Volume 8, Number 2, Spring 2022

Advanced Ceramics Progress

ISSN 2423-7477
e-ISSN 2423-7485

Advanced Ceramics Progress

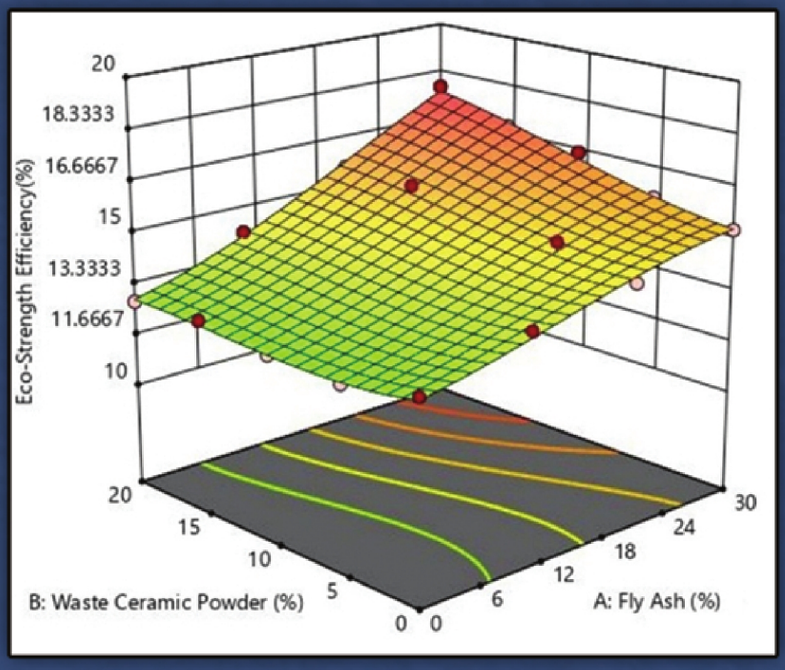

Materials and Energy Research Center

Iranian Ceramic Society

In The name of God

Advanced Ceramics Progress

DISCLAIMER

The publication of articles in Advanced Ceramics Progress does not imply that the editorial board, editorial advisory board, reviewers or the publisher accept, approve or endorse the data and conclusions of authors.

Advanced **Cer**amics **P**rogress (ISSN 2423-7477) (e-ISSN 2423-7485)
Web Site: www.acerp.ir, E-mail: office@acerp.ir
Tel: +98 (0) 26 36280040-7 ext.: 382, Fax: +98 (0) 26 36201888
Tel:+98 (0)21 88771626-7 ext.: 8931, Fax: +98 (0)21 88773352
Materials and Energy Research Center (MERC); Iranian Ceramic Society (ICERS)

ISSN: 2423-7477; e-ISSN: 2423-7485

Advanced Ceramics Progress: Vol. 8, No. 2, (Spring 2022) 1-72

CONTENTS

Advanced Ceramics Progress: Vol. 8, No. 2, (Spring 2022) 1-11

Materials and Energy Research Center
MERC

Contents lists available at ACERP

Advanced Ceramics Progress

Journal Homepage: www.acerp.ir

Original Research Article

Oxidation Behavior of HfB_2-SiC-Nd_2O_3 Ultra-High Temperature Composite Sintered through SPS Process

Younes Hanifeh [a], Maryam Shojaie-Bahaabad [b,*], Mohammad Jafar Molaei [b]

[a] *MSc Student, Faculty of Chemical and Materials Engineering, Shahrood University of Technology, Shahrood, Semnan, Iran*
[b] *Assistant Professor, Faculty of Chemical and Materials Engineering, Shahrood University of Technology, Shahrood, Semnan, Iran*

* Corresponding Author Email: mshojaieb@shahroodut.ac.ir (M. Shojaie-Bahaabad)

URL: https://www.acerp.ir/article_149762.html

ARTICLE INFO

Article History:

Received 6 April 2022
Received in revised form 8 May 2022
Accepted 14 May 2022

Keywords:

HfB_2-SiC-Nd_2O_3 Composite
Oxidation Behavior
Spark Plasma Sintering
Rare Earth Element

ABSTRACT

The current study aims to fabricate HfB_2-30 vol. % SiC and HfB_2-30 vol. % SiC-2 vol. % Nd_2O_3 composites through Spark Plasma Sintering (SPS) method at 1950 °C for 10 min. The oxidation behavior of the prepared composites was investigated at 1400 °C and different times namely 4, 8, 12, and 16 hours. The relative density, hardness, toughness, and strength of the HfB_2-30 vol. % SiC composite increased from 98.5 %, 20.19 GPa, 414.9 MPa, and 4.36 MPa.$m^{0.5}$ up to 99.1 % , 24.47 GPa, 485 .5 MPa, and 4.93MPa.$m^{0.5}$ for HfB_2-30 vol. % SiC-2 vol. % Nd_2O_3 composite, respectively. After 16 hours of oxidation, SiO_2 layer, which was extremely thick, was produced locally on the oxidized HfB_2-30 vol. % SiC composite surface. The thinckness of the SiO_2 layer was calculated to be around 25 µm. The thickness measurement revealed the SiO_2 produced layer on the surface of the HfB_2-30 vol. % SiC-2 vol. % Nd_2O_3 composite to be 5 µm. The oxidation kinetic results of the composite exhibited linear-parabolic behavior. The chemical reaction during the oxidation process controlled the oxidation rate after eight hours. After 16 hours of performing the oxidation procedure at 1400 °C, HfB_2-30 vol. % SiC-2 vol. % Nd_2O_3 composite exhibited parabolic behavior, while HfB_2-30 SiC exhibited linear behavior. This composite's improved oxidation resistance was attributed to $Nd(Hf,Si)O_xC_y$ phases and decreased porosity, resulting in the generation of thin, dense, adherent, and protective layers. Therefore, it was concluded that the oxygen diffusion rate could control the oxidation process in HfB_2-30 vol. % SiC-2 vol. % Nd_2O_3 composite.

https://doi.org/10.30501/acp.2022.336283.1086

1. INTRODUCTION

Ceramic materials characterized by high melting temperatures (> 3000 °C) are referred to as Ultra-High Temperature Ceramics (UHTCs) that are promising materials for Thermal Protection Systems (TPSs). Transition metal nitrides, carbides, and diborides are known as the members of the UHTCs family [1-3]. These compounds have such characteristics as high melting point, good thermal and electrical conductivity, excellent stability against metal melt, considerable heat shock resistance, high Young's modulus, and relatively good hardness and resistance against chemical attacks [4]. Of note, higher melting point (e.g., 3380 °C) and better electrical and thermal conductivity of HfB_2 than those of other intermetallic compounds such as carbides, nitrides, and deborides have encouraged researchers to shift their focus to conducting extensive research on HfB_2-based ceramics [5,6].

HfB_2 ceramics are commonly fabricated through

Please cite this article as: Hanifeh, Y., Shojaie-Bahaabad, M., Molaei, M. J., "Oxidation Behavior of HfB_2-SiC-Nd_2O_3 Ultra-High Temperature Composite Sintered through SPS Process", ***Advanced Ceramics Progress***, Vol. 8, No. 2, (2022), 1-11. https://doi.org/10.30501/acp.2022.336283.1086

pressureless sintering (> 2150 °C), hot pressing (1800-2000 °C), and Spark Plasma Sintering (SPS) methods. Without using sintering aids, HfB_2 ceramics are densified at temperatures above 2000 °C in the range of 20-30 MPa and at a temperature of about 1700-1800 °C in the range of 800-1500 MPa as well through hot pressing [7-10]. SPS is a favorable process used to compact HfB_2 ceramics at lower temperatures in a short time period that needs less sintering aid than the conventional methods.

In recent years, several researchers have employed the SPS method for HfB_2 ceramics compaction. This method applies direct pulse current and external axial force in a simultaneous manner on compacted powder in a graphite die in order to accelerate sintering. Its high heating rate and low sintering temperature, compared to other methods, yield a finer microstructure. Owing to the spark created among the powder particles and use of direct pulse flow, this method can successfully compact materials with poor sinterability [11-14]. Moreover, additives such as metals, nitrides, carbides, and desilicides are usually used for improving the sintering consolidation of HfB_2 ceramics [15-19].

One of the main drawbacks of HfB_2 ceramics is, however, their poor oxidation resistance. HfB_2 oxidation begins at the low temperature of about 1000 °C, depending on the oxygen partial pressure. The molten B_2O_3 fills the pores, thus forming a protective layer to prevent further oxidation of matrix up to the temperature of 1100 °C. At a temperature of about 1400 °C, upon increasing the oxygen partial pressure, B_2O_3 and HfB_2 are rapidly evaporated and oxidized, respectively, hence formation of some porous and cracked layers on the surface [20].

A promising approach to improving the oxidation resistance of HfB_2 ceramics is the addition of SiC to HfB_2, typically in the volume range of 10-30 vol. %. Followed by oxidization of HfB_2-SiC composite, a borosilicate glassy layer is developed on the composite surface. The borosilicate layer melts at a lower temperature, yet it can withstand temperatures up to 2000 °C for about 1 h in a non-air flowing atmosphere [20]. The borosilicate layer vanishes at termperatures above 2000 °C and the bulk composite is likely to experience active oxidation.

A variety of methods have been proposed to date to improve the oxidation resistance of UHTC HfB_2-SiC ceramics, some of which are listed in the following: adding different compounds such as Si and making a solid solution using HfB_2 [14,21-23], increasing the viscosity and melting point of the borosilicate layer by adding metal elements [24], adding metal boride compounds [25-27], using rare earth compounds, and forming refractory phases with a high melting temperature in the protective layer [28,29], to name a few. There are, however, few studies that already investigated the long-term oxidation of HfB_2-SiC coating at a temperature of 1500 °C for 50 [30] and 753 h [31]. Studies on the oxidation are commonly conducted at tempratures of 1500-1700 °C up to 10 h [21,24]. Zapata-Solvas et al. reported the oxidation kinetics for the HfB_2-SiC-La_2O_3 composite in the temprature range of 1400-1600 °C for up to 32 h [32]. In the particular case of adding Nd_2O_3, $Nd_2Hf_2O_7$ pyrochlore compound has a low vapor pressure at high temperatures (> 2000 °C) [33]. In addition to the phase stability in such a wide temperature range, the melting point of neodymium hafinate is high (2330-2700 °C), as reported in many studies [34]. As a result, it makes this crystal phase a good candidate for UHTCs which needs to withstand the temperatures of about 2000 °C.

However, almost no study has been conducted on the oxidation behavior of HfB_2-SiC-Nd_2O_3 composites. In this regard, the current study aimed to fabricate HfB_2-30 vol. % SiC-2 vol. % Nd_2O_3 composite through the SPS method. In fact, this research makes a comparison between the prepared composite and HfB_2-30 vol. % SiC composite in terms of their oxidation resistance. The oxidation behavior of the obtained composites was also examined at a temperature of 1400 °C and different times of 4, 8, 12, and 16 h.

2. MATERIALS AND METHODS

Commercial HfB_2 (Beijing Cerametek Materials Co., China, particle size of < 2 µm and purity of > 99 %), SiC (Xuzhou Co., China, particle size of < 10 µm and purity of 99 %), and Nd_2O_3 (Xuzhou Co., China, particle size of < 5 µm and purity of 99.8 %) powders were used and mixed to make HfB_2-30 vol. % SiC-Nd_2O_3 composites. The theoretical densification values for SiC, HfB_2, and Nd_2O_3 were obtained as 3.2 g/cm^3 for, 11.2 g/cm^3, and 7.24 g/cm^3, respectively, and the volume fractions of the raw materials were calculated based on these values to achieve the final compositions. The powder mixtures were minced through high-energy planetary milling using balls and a WC-Co cup at 300 rpm for three hours in ethanol medium at the weight ball to powder ratio of 10:1. The slurry was then dried out at a temperature of 60 °C for two hours. HfB_2-30 vol. % SiC composites containing 0 and 2 vol. % Nd_2O_3 (named Nd0 and Nd2) were prepared through the SPS method at 1950 °C in 10 min with the vacuum of 0.05 mbar under the pressure of 40 MPa. The relative densification in the distilled water was then calculated using Archimedes technique; theoretical densification was measured based on the mixtures' law. Phase analysis of the composites was performed by the X-ray diffraction pattern (XRD, Philips, Model: X'Pert MPD, Co Kα1, λ: 1.78897 Å); their surface and microstructure were studied using Field Emission Scanning Electron Microscope (FESEM, TESCAN, Model: MIRA) prepared by Energy Dispersive Spectroscopy (EDS). The hardness of the composites was then measured by utilizing the Vickers hardness tester under 1 kg, with the loading time being 10 s. The toughness of composites was obtained using

Equation 1 [28]:

$$K_{IC} = 0.073 (P/c^{1.5}) \quad (1)$$

where K_{IC} represents the fracture toughness (MPa.$m^{1/2}$), P the applied load (N), and c the average half-length of the crack (µm). The flexural strength of composite was evaluated using a three-point flexural machine (Zwick Roell SP600, Germany) having a loading rate of 0.05 mm/min. Oxidation behavior was investigated in an electric furnace at a temperature of 1400 °C for 4, 8, 12, and 16 h. The oxidation resistance of composites was then evaluated based on the weight changes and the oxide layer thickness following oxidation.

3. RESULTS AND DISCUSSION

The densification of the prepared composites exhibited that by adding Nd_2O_3 up to 2 vol. %, composite densification was enhanced from 98.5 % to 99.1 %. Nd_2O_3 seemed to react with oxide impurity on the surface of HfB_2 and SiC particles, forming a liquid phase, as a result of which powders sinterability and densification were increased [29,33].

The XRD patterns of the composites following the SPS process are shown in Figure 1. Based on the XRD patterns of the composites, HfB_2 and SiC phases could be seen in the samples, too. The trace of $Nd_2Hf_2O_7$ phase was identified in the Nd2 composite. Thus, HfO_2 impurities on the surface of HfB_2 particles reacted, leading to the formation of Nd_2O_3 and $Nd_2Hf_2O_7$ phase [35].

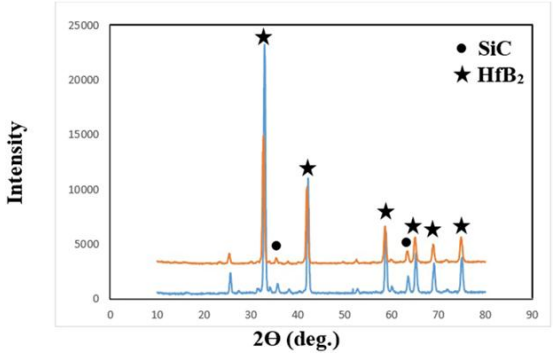

Figure 1. XRD patterns of the sintered composites

Figure 2 shows the SEM image and EDS analysis of the composite surface following the SPS process. Based on the EDS analysis, the dark and light gray areas were SiC and HfB_2 phases, respectively. At the junction of several HfB_2 grains, dark gray areas could be observed. According to the XRD patterns and EDS analysis (Figure 1 (C)), these areas were $Nd_2Hf_2O_7$.

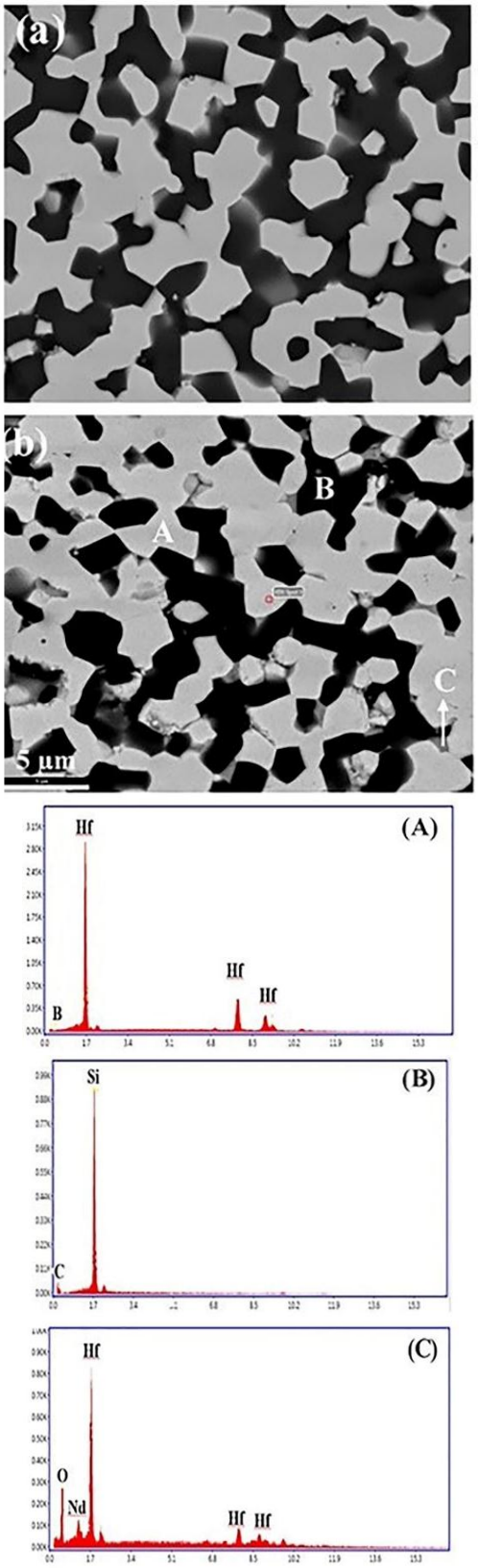

Figure 2. FESEM images and EDS analysis of the sintered composites: (a) HfB_2-SiC and (b) HfB_2-SiC-2 vol. % Nd_2O_3

Figure 3 shows the sintered composites' fracture surface. An oxide layer on the surfaces of non-oxide particles (e.g., SiO_2 B_2O_3, and HfO_2) led to the generation of borosilicate glassy phases. Jaberi et al. investigated the ZrB_2-SiC composite prepared by the hot pressing method and found that the glassy phase in the SEM images appread in the form of a cleavage or planar state, thin thickness, or inelastic and elastic fracture surface [36]. Such a glassy phase was well visible in the SEM images obtained from the cross-section of the composites that had been prepared in the present research (dashed flash). The HfB_2-SiC composites had an intergranular-transgranular fracture. Particles pullout and sharp edges could be seen in the photos, thus implying that the intergranular fracture had happened across the grain boundary (thick arrows). Elastic and broad surfaces reflecting transgranular fractures could be detected in some regions (narrow arrows), particularly when confronted with atypical grain growth, in comparison to others.

The investigation of the mechanical properties of thHfB_2-30 SiC composite demonstrated that the hardness, flexural strength, and toughness of the Nd0 specimen were 20.19 GPa, 414.9 MPa, and 4.36 MPa.$m^{0.5}$. When the addition of Nd_2O_3 to the HfB_2-30 SiC composite was done, the hardness, flexural strength, and toughness of the composites increased to 24.47 GPa, 485 .5 MPa, and 4.93MPa.$m^{0.5}$, respectively, because of the rise of the densification of the composite. Researchers have also investigated the impact of Re_2O_3 addition on the mechanical properties of ZrB_2-based composites [37]. They reported the improved densification of ZrB_2-SiC composites which were doped with Re_2O_3 due to the ability of Re_2O_3 to form liquid phases with SiO_2, B_2O_3, and ZrO_2 impurities, thus strengthening the grain boundaries. So, stronger grain boundaries and denser matrix with lower residual porosity could enhance mechanical properties. In the present research study, similar results were obtained in regard to HfB_2-SiC-Nd_2O_3 composite.

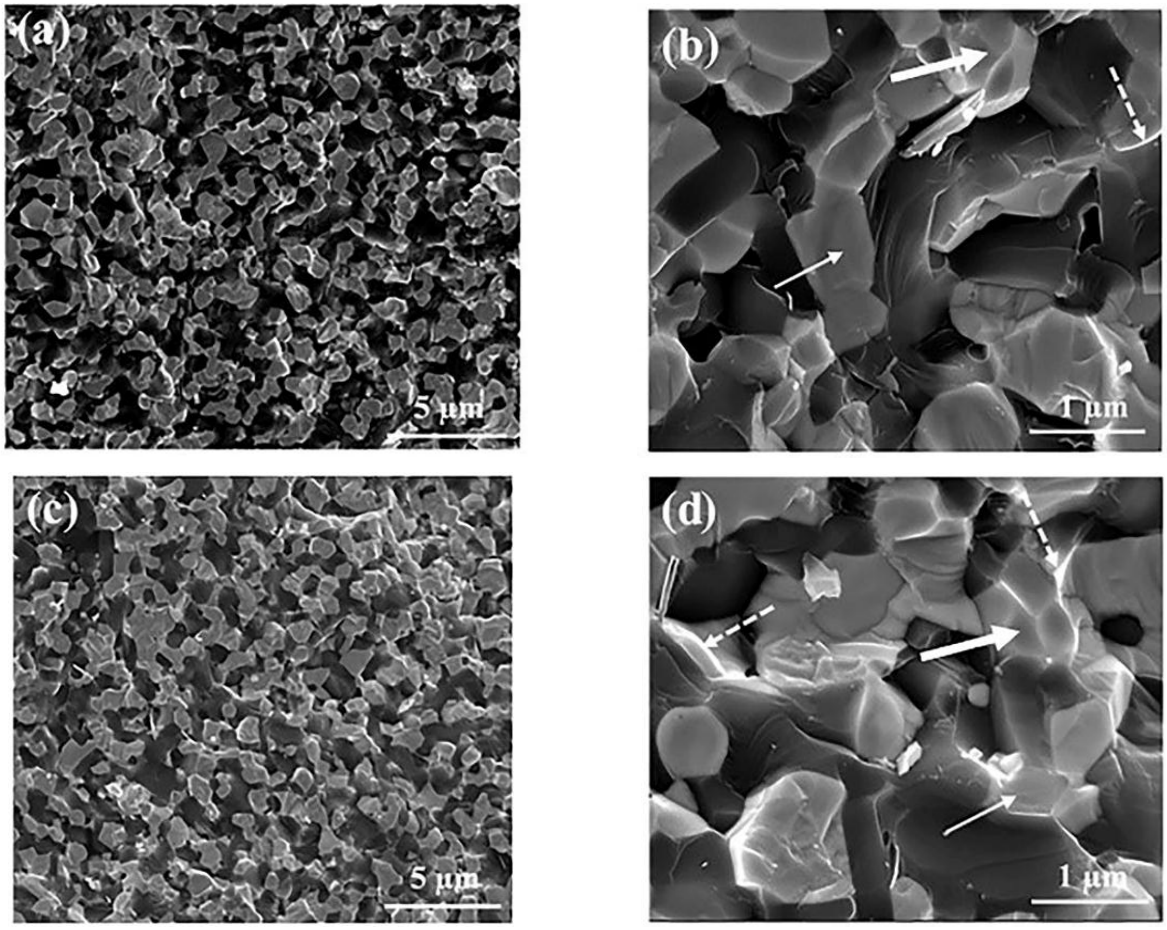

Figure 3. FESEM images of the fracture surface of the sintered composites: (a,b) HfB_2-SiC and (c,d) HfB_2-SiC-2 vol. % Nd_2O_3

The effects of the Vickers hardness indenter on HfB_2-30 SiC composites are depicted in Figure 4. As shown in the Nd2 sample, the hardness test had a regular effect and no deformation was observed around it. This could be due to the high densification of this sample, as compared to the Nd0 sample. In the Nd0 sample, the hardness effect

was more irregular due to the higher porosity of this composite.

XRD patterns of HfB_2-SiC composites, following oxidation at a temperature of 1400 °C for 16 h, are shown in Figure 5. In HfB_2-SiC composites, $HfSiO_4$ and HfO_2 phases could be seen as the main phases and some SiO_2 phase was identified in the XRD patterns following oxidation.

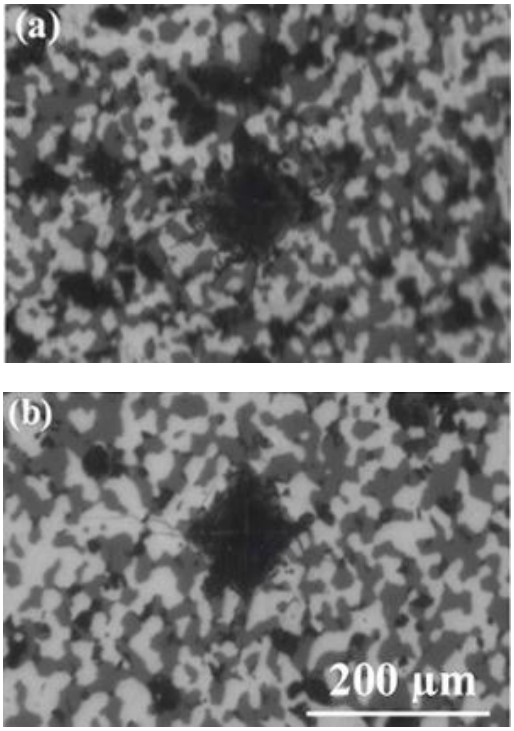

Figure 4. FESEM images of Vickers indenter effect of the sintered composites: (a) HfB_2-SiC and (b) HfB_2-SiC-2 vol. % Nd_2O_3

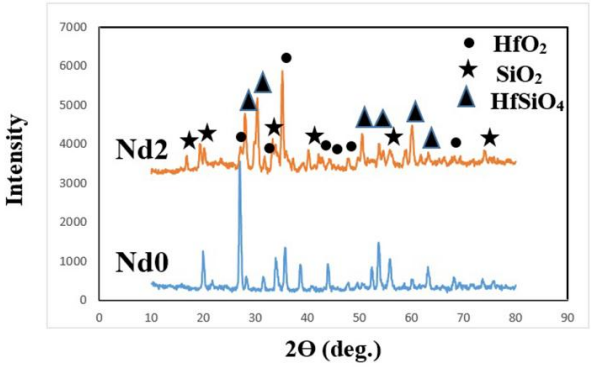

Figure 5. XRD patterns of the sintered composites after the oxidation test at 1400 °C for 16 h

The HfB_2-30 SiC composite surface following oxidization at a temperature of 1400 °C for different times is shown in Figure 6. The composite's surface was locally coated with a glass layer and evenly distributed on the composite surface following oxidation for a period of 16 h.

Oxidation of SiC particles at temperatures above 1100 °C led to the generation of some SiO_2 glass layer on the composite surface [38]. EDS analysis also showed that the glass layer was evenly composed of Si and O. Further, the white crystals with different sizes and shapes were observed on the composites surafce following oxidation. According to the EDS analysis, spherical crystals with Hf and O high content were HfO_2 crystals. The surface of the Nd2 composite was smoothly coated by this oxide layer; it consisted of a needle-like crystal phase following oxidation for more than 12 h.

According to the EDS analysis (Figure 7), these crystals with equal Hf and Si content were $HfSiO_4$ crystals. The formation of crystalline phases in the present study is described in the following. Following the formation of SiO_2 and HfO_2 and molten B_2O_3 (according to reactions (2) and (3)) [36], there was the dissolution of HfO_2 in borosilicate melt first, leading to the formation of SiO_2-B_2O_3 (HSB) liquid in the glass layer.

$$2\ SiC\ (s) + 3\ O_2\ (g) = 2\ SiO_2\ (l) + 2\ CO\ (g) \quad (2)$$

$$2\ HfB_2\ (s) + 5\ O_2\ (g) = 2\ HfO_2\ (s) + 2\ B_2O_3\ (l) \quad (3)$$

Then, with the development of the oxidation process, the HSB liquid flowed on the top of the glass layer. Upon evaporation of B_2O_3, precipitation of HfO_2 particles from the HSB liquid occurred. Further, HfO_2 could react with SiO_2 (reaction (4)) and $HfSiO_4$ particles could also be formed [35].

$$SiO_2\ (l) + HfO_2\ (s) = HfSiO_4\ (s) \quad (4)$$

The molten B_2O_3 evaporates at temperatures above 1100 °C; its evaporation rate is faster than the formation rate of the molten B_2O_3 in the temperature range of 1100-1400 °C, according to Reaction (5) [39]. Thus, B_2O_3 phase was not observed in the X-ray pattern of composites following oxidation.

$$B_2O_3\ (l) = B_2O_3\ (g) \quad (5)$$

As can be seen in the XRD patterns, the trace $HfSiO_4$ phase was also formed in the Nd0 sample. As mentioned before, SiO_2 was locally distributed on the surface of Nd0 composite. As a result, $HfSiO_4$ particles were formed in lower amounts, as compared locally to the Nd2 composite. Based on the formation of $HfSiO_4$ silicate phase and the locking effect of this phase in the glassy layer, the oxide layer which was formed on the surafce of the Nd2 sample protected the HfB_2-30 SiC composite in a more effective manner than the Nd0 composite.

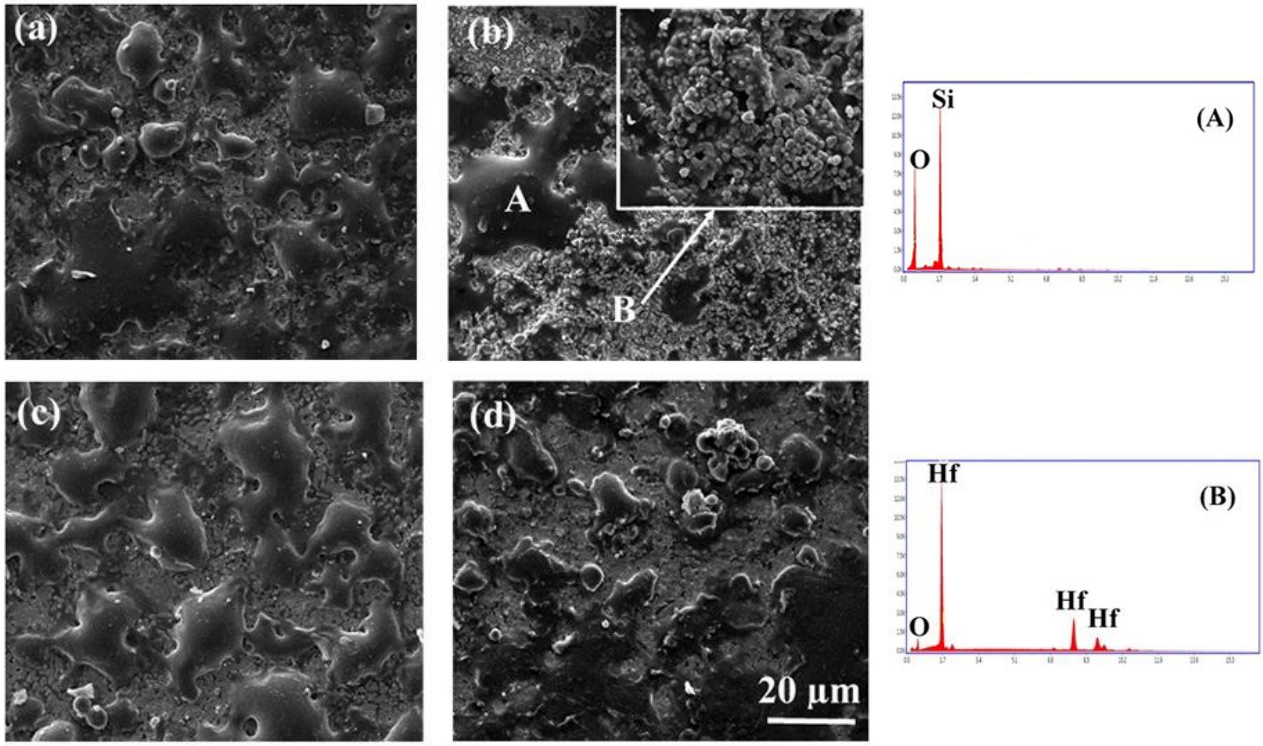

Figure 6. FESEM image and EDS analysis of the surface of HfB_2-SiC composite after the oxidation test at 1400 °C at different times: (a) 4, (b) 8, (c) 12, and (d) 16 h

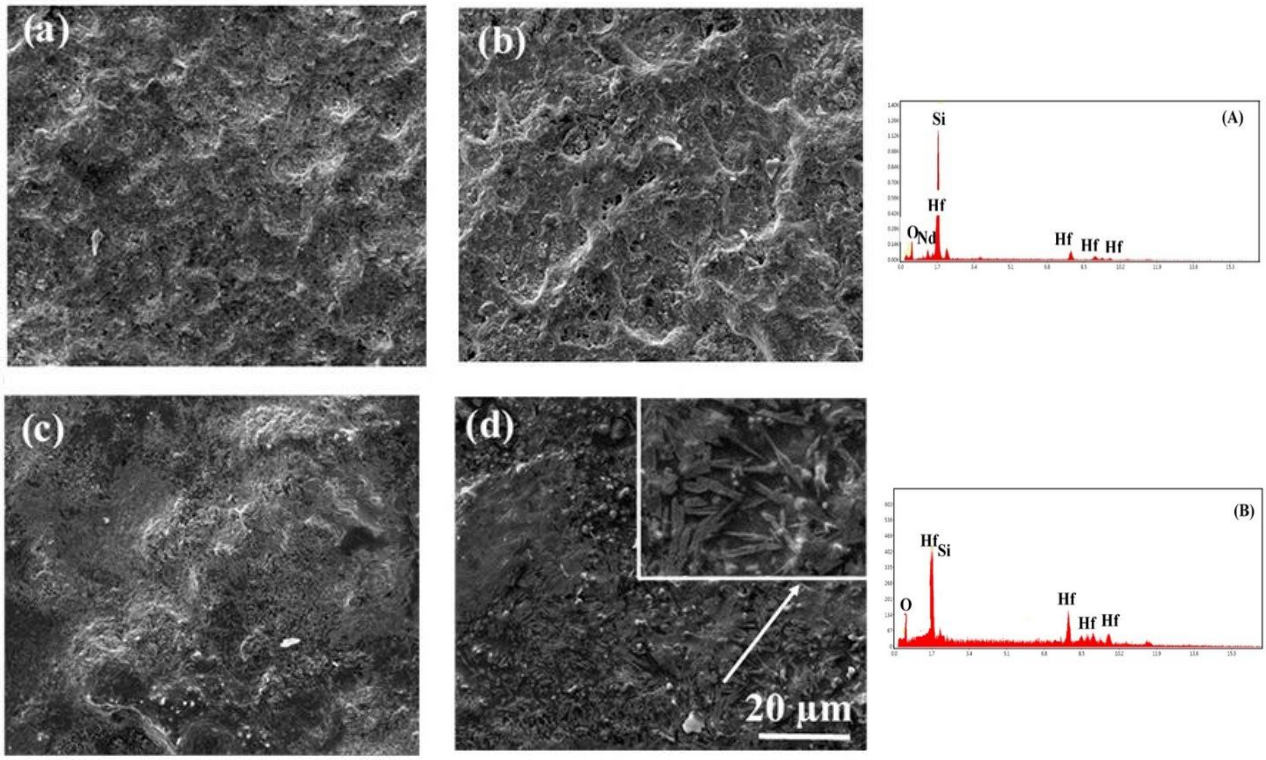

Figure 7. FESEM image and EDS analysis of the surface of HfB_2-SiC-2 vol. % Nd_2O_3 composite after the oxidation test at 1400 °C for different times, (a) 4, (b) 8, (c) 12, and (d) 16 h

Figures 8 and 9 represent the composites' sample cross-section following the oxidation test for different times. According to the EDS analysis, the first layer was rich in Si and the second one had moderate values of Si and Hf.

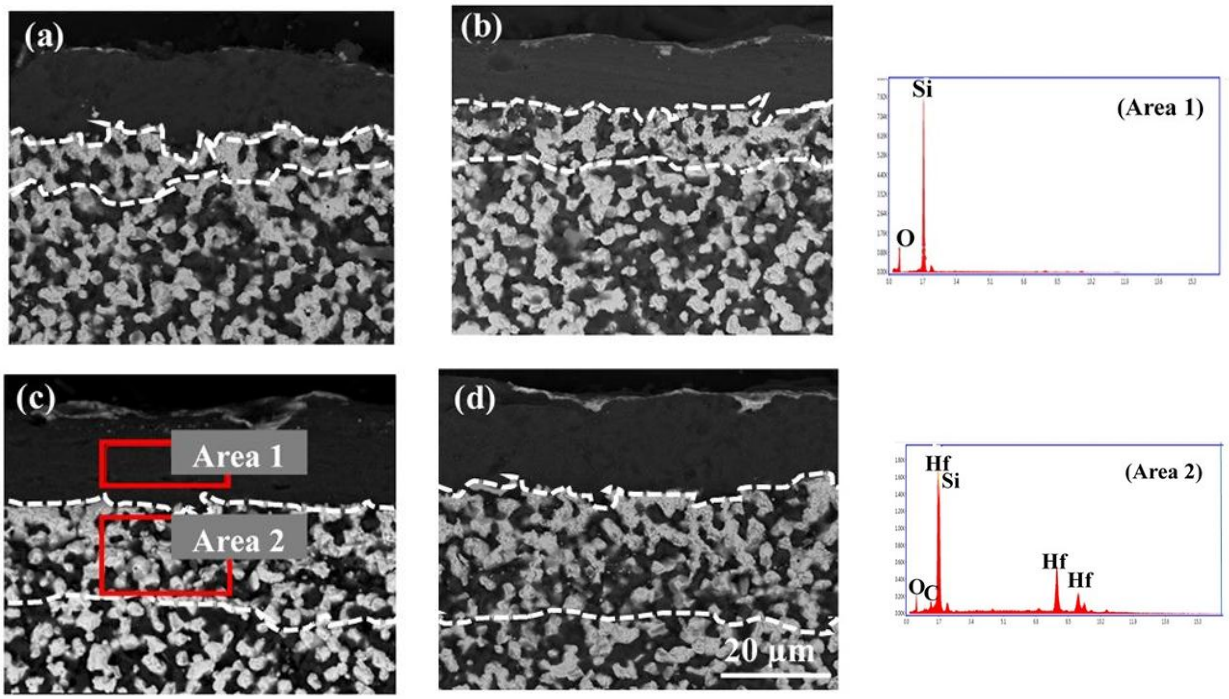

Figure 8. FESEM image and EDS analysis of cross-section of HfB_2-SiC composite after the oxidation test at 1400 °C for different times, (a) 4, (b) 8, (c) 12, and (d) 16 h

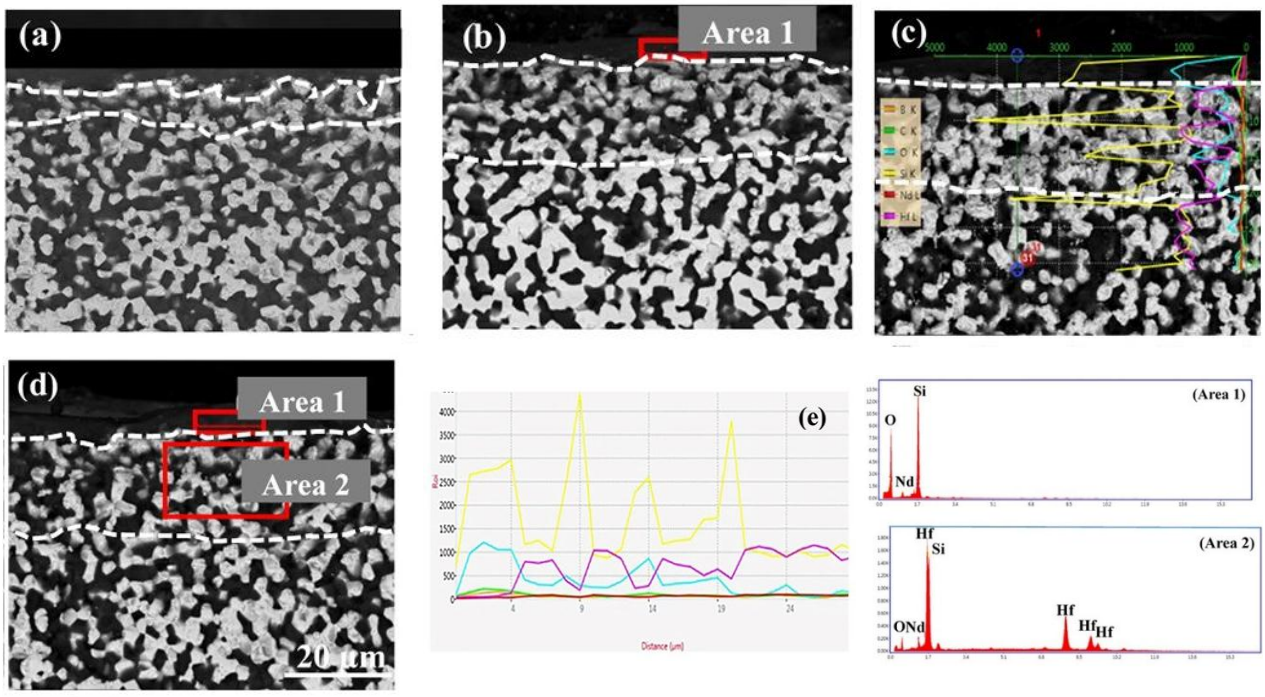

Figure 9. FESEM image and EDS analysis of cross-section of HfB_2-SiC-2 vol. % Nd_2O_3 composite after the oxidation test at 1400 °C for different times, (a) 4, (b) 8, (c) 12, and (d) 16 h

The thickness of the SiO_2 rich layer which was produced on HfB_2-30 SiC composites' surface following the oxidation test can be seen in Figure 8. As can be observed, the overall oxide layer thickness was increased greatly with increasing the duration time for the HfB_2-30 SiC composite. The SiO_2 oxide layer was not smoothly formed on the surface during oxidation. Over time, a partial glass layer and greater porosity might enhance oxygen penetration into the bulk. Because of the growth of the oxide scale layer throughout the oxidation process, this layer no longer protected the bulk from oxidation. These results were, thus, consistent with those obtained by other researchers [40-42].

According to Figure 10, the oxides layer's thickness was minimal and gradually grew for the Nd2 composite, as compared to the HfB_2-30 SiC composite. Furthermore, the oxide layer thickness in the HfB_2-based composites was less than the stated values in the previous research [43]. As a result of the rare earth oxide presence, the viscosity of the borosilicate glass layer was increased; due to the rise of the capillary forces, the borosilicate layer did not move directly to the upper surface, thus resulting in a more uniform mixture between the glass and oxide phases and improving the oxidation resistance of the UHTCs composite [32]. Therefore, by adding Nd_2O_3, the oxidation resistance of the HfB_2-30 SiC composite was improved, leading to the formation of a thinner oxide layer in this study.

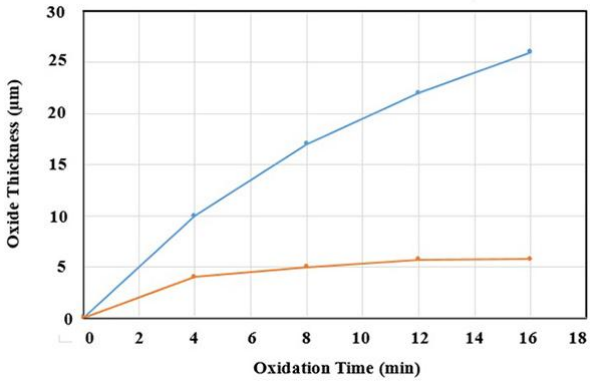

Figure 10. Variation of oxide layer thickness as a function of oxidation time for (a) HfB_2-SiC and (b) HfB_2-SiC-2 vol. % Nd_2O_3 composite

Figure 11 represents the weight gain with oxidation time for HfB_2-30 SiC and Nd2 composites following a 16 h oxidation test at a temperature of 1400 °C. The findings demonstrate that the Nd2 composite had substantially better oxidation resistance at this temperature due to the lower weight growth. The change of weight gain per unit surface area (W/S) as a function of oxidation time could determine the oxidation mechanism. The kinetic variables, n and k, could be obtained using Equation 6 [41]:

$$(\Delta W/S)^n = kt + B \quad (6)$$

where k is the constant of parabolic oxidation rate ($g^2cm^{-4}s^{-1}$), ΔW indicates the weight gain (g), S reflects the surface area (cm^2), t stands for the duration of isothermal oxidation (s), n represents the index of oxidation law ($0.35 \leq n \leq 0.55$ for parabolic behavior), and B is a constant.

A linear trend indicates response rate-controlled kinetics, while a parabolic one reflects diffusion rate-controlled ones. In the current research study, Nd2 exhibited a parabolic behavior (n = 0.51), while HfB_2-30 SiC had a linear one (n = 0.85) following the oxidation process for a period of 16 h at a temperature of 1400 °C. The HfB_2-30 SiC composite had low densification; therefore, the SiO_2 layer was generated locally on the composite surface. Thus, more oxygen penetrated the bulk owing to the active SiC oxidation at a high temperature of 1400 °C and more SiO (g) was formed, as compared to SiO_2 (l) (reaction (7)) [36], thus suggesting the oxidation control under this condition by the reaction rate.

$$SiC\ (s) + O_2\ (g) = SiO\ (g) + CO\ (g) \quad (7)$$

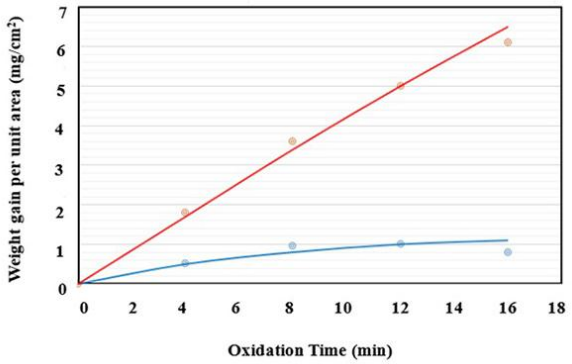

Figure 11. Weight gain as a function of oxidation time for (a) HfB_2-SiC and (b) HfB_2-SiC-2 vol. % Nd_2O_3 composite

The improved oxidation resistance of Nd2 composite could be associated to the generation of thin, dense, adherent, and protective layers formed as a result of the formed Si-based phase, thus leading to parabolic oxidation kinetics. These oxide layers can serve as barriers to the oxygen transport. Further, in the Nd2 composite, due to the generated oxycarbide compounds in the oxide layer and the decrease of oxygen diffusion, oxidation was controlled by the diffusion rate. However, following the formation of Nd-HfO_xC_y and Nd-SiO_xC_y phases, oxygen was applied at these phases of oxidation. Thus, the oxygen diffiusion rate in the bulk was reduced, hence improving the oxidation resistance of the composite and gradually increasing the oxidation rate in the incorporated HfB_2-30 SiC matrix. It is important to

note that the narrow, dense and compact layers comprising the Si-glass phase acted as a protective layer for the composite throughout the oxidation process, thus improving its oxidation resistance at high temperatures.

The Nd2 composite cross-section with high magnification can be seen in Figure 12.

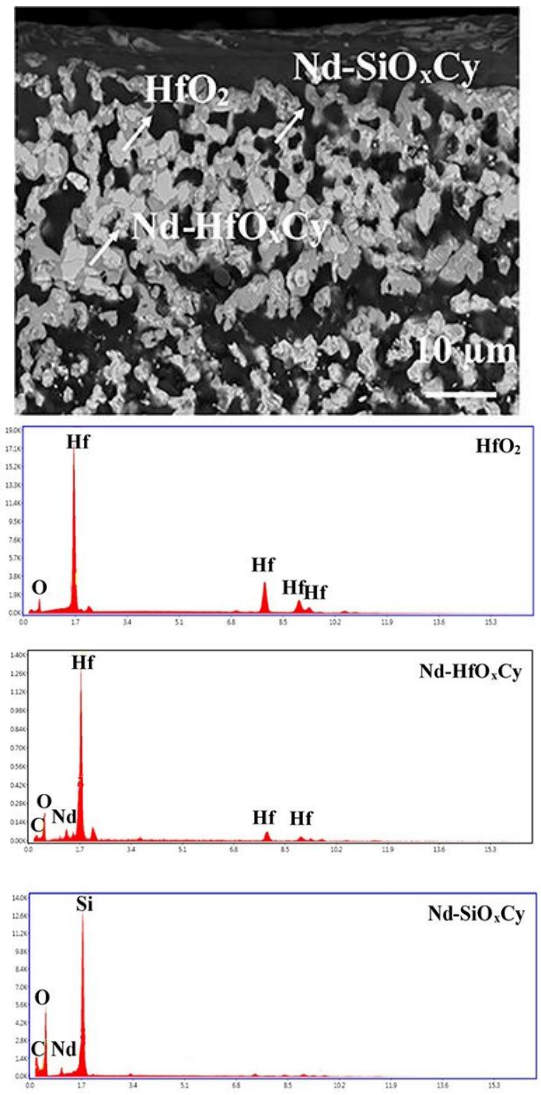

Figure 12. Cross-section of the HfB_2-SiC-2 vol. % Nd_2O_3 composite sample after the oxidation test for 16 h

Zapata et al. [32] found that with the addition of La_2O_3 to MeB_2 (Me = Hf, Zr)-SiC composites MeO_xC_y, La-MeO_xC_y and SiO_xC_y compounds formed following oxidation at 1500 °C for a period of 3 h, respectively. These researchers introduced the formed phases as new protective coatings for ultra-high temperature ceramics, as the oxygen diffusion coefficients were decreased and the oxidation resistance of the composites was raised to resist oxidation conditions for a long time. Thus, in this research study, the addition of Nd_2O_3 to HfB_2-SiC composites probably led to the formation of HfO_2, Nd-HfO_xC_y, and Nd-SiO_xC_y oxycarbide compounds in the oxide layer; thus, these compounds continuously reacted with oxygen and oxidized, reducing the penetration of oxygen-containing species into the composite. Therefore, the composite would follow a stabilized trend at long exposure times.

4. CONCLUSION

HfB_2-30 vol. % SiC and HfB_2-30 vol. % SiC-2 vol. % Nd_2O_3 composite samples were oxidized for 16 hours in a typical oxidation furnace to compare the oxidation behavior at a temperature of 1400 °C. Two layers were generated in each composite. The Si-based glass phase was in all layers. Based on microstructural examinations, no Si-depleted layer was discovered. After the oxidation procedure, a SiO_2 layer was generated on the surface of the oxidized HfB_2-30 vol. % SiC composite locally. This layer was extremely dense. The thickness of SiO_2 layer was calculated to be around 25 µm. Because of its increased porosity, the HfB_2-30 vol. % SiC composite indicated poor oxidation resistance, based on the findings. The thickness measurements revealed that the SiO_2 generated layer on the surface of Nd2 was 5 µm thick. After a 16-hour oxidation procedure at 1400 °C, Nd2 exhibited a parabolic behavior, while HfB_2-30 SiC exhibited a linear one. The improved oxidation resistance of this composite could be attributed to the formed Si-based phase and the decreased porosity, generating narrow, dense, adherent, and protective layers.

ACKNOWLEDGEMENTS

The authors wish to acknowledge Sharood University of Technology for the all support throughout this work.

REFERENCES

1. Chen, X., Feng, Q., Zhou, H., “Ablation behavior of three-dimensional C_f/SiC-ZrC-ZrB_2 composites prepared by a joint process of sol-gel and reactive melt infiltration”, ***Corrosion Science***, Vol. 134, (2018), 49-56. https://doi.org/10.1016/j.corsci.2018.02.011
2. Liu, T., Niu, Y., Li, C., Zhao, J., Zhang, J., Zeng, Y., Zheng, X., Ding, C., “Effect of $MoSi_2$ addition on ablation behavior of ZrC coating fabricated by vacuum plasma spray”, ***Ceramics International***, Vol. 44, No. 8, (2018), 8946-8954. https://doi.org/10.1016/j.ceramint.2018.02.093
3. Shojaie-Bahaabad, M., Hasani-Arefi, A., “Ablation properties of ZrC-SiC-HfB_2 ceramic with different amount of carbon fiber under an oxyacetylene flame”, Materials Research Express, Vol. 7, No. 2, (2020), 025604. https://doi.org/10.1088/2053-1591/ab70db
4. Binner, J., Porter, M., Baker, B., Zou, J., Venkatachalam, V., Diaz, V. R., D'Angio, A., Ramanujam, P., Zhang, T., Murthy, T. S. R. C., “Selection, processing, properties and

applications of ultra-high temperature ceramic matrix composites, UHTCMCs–a review", ***International Materials Reviews***, Vol. 65, No. 7, (2020), 389-444. https://doi.org/10.1080/09506608.2019.1652006

5. Ghelich, R., Jahannama, M. R., Abdizadeh, H., Torknik, F. S., Vaezi, M. R., "Hafnium diboride nonwoven mats with porosity/morphology tuned via different heat treatments", ***Materials Chemistry and Physics***, Vol. 248, (2020), 122876. https://doi.org/10.1016/j.matchemphys.2020.122876
6. Wang, H., Lee, S. H., Kim, H. D., Oh, H. C., "Synthesis of ultrafine hafnium diboride powders using solution-based processing and spark plasma sintering", ***International Journal of Applied Ceramic Technology***, Vol. 11, No. 2, (2014), 359-363. https://doi.org/10.1111/ijac.12016
7. Zou, J., Zhang, G. J., Kan, Y. M., Ohji, T., "Pressureless sintering mechanisms and mechanical properties of hafnium diboride ceramics with pre-sintering heat treatment", ***Scripta Materialia***, Vol. 62, No. 3, (2010), 159-162. https://doi.org/10.1016/j.scriptamat.2009.10.014
8. Monteverde, F., "Hot pressing of hafnium diboride aided by different sinter additives", ***Journal of Materials Science***, Vol. 43, No. 3, (2008), 1002-1007. https://doi.org/10.1007/s10853-007-2247-9
9. Ni, D. W., Liu, J. X., Zhang, G. J., "Pressureless sintering of HfB_2-SiC ceramics doped with WC", ***Journal of the European Ceramic Society***, Vol. 32, No. 13, (2012), 3627-3635. https://doi.org/10.1016/j.jeurceramsoc.2012.05.001
10. Gasch, M., Johnson, S., "Physical characterization and arc jet oxidation of hafnium based ultra-high temperature ceramics fabricated by hot pressing and field-assisted sintering", ***Journal of the European Ceramic Society***, Vol. 30, No. 11, (2010), 2337-2344. https://doi.org/10.1016/j.jeurceramsoc.2010.04.019
11. Ghadami, S., Taheri-Nassaj, E., Baharvandi, H. R., "Novel HfB_2-SiC-$MoSi_2$ composites by reactive spark plasma sintering", ***Journal of Alloys and Compounds***, Vol. 809, (2019), 151705. https://doi.org/10.1016/j.jallcom.2019.151705
12. Wang, H., Lee, S. H., Feng, L., "HfB_2-SiC composite prepared by reactive spark plasma sintering", ***Ceramics International***, Vol. 40, No. 7, (2014), 11009-11013. https://doi.org/10.1016/j.ceramint.2014.03.107
13. Ghadami, S., Taheri-Nassaj, E., Baharvandi, H. R., Ghadami, F., "Improvement of mechanical properties of HfB_2-based composites by incorporating in situ SiC reinforcement through pressureless sintering", ***Scientific Reports***, Vol. 11, No. 1, (2021), 1-11. https://doi.org/10.1038/s41598-021-88566-0
14. Zapata-Solvas, E., Jayaseelan, D. D., Lin, H. T., Brown, P., Lee, W. E., "Mechanical properties of ZrB_2-and HfB_2-based ultra-high temperature ceramics fabricated by spark plasma sintering", ***Journal of European Ceramic Society***, Vol. 33, No. 7, (2013), 1373-1386. https://doi.org/10.1016/j.jeurceramsoc.2012.12.009
15. Shahriari, M., Zakeri, M., Razavi, M., Rahimipour, M. R., "Investigation on microstructure and mechanical properties of HfB_2-SiC-HfC ternary system with different HfC content prepared by spark plasma sintering", ***International Journal of Refractory Metals and Hard Materials***, Vol. 93, (2020), 105350. https://doi.org/10.1016/j.ijrmhm.2020.105350
16. Mashayekh, S., Baharvandi, H. R., "Effects of SiC or $MoSi_2$ second phase on the oxide layers structureof HfB_2-based composites", ***Ceramics International***, Vol. 43, No. 17, (2017), 15053-15059. https://doi.org/10.1016/j.ceramint.2017.08.031
17. Guérineau, V., Vilmart, G., Dorval, N., Julian-Jankowiak, A. "Comparison of ZrB_2-SiC, HfB_2-SiC and HfB_2-SiC-Y_2O_3 oxidation mechanisms in air using LIF of $BO_2(g)$", ***Corrosion Science***, Vol. 163, (2020), 108278. https://doi.org/10.1016/j.corsci.2019.108278
18. Ghadami, S., Taheri-Nassaj, E., Baharvandi, H. R., Ghadami, F., "Effect of in situ VSi_2 and SiC phases on the sintering behavior and the mechanical properties of HfB_2-based composites", ***Scientific Reports***, Vol. 10, No. 1, (2020), 16540. https://doi.org/10.1038/s41598-020-73295-7
19. Simonenko, E. P., Simonenko, N. P., Lysenkov, A. S., Sevast'yanov, V. G., Kuznetsov, N. T., "Reactive Hot Pressing of HfB_2–SiC–Ta_4HfC_5 Ultra-High Temperature Ceramics", ***Russian Journal of Inorganic Chemistry***, Vol. 65, No. 3, (2020), 446-457. https://doi.org/10.1134/S0036023620030146
20. Simonenko, E. P., Simonenko, N. P., Nagornov, I. A., Sevastyanov, V. G., Kuznetsov, N. T., "Production and oxidation resistance of HfB_2–30 vol% SiC composite powders modified with $Y_3Al_5O_{12}$", ***Russian Journal of Inorganic Chemistry***, Vol. 65, No. 9, (2020), 1416-1423. https://doi.org/10.1134/S003602362009020X
21. Carney, C. M., "Oxidation resistance of hafnium diboride–silicon carbide from 1400 to 2000 ℃", ***Journal of Materials Science***, Vol. 44, No. 20, (2009), 5673-5681. https://doi.org/10.1007/s10853-009-3799-7
22. Carney. C. M, Parthasarathy, T. A., Cinibulk, M. K., "Oxidation resistance of hafnium diboride ceramics with additions of silicon carbide and tungsten boride or tungsten carbide", ***Journal of the American Ceramic Society***, Vol. 94, No. 8, (2011), 2600-2607. https://doi.org/10.1111/j.1551-2916.2011.04462.x
23. Guo, S., "Oxidation and strength retention of HfB_2−SiC composite with La_2O_3 additives", ***Advances in Applied Ceramics***, Vol. 119, No. 4, (2020), 218-223. https://doi.org/10.1080/17436753.2020.1755510
24. Sciti, D., Balbo, A., Bellosi, A., "Oxidation behavior of a pressureless sintered HfB_2–$MoSi_2$ composite", ***Journal of the European Ceramic Society***, Vol. 29, No. 9, (2009), 1809-1815. https://doi.org/10.1016/j.jeurceramsoc.2008.09.018
25. Opila, E., Levine, S., Lorincz, J., "Oxidation of ZrB_2- and HfB_2-based ultra-high temperature ceramics: Effect of Ta conditions", ***Journal of Materials Science***, Vol. 39, No. 19, (2004), 5969-5977. https://doi.org/10.1023/B:JMSC.0000041693.32531.d1
26. Simonenko, E. P., Simonenko, N. P., Gordeev, A. N., Kolesnikov, A. F., Chaplygin, A. V., Lysenkov, A. S., Nagornov, I. A., Sevastyanov, V. G., Kuznetsov, N. T., "Oxidation of HfB_2-SiC-Ta_4HfC_5 ceramic material by a supersonic flow of dissociated air", ***Journal of the European Ceramic Society***, Vol. 41, No. 2, (2021), 1088-1098. https://doi.org/10.1016/j.jeurceramsoc.2020.10.001
27. Bannykh, D., Utkin, A., Baklanova, N., "Effect of chromium additive on sintering and oxidation behavior of HfB2-SiC ceramics", ***Ceramics International***, Vol. 44, No. 11, (2018), 12451-12457. https://doi.org/10.1016/j.ceramint.2018.04.035
28. Kováčová, Z., Bača, Ľ., Neubauer, E., Kitzmantel, M., "Influence of sintering temperature, SiC particle size and Y_2O_3 addition on the densification, microstructure and oxidation resistance of ZrB_2–SiC ceramics", ***Journal of the European Ceramic Society***, Vol. 36, No. 12, (2016), 3041-3049. https://doi.org/10.1016/j.jeurceramsoc.2015.12.028
29. Guo, W. M., Vleugels, J., Zhang, G. J., Wang, P. L., Van der Biest, O., "Effects of Re_2O_3 (Re = La, Nd, Y and Yb) addition in hot-pressed ZrB_2–SiC ceramics", ***Journal of the European Ceramic Society***, Vol. 29, No. 14, (2009), 3063-3068. https://doi.org/10.1016/j.jeurceramsoc.2009.04.021
30. Ren, X., Mo, H., Wang, W., Feng, P., Guo, L., Li, Z., "Ultrahigh temperature ceramic HfB_2-SiC coating by liquid phase sintering method to protect carbon materials from oxidation", ***Materials Chemistry and Physics***, Vol. 217, (2018), 504-512. https://doi.org/10.1016/j.matchemphys.2018.07.018
31. Wang, P., Li, H., Yuan, R., Wang, H., Zhang, Y., Zhao, Z., "The oxidation resistance of two-temperature synthetic HfB_2-SiC coating for the SiC coated C/C composites", ***Journal of Alloys and Compounds***, Vol. 747, (2018), 438-446. https://doi.org/10.1016/j.jallcom.2018.03.043
32. Zapata-Solvas, E., Jayaseelan, D. D., Brown, P. M., Lee, W. E., "Effect of La_2O_3 addition on long-term oxidation kinetics of ZrB_2–SiC and HfB_2-SiC ultra high temperature ceramics", ***Journal of the***

European Ceramic Society, Vol. 34, Vol. 15, (2014), 3535-3548. https://doi.org/10.1016/j.jeurceramsoc.2014.06.004

33. Duran. P, "Phase relationships in the systems HfO_2-La_2O_3 and HfO_2-Nd_2O_3", ***Ceramics International***, Vol. 1, No. 1, (1975), 10-13. https://doi.org/10.1016/0390-5519(75)90032-0
34. Sevastyanov, V. G., Simonenko, E. P., Sevastyanov, D. V., Simonenko, N. P., Stolyarova, V. L., Lopatin, S. I., Kuznetsov, N. T., "Synthesis, vaporization and thermodynamics of ultrafine $Nd_2Hf_2O_7$ powders", ***Russian Journal of Inorganic Chemistry***, Vol. 58, No. 1, (2013), 1-8. https://doi.org/10.1134/S0036023613010178
35. Jaberi Zamharir, M., Shahedi Asl, M., Pourmohammadie Vafa, N., Ghassemi Kakroudi, M., "Significance of hot pressing parameters and reinforcement size on densification behavior of ZrB_2-25 vol% SiC UHTCs", ***Ceramics International***, Vol. 41, No. 5, (2015), 6439-6447. https://doi.org/10.1016/j.ceramint.2015.01.082
36. Ghadami, S., Taheri-Nassaj, E., Baharvandi, H. R., Ghadami, F., "Effect of in situ SiC and $MoSi_2$ phases on the oxidation behavior of HfB_2- based composites", ***Ceramics International***, Vol. 46, No. 12, (2020), 20299-20305. https://doi.org/10.1016/j.ceramint.2020.05.116
37. Vinci, A., Zoli, L., Galizia, P., Sciti, D., "Influence of Y_2O_3 addition on the mechanical and oxidation behavior of carbon fiber reinforced ZrB_2/SiC composites", ***Journal of the European Ceramic Society***, Vol. 40, No. 15, (2020), 5067-5075. https://doi.org/10.1016/j.jeurceramsoc.2020.06.043
38. Wang, P., Li, H., Sun, J., Yuan, R., Zhang, L., Zhang, Y., Li, T., "The effect of HfB_2 content on the oxidation and thermal shock resistance of SiC coating", ***Surface and Coatings Technology***, Vol. 339, (2018), 124-131. https://doi.org/10.1016/j.surfcoat.2018.02.029
39. Jin, H., Meng, S., Zhang, X., Zeng, Q., Niu, J., "Effects of oxidation temperature, time, and ambient pressure on the oxidation of ZrB_2–SiC–graphite composites in atomic oxygen", ***Journal of the European Ceramic Society***, Vol. 36, No. 8, (2016), 1855-1861. https://doi.org/10.1016/j.jeurceramsoc.2016.02.040
40. Parthasarathy, T. A., Rapp, R. A., Opeka, M., Kerans, R. J., "A model for the oxidation of ZrB_2, HfB_2 and TiB_2", ***Acta Materialia***, Vol. 55, No. 17, (2007), 5999-6010. https://doi.org/10.1016/j.actamat.2007.07.027
41. Mallik, M., Ray, K. K., Mitra, R., "Oxidation behavior of hot pressed ZrB_2–SiC and HfB_2–SiC composites", ***Journal of the European Ceramic Society***, Vol. 31, No. 1-2, (2011), 199-215. https://doi.org/10.1016/j.jeurceramsoc.2010.08.018
42. Lespade, P., Richet, N., Goursat, P., "Oxidation resistance of HfB_2–SiC composites for protection of carbon-based materials", ***Acta Astronautica***, Vol. 60, No. 10-11, (2007), 858-864. https://doi.org/10.1016/j.actaastro.2006.11.007
43. Ghadami, F., Aghdam, A. S. R., Zakeri, A., Saeedi, B., Tahvili, P., "Synergistic effect of CeO_2 and Al_2O_3 nanoparticle dispersion on the oxidation behavior of MCrAlY coatings deposited by HVOF", ***Ceramics International***, Vol. 46, No. 4, (2020), 4556-4567. https://doi.org/10.1016/j.ceramint.2019.10.184

Advanced Ceramics Progress: Vol. 8, No. 2, (Spring 2022) 12-26

Materials and Energy Research Center
MERC

Contents lists available at ACERP

Advanced Ceramics Progress

Journal Homepage: www.acerp.ir

Original Research Article

Characterization and Performance Evaluation of Fabricated TFN-RO Membranes in the Presence of MFI Type Zeolite

Safoura Bakhodaye Dehghanpour [a], Fahime Parvizian [b,*], Vahid Vatanpour [c,*]

[a] *PhD Candidate, Department of Chemical Engineering, Faculty of Engineering, Arak University, Arak, Markazi, Iran*
[b] *Associate Professor, Department of Chemical Engineering, Faculty of Engineering, Arak University, Arak, Markazi, Iran*
[c] *Associate Professor, Department of Applied Chemistry, Faculty of Chemistry, Kharazmi University, Tehran, Tehran, Iran*

* Corresponding Authors' Emails: f-parvizian@araku.ac.ir (F. Parvizian); vahidvatanpour@khu.ac.ir (V. Vatanpour)
URL: https://www.acerp.ir/article_154054.html

ARTICLE INFO

Article History:

Received 07 May 2022
Received in revised form 08 August 2022
Accepted 16 August 2022

Keywords:

Reverse Osmosis
Desalination
Interfacial Polymerization
Antifouling

ABSTRACT

Thin Film Composite (TFC) membranes were fabricated by Interfacial Polymerization (IP) of M-Phenylene Diamine (MPD) and Tri-Mesoyl Chloride (TMC) on Polysulfone (PSf) support in the presence of hydrothermally synthesized TS-1 zeolite as an additive blended in the MPD aqueous solution. Formation of the MFI structure (Pentasil Zeolite), presence of extra-framework TiO_2, and zeolite particle size were investigated through X-Ray Diffraction (XRD), Fourier Transform Infrared Spectroscopy (FTIR), and Field Emission Scanning Electron Microscopy (FE-SEM) analyses, respectively. In addition, the effect of the TS-1 zeolite concentration in the range of 0-0.02 wt. % on the desalination and antifouling performance of the reverse osmosis membranes was evaluated in this study. The obtained results revealed that the membrane containing zeolite at the optimal concentration of 0.005 wt. % had the smoothest surface (RMS: 21.05 nm) and lowest contact angle (51.32°), thus exhibiting the best performance in the water flux of 47.5 $Lm^{-2}h^{-1}$ at 15 bars. In addition, compared to the unfilled TFC membrane, the rejection percentage of NaCl was calculated as 96.7 % (2000 ppm). Further, the antifouling ability of the membranes in the face of Bovine Serum Albumin (BSA) showed the excellent fouling resistance of the zeolite-modified membranes.

https://doi.org/10.30501/acp.2022.348785.1094

1. INTRODUCTION

The population growth, climate change, and excessive use of water resources are among the factors threatening the existing water supplies and causing serious problems many communities are facing that significantly increase the demands for new desalination technologies and water resources [1]. Therefore, the seawater desalination and wastewater reuse is an appropriate approach to solving the problem of water scarcity [2]. Desalination technology is classified into thermal and membrane-based processes based on their separation mechanism [3,4]. Membrane separation technology is the most suitable option for separating a wide range of contaminants from water due to its relatively low energy consumption, simple operating process, low required space, and no requirement of chemical additives [5,6]. Due to the simplicity and relatively low cost of the

Please cite this article as: Bakhodaye Dehghanpour, S., Parvizian, F., Vatanpour, V., "Characterization and Performance Evaluation of Fabricated TFN-RO Membranes in the Presence of MFI Type Zeolite", ***Advanced Ceramics Progress***, Vol. 8, No. 2, (2022), 12-26. https://doi.org/10.30501/acp.2022.348785.1094

available types of energy compared to the thermal processes, most water desalination units in the world currently employ Reverse Osmosis (RO) technology [7]. Cellulose acetate and its derivatives as well as Polyamide (PA) are widely used in manufacturing polymeric RO membranes. These membranes are asymmetric that are made of two categories of integrally-skinned asymmetric membranes and Thin Film Composites (TFC) [8,9]. PA-TFC membranes have a major share of the RO membrane market due to their high salt rejection and water flux potency, modification of the TFC membrane layers separately, relatively low overall manufacturing cost, and high mechanical strength [2]. One of the main challenges in application of RO membranes is fouling with contaminants inside the membrane pores or on its surface, which leads to a decrease in the proper performance of the membrane by affecting the water flux, permeation quality, and salt rejection. Therefore, pre-treatment of feed water [10] and modification of the membrane active thin layer with different compounds can be a suitable solution to improvement of the membrane performance and fouling reduction [11]. To this end, many researchers developed different methods such as considering a change in the membrane monomers [12], addition of organic materials [13], surface modification methods (physical and chemical) [14-16], and nanotechnology [17]. Among these procedures, several studies have been conducted to fabricate Thin Film Nanocomposite (TFN) membranes using nanotechnology and introduction of nanomaterials based on some advantageous groups such as hydroxyl and carboxyl into the membrane [18-22]. Several compounds namely Titanium Dioxide (TiO_2) [23-25], Graphene Oxide (GO) [26], Carbon Nano-Tubes (CNTs) [27], Metal-Organic Frameworks (MOFs) [28,29], and zeolites [30,31] are used to enhance water diffusion and salt rejection as well as fouling reduction.

Zeolites are nanomaterials with excellent capability to enhance the membrane performance owing to their chemical stability and good retardation. They are crystalline aluminosilicate materials with uniform pore sizes in which rejection mechanisms are defined based on the ion exchange and molecular screening. In other words, ions with low hydration radii show greater diffusion through the structure of zeolite cavities. In addition, Nano-zeolites facilitate adsorption of cations by presenting negatively charged centers on the membrane surface that can improve the separation performance [17,32]. Jung et al. [33] reported the fabrication of TFC-RO membranes by dispersing NaA zeolite nanoparticles in the PA films. The modified membranes showed better permeability than the unfilled ones. The idea of using zeolite was suggested due to the structure of pores and consequently, hydrophilicity with antibacterial properties led to introduction of membranes with high performance where the flux was twice as high as that of the unmodified membrane in the membrane with the concentration of 0.4 w/v % zeolite. Fathizadeh et al. [34] added NaX nano-zeolite to the PA layer. The fabricated membranes then improved the surface properties, thus ensuring more water permeability than the zeolite-free membrane. The obtained results showed a decrease and increase in the thickness and pore size of the active thin film, respectively. Dong et al. [35] utilized synthesized NaY zeolite nanoparticles to prepare TFN membranes. Zeolite nanoparticles under an optimal loading of 0.15 wt. % zeolite in a diamine solution increased the flux from 39.6 $Lm^{-2}h^{-1}$ in a membrane without zeolite up to 74.17 $Lm^{-2}h^{-1}$ by forming nano-spaces in the interfacial and possessing a porous structure. Of note, the rejection with 2000 ppm feed salt concentration remained constant at about 98.8 %. Cay-Durgun et al. [36] in their experiments increased the water permeation up to 1.4 times of that of the TFC membrane by embedding 0.30 wt. % of Linde type A zeolite to the RO membrane. In addition, the solute rejection in their study increased from 97.4 up to 97.9 %. Membranes fabricated by this zeolite showed better stability than the TFC membrane in long-term desalination. Incorporation of S-Beta zeolite with hydrophilic nature into the PA layer increased the water flux and NaCl rejection from 25.36 to 65.25 $Lm^{-2}h^{-1}$ and from 97 to 97.33 %, respectively at an optimal content of 0.05 wt. % [37].

MFI type zeolites are also used to fabricate membranes containing zeolite nanoparticles [38]. For example, PA composite membranes were synthesized through Interfacial Polymerization (IP) method based on commercial Polysulfone (PSf) substrate in the presence of silicalite to evaluate the desalination performance. The surface roughness of the fabricated membrane was similar to that of the commercial zeolite-free membrane. Increasing the zeolite loading up to 0.5 wt. % increased water flux up to 9.86 $Lm^{-2}h^{-1}$, which was higher than that of the unmodified membrane, but NaCl rejection (98.1) decreased by 50 % as the density of the PA layer decreased [39]. Huang et al. [40] in a study investigated the effect of silicalite-1 with a pore size of 0.56 nm in the TFC membrane and proved that the surface of S-PA membrane was more hydrophilic than that of the bare membrane, hence excellent water permeability and large-scale seawater desalination.

Titanium Silicate-1 (TS-1) is another member of the MFI type that is acknowledged to be a milestone in oxidation reactions as an excellent catalyst [41]. Synthesized by isomorphous substitution of silicon with titanium, this zeolite, similar to Silicalite-1, is characterized by three-dimensional pores and channels with dimensions of 0.56 nm × 0.53 nm. This zeolite is also characterized by a different morphology of regular cubic to irregular blackberry-like [42-44]. So far, this zeolite has been used as an additive in gas separation and pervaporation membranes [45,46]. However, in some limited cases, this zeolite is generally utilized as a zeolite membrane with desalination applications. For example,

Zhang et al. [47] employed the periodic secondary growth method to fabricate the TS-1 bilayer membrane on a seeded support. Such a membrane enjoys a hydrophobic and flawless structure. However, to the best of the authors' knowledge, there is no report on the fabrication of the TFN-RO membrane based on the incorporation of this zeolite as a nanoparticle using the IP method. In this regard, the current study utilized a hydrophilic TS-1 zeolite nanoparticle as an additive to the aqueous phase to fabricate TFN-RO membrane through the IP method. The main objective here was to enhance the membrane performance by taking advantage of the interesting properties of TS-1 such as negative charged groups and molecular sieving properties, to name a few. In order to determine how zeolite concentration affects the membrane performance, a series of TFN membranes were fabricated under different zeolite loadings. In addition, the membranes were characterized followed by their preparation. The characteristics of the RO membranes such as the structure of their surface morphology and hydrophilicity under different zeolite nanoparticle loadings were investigated. Water permeability and separation performance were also evaluated based on the separation tests. Further, the antifouling potential of all membranes in the face of the BSA protein as a foulant was studied. It was expected that followed by the insertion of the TS-1 zeolite into the active thin layer of the TFN-RO membranes, the performance and fouling resistance would significantly improve.

2. EXPERIMENTAL

2.1. Materials

All materials needed for the synthesis of the MFI zeolite namely Tetra-n-butyl orthotitanate (TBOT, 97 wt. %), tetrapropylammonium hydroxide solution (TPAOH, 40 wt. %), tetraethyl orthosilicate (TEOS, 98 wt. %), and isopropanol were purchased from Merck company. In order to fabricate the membrane support, Dimethylformamide (DMF, Merck, Germany) and polysulfone (PSf, MW: 58,000 $gmol^{-1}$, BASF, Germany), and a non-woven polyester fabric were used. In addition, M-Phenylenediamine (MPD, Sigma-Aldrich, USA), triethylamine (TEA, Merck, Germany) and (+) 10-camphor sulfonic acid (CSA, Merck, Germany), trimesoyl chloride (TMC, Merck, Germany), and n-hexane dehydrated by molecular sieve (Merck, Germany) were utilized to obtain the barrier layer. Of note, Bovine serum albumin (BSA, MW: 67,000 $gmol^{-1}$) and NaCl were purchased from Merck company.

2.2. Synthesis of MFI Zeolite

The hydrothermal synthesis of TS-1 zeolite was accomplished according to the protocol proposed by Du et al. [48]. To this end, 7.5 g TEOS was added dropwise into 9.3 g TPAOH (25 % aqueous solution) as a template and 2.3 g distilled water with stirring. After that, 0.32 g TBOT was dissolved in 1.2 g isopropanol and added slowly into the above mixture. The prepared solution was kept stirring for 20 min at 25 °C. To hydrolyze and remove the alcohol, the temperature of the solution was raised up to 70 °C under vigorous stirring for 2 h. Then, 15 g distilled water was added to the precursor mixture and stirring continued for another 20 min. An autoclave with Teflon-lined steel was used to heat the solution for 72 h at 160 °C. To obtain the synthesized zeolite, the resultant product was washed by centrifugation with ethanol and distilled water. Calcination was then performed by calcining the solid at 550 ° C for 6 h after it had been dried overnight at 60 °C.

2.3. Fabrication of TS-1/RO Membrane

The fabrication process of TFC-RO membranes involves two steps: preparing the porous PSf support and generating the PA layer on the support. The phase inversion method was employed to prepare the PSf support. The formulation of the casting solution is as follows: PSf (19 wt. %) should be added into the DMF (81 wt. %) as a solvent and kept stirring until a homogeneous solution is obtained and then, it should be heated for four hours at 50 ° C to eliminate air bubbles. Casting of PSf solution was then conducted using a film applicator on polyester fabric. The cast films were immediately transferred to a bath containing distilled water as the non-solvent and preserved for two hours. The TFC-RO membrane including a PA layer on the support was prepared through interfacial polymerization according to the method proposed by Safarpour et al. [24]. The prepared support was then dipped in a solution containing MPD (2.0 wt. %), TEA (2.0 wt. %), and CSA (2.0 wt. %) for 10 min and then removed. The remained solution was drained of the surface by a glass roller. Subsequently, the MPD-impregnated membrane was fixed on a glass plate, and an organic solution of TMC (0.1 wt. %) in n-hexane was spread on its top surface and allowed to subject for one min. The membrane was washed using n-hexane to remove the unreacted monomers from the surface and then cured for 10 min at 70 °C. To fabricate the TFN membranes containing zeolite, first, the same amount of zeolite was added to the distilled water and n-hexane separately and then, ultrasonication was used for 30 min to evaluate the stability of zeolite dispersion in aqueous and organic phases. The zeolite in the n-hexane was immediately precipitated after ultrasonication while it remained well dispersed in water for hours due to the hydrophilic essence of synthesized zeolite. Accordingly, the membranes containing zeolite were prepared by dispersing different loadings of zeolite (0.002, 0.005, 0.01, and 0.02 wt. % based on the weight of the aqueous solution) in distilled water and then, the zeolite solution was added to the aqueous solution for an IP process. The

rest of the procedure is the same as what was already described. The prepared membranes were called TFC for non-zeolite membrane and TFN-Z-X where X indicates the concentration of zeolite in the aqueous phase.

2.4. Characterization

X-Ray Diffraction (XRD) analysis of TS-1 zeolite was performed using Philips X-ray diffractometer model with the current and voltage of 25 mA and 30 kV, respectively, and CuKα radiation (λ = 0.154 nm). Phase analysis was then performed using X'Pert HighScore Plus version 2.0 software. Further, Attenuated Total Reflection-Fourier Transform Infrared (ATR-FTIR) was taken into consideration to study the membrane surface modification in the range of 650-4000 cm^{-1} by SPECAC Golden Gate (England). Fourier Transform Infrared Spectra (FTIR) was also recorded on Perkin Elmer Spectrum RX1 using KBr pellet method from 400 to 4000 cm^{-1}. Furthermore, Field Emission Scanning Electron Microscopy (FE-SEM) model TESCAN was employed to study the microstructure of the synthesized zeolite as well as the surface and cross-sectional properties of the fabricated membranes. For cross-sectional analysis, all membranes were broken down in liquid nitrogen to prevent deformation. In addition, Energy Dispersive X-ray (EDX) was employed to verify the existence of Ti on zeolite and dispersion of zeolite in the membrane structure. Determination of topology and parameters of the surface roughness of membranes with a 5 µm× 5 µm scan area was recorded through Atomic Force Microscopy (AFM) analysis Park scientific instruments-C_p auto probe model. Moreover, a contact angle analyzer was utilized to assess the hydrophilicity of membrane surfaces. In order to decrease the experimental errors and increase accuracy, the measurements were made at five different membrane points, and the mean contact angle value was calculated.

2.5. Membrane Performance Evaluation

Several experiments were done to evaluate the RO performance considering the pure water flux, NaCl rejection, and antifouling by permeating aqueous solution through the membrane films with the area of 36 cm^2 in a cross-flow filtration system. In order to obtain a steady flux, the membranes were pre-compacted at 20 bars. The experiments were done at the ambient temperature and pressure of 15 bars. The amount of pure water flux is measured through Equation (1).

$$J = \frac{V}{A \times t} \quad (1)$$

where V, A, t, and J are the volume of permeate flux (L), effective area of membrane (m^2), test time (h), and permeate flux ($Lm^{-2}h^{-1}$), respectively.

Moreover, NaCl rejection was determined using 2000 ppm NaCl solution. In addition, the amount of (R(%)) can be calculated through Equation (2).

$$R(\%) = \left(1 - \frac{C_P}{C_f}\right) \times 100 \quad (2)$$

where C_p and C_f indicate the salt concentration in the permeate and feed solution, respectively, both determined by a conductometer.

Followed by adding BSA protein (200 ppm) to the NaCl solution (2000 ppm), the anti-fouling ability of the membranes for 90 min was studied. Also, the permeated water volume was quantified to determine the flux.

To minimize the experimental errors, all experiments were conducted at least three times for each membrane, and their mean values were claculated.

3. RESULTS AND DISCUSSION

3.1. TS-1 Zeolite Characterization

Figure 1a demostrates the XRD pattern of TS-1 zeolite in the range of 2θ=5-60°. As observed, the synthesized zeolite shows the characteristic diffraction peaks of the MFI topology at 2θ=7.9°, 8.8°, 23.0°, 23.9°, and 24.4° [49] that correspond to the d-spacing 11.2, 10.08, 3.86, 3.73, and 3.66 Å, respectively. The diffraction peak of 2θ=25.4° shows the presence of anatase TiO_2. This peak in the XRD pattern of the synthesized zeolite is undetectable mainly due to the high dispersion of TiO_2 formed during zeolite crystallization [48].

Figure 1b illustrates the FTIR spectroscopy of the synthesized zeolite. The appearance of vibration adsorption bands at 552, 807, 960, 1100, and 1230 cm^{-1} agrees with the typical FTIR spectrum of the TS-1 zeolite [50]. The band at 552 cm^{-1}, which is attributed to the vibrations of double five-membered rings, belongs to the characteristic band of MFI topology, and the band at 1230 cm^{-1} corresponds to the TiO_4 and SiO_4 tetrahedral asymmetric stretching in the zeolite structure [49,51]. The band at 552 cm^{-1} and weak band at 628 cm^{-1} are indictive of the presence of TiO_2 [52,53]. The adsorption band at 960 cm^{-1} attributed to the stretching vibration of SiO_4 units adjacent to the structural titanium is indicative of the insertion of Ti into the zeolite framework. Of note, IR absorptions at 451, 807, and 1100 cm^{-1} are said to the internal vibrations of TiO_4 and SiO_4 and the broad band at 3430 cm^{-1} shows the presence of hydroxyl groups [54,55].

Figure 1c presents the FE-SEM image of the morphology and particle diameter of the synthesized zeolite. The average size of the synthesized zeolite particles is about 180 nm, indicating an aggregated structure with a blackberry-like shape [56]. The EDX mapping analysis was then done to ensure the presence of Ti on the zeolite surface, the results of which are given

in Figure 1d. The results confirmed the presence of Ti on the surface of the synthesized zeolite with a relatively uniform distribution (Red dots indicate the presence of Ti). The EDX survey (Figure 1e) was also done to confirm the presence of Ti. One of the notable properties of TS-1 zeolite is the amount of tetrahedral Ti inserted into the zeolite framework, which is substituted by Si atoms. At the same time, this substitution is bound to a restriction. To be specific, given that Ti has a larger atomic radius than that of the stable silicalite-1 structure, it causes changes in the unit cell parameters during insertion.

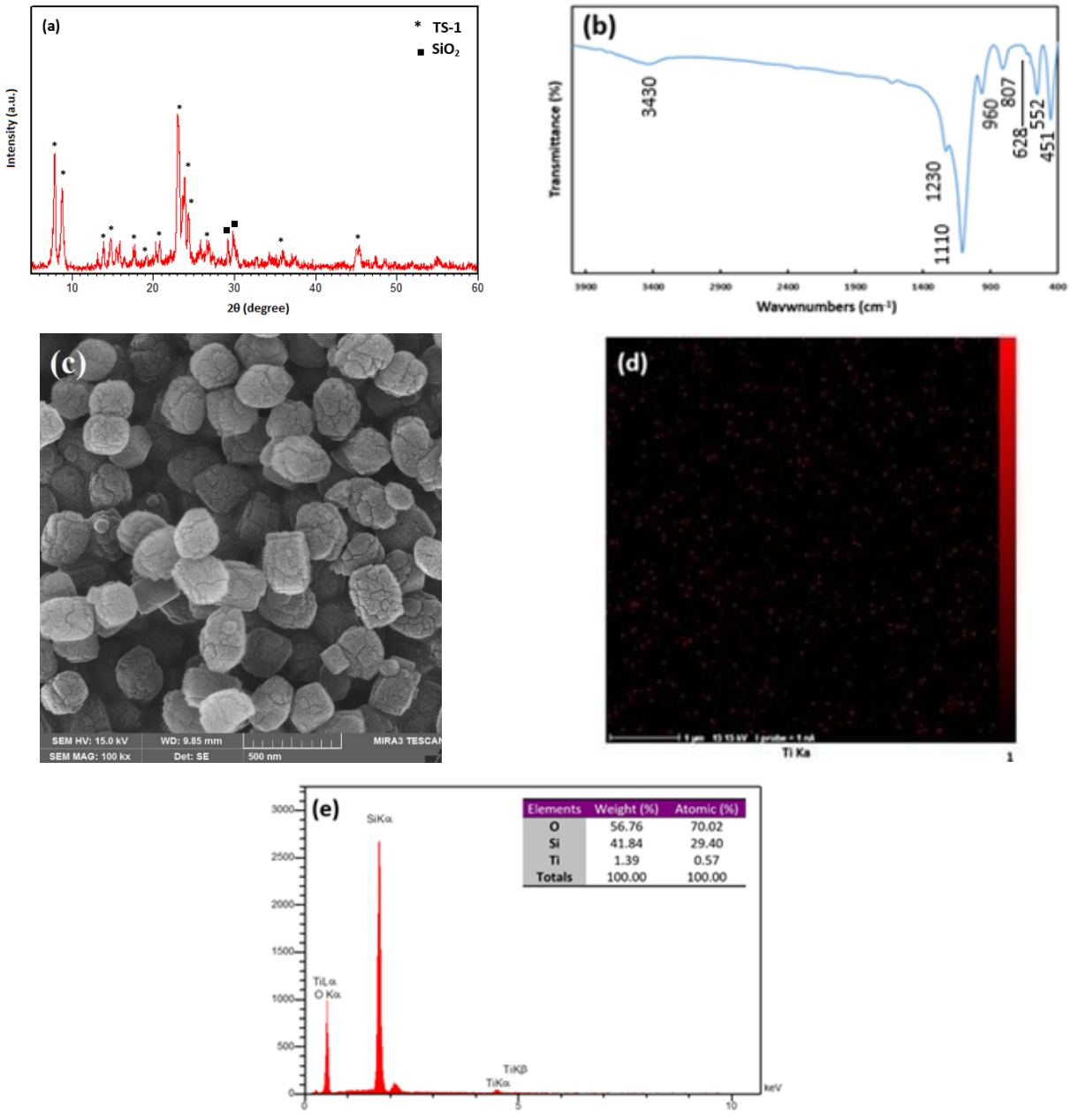

Figure. 1. (a) XRD pattern, (b) FTIR spectrum, (c) FE-SEM image, (d) EDX map of Ti element, and (e) EDX spectrum of the synthesized TS-1 zeolite

According to the results, the highest amount of Ti that can enter the lattice is about 2.5 A while the rest of Ti in the synthesis solution will not be able to enter the scaffold, hence converted to extraframework TiO_2 phases [57]. It should be noted that the presence of extraframework Ti can be confirmed through the FTIR analysis.

3.2. Structure and Properties of the Membranes

FE-SEM analysis was done to assess the surface and cross-sectional morphology of the membranes prior to and followed by the zeolite introduction. Figure 2 shows the effect of different zeolite loadings on the cross-sectional morphology of the fabricated membranes. For all asymmetric membranes, the formation of a PA layer on the spongy structure of the PSf support is observable. According to the images, the thickness and support values of the PA layer were calculated as 250-350 nm and 30-40 µm, respectively. Of note, the thickness of the PA thin film did not change significantly with the introduction of zeolite probably due to the small amount of the used zeolite.

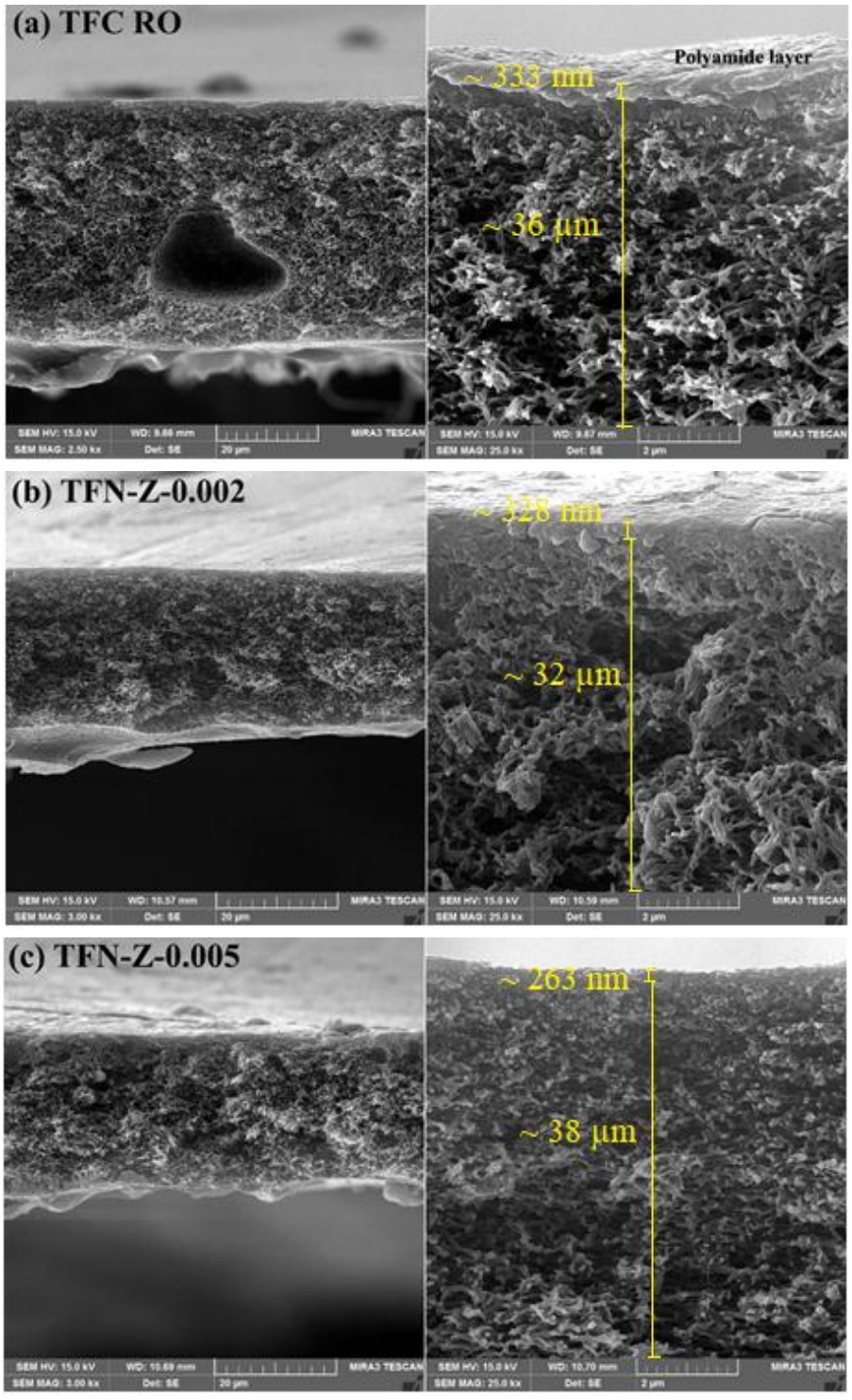

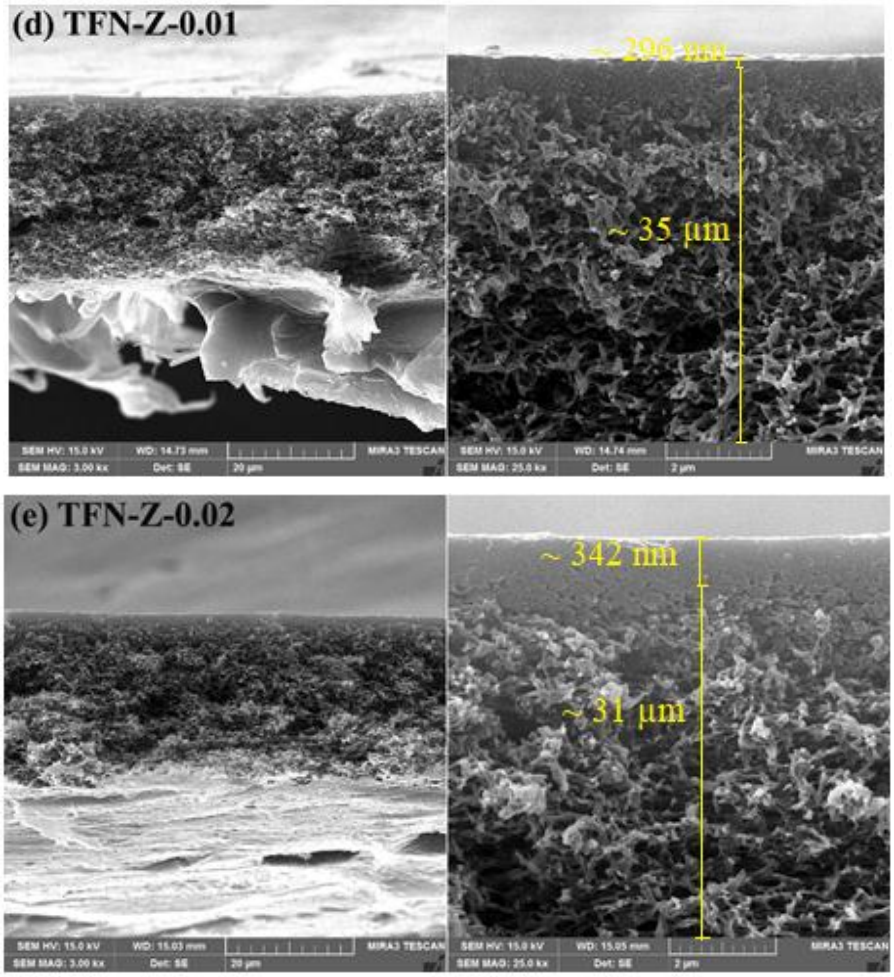

Figure 2. The cross-sectional FE-SEM images of (a) TFC, (b) TFN-Z-0.002, (c) TFN-Z-0.005, (d) TFN-Z-0.01, and (e) TFN-Z-0.02 membranes

Figure 3 shows the upper surface of all membranes. Clearly, all membranes have a hill and valley morphology, which is a common structure among the PA membranes formed through the polymerization of the interface between MPD and TMC [35]. However, it seems that upon adding zeolite to the PA layer, the surface morphology of the membranes will considerably chanege. Upon inserting 0.002 and 0.005 wt. % zeolite into the polymerization solution, the surfaces of the membranes will gradually get smoother than the TFC membrane.

Changes in the miscibility and kinetics of the aqueous and organic solution induced by zeolite as well as the interaction between TS-1 and MPD are the key factors that alter the membrane morphology and reduce the surface roughness [30], as observed in the TFN-Z-0.002 and TFN-Z-0.005 membranes (Figures 3b and 3c, respectively). On the contrary, followed by increasing the zeolite concentration, the surface morphologies of the TFN-Z-0.01 and TFN-Z-0.02 membranes will get rougher probably due to the formation of larger zeolite particles containing smaller particles. Similar trends have been detected by other researchers [58,59]. In order to further investigate the morphology and surface roughness of the fabricated membranes, AFM analysis is discussed in detail in the following.

Given that zeolite particles were indistinguishable on the surface and cross-section of the TFN membranes, the EDX survey was employed to confirm the presence of zeolite (Ti and Si elements) on the TFN-Z-0.005 membrane surface. As illustrated in Figure 4a, the EDX map analysis shows a relatively uniform distribution of zeolite on the membrane surface. In this analysis, green and red dots indicate the attendance of Si and Ti elements on the surface of the zeolite-modified membrane, respectively.

In addition, the EDX spectrum of the modified membrane given in Figure 4b confirms the presence of Ti and Si on the surface of TFN-Z-0.005 membrane, thus confirming the presence of zeolite in TFN membranes.

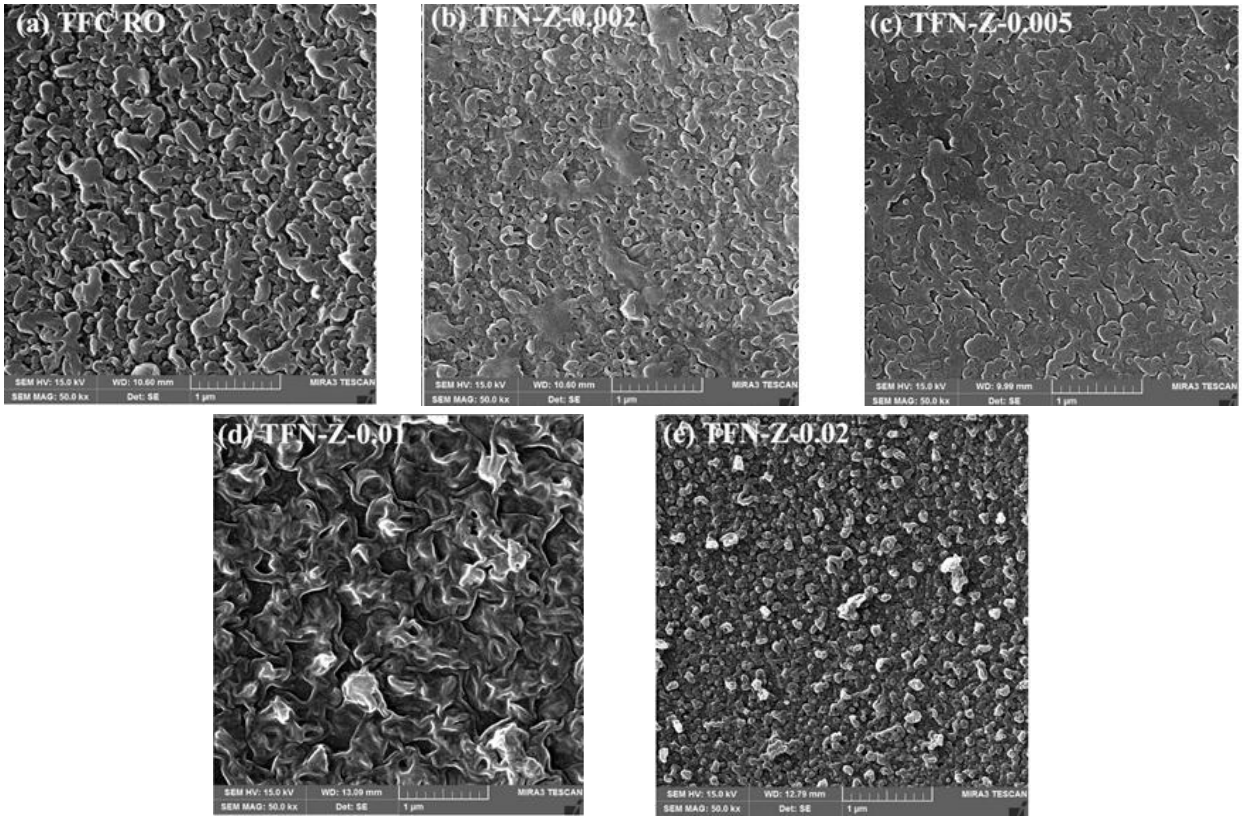

Figure 3. Surface FE-SEM images of (a) TFC, (b) TFN-Z-0.002, (c) TFN-Z-0.005, (d) TFN-Z-0.01, and (e) TFN-Z-0.02 membranes

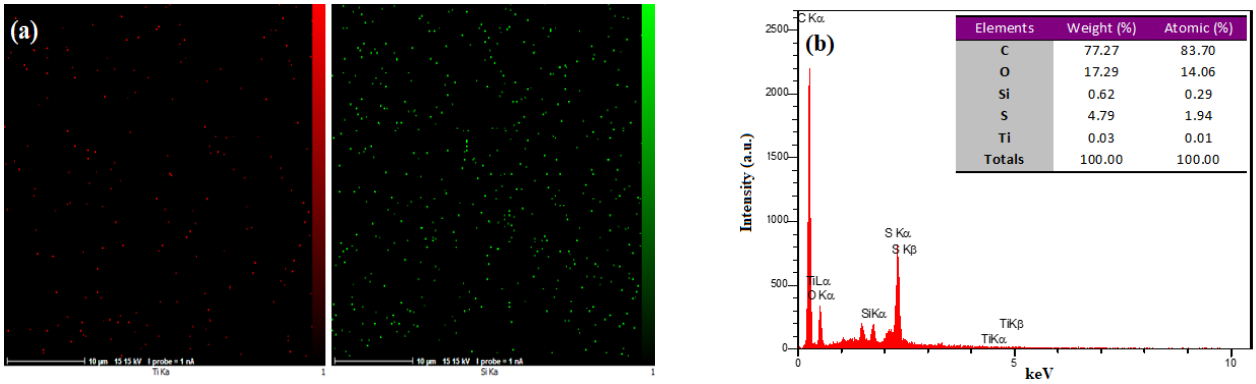

Figure 4. (a) EDX map of Ti and Si element and (b) EDX spectrum of TFN-Z-0.005 membrane

Figure 5 presents the results from the AFM analysis that help examine the surface properties with the scan size of 5 µm × 5 µm. Table 1 lists the average arithmetic (S_a) and Root Mean Square (RMS) roughness as the parameters that determine the surface roughness. The trend observed in this analysis is similar to that in the FE-SEM results according to which, the lowest surface roughness is attributed to the TFN-Z-0.005 membrane with the smoothest surface. As mentioned earlier, the presence of zeolite can change the reaction rate between the organic and aqueous monomers. On the contrary, the chemical bonding between the TiO_2 and PA layer is the reason for the surface roughness reduction [24]. It should be noted that reducing the surface roughness can improve the membrane fouling resistance. Upon increasing the concentration of zeolite introduced into the upper active layer and given the tendency of particles to clump together, we can expect a growth in the surface roughness. The RMS values in TFN-Z-0.01 and TFN-Z-0.02 membranes are 28.58 nm and 38.01 nm, respectively. Such an increase in the surface roughness has also been previously reported by other researchers [36].

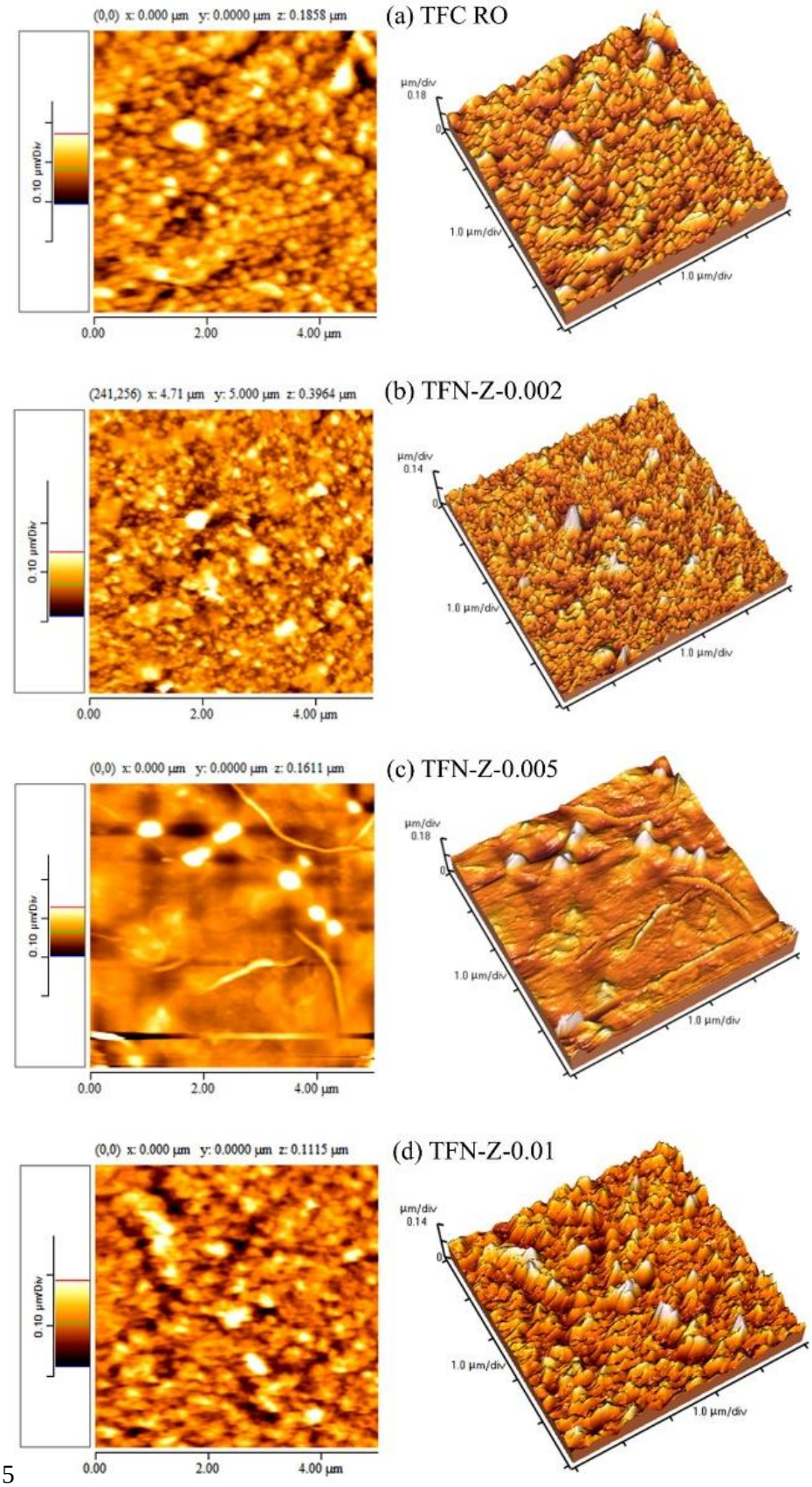
(0,0) x: 0.000 µm y: 0.0000 µm z: 0.1858 µm
(a) TFC RO
0.10 µm/Div
0.00
2.00
4.00 µm
µm/div
0.18
1.0 µm/div
1.0 µm/div
(241,256) x: 4.71 µm y: 5.000 µm z: 0.3964 µm
(b) TFN-Z-0.002
0.14
(0,0) x: 0.000 µm y: 0.0000 µm z: 0.1611 µm
(c) TFN-Z-0.005
(0,0) x: 0.000 µm y: 0.0000 µm z: 0.1115 µm
(d) TFN-Z-0.01

5

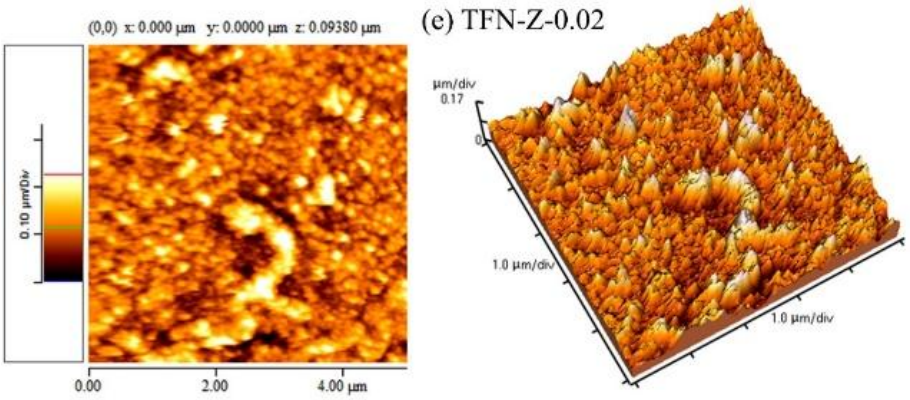

Figure 5. Two- and three-dimensional AFM images of (a) TFC, (b) TFN-Z-0.002, (c) TFN-Z-0.005, (d) TFN-Z-0.01, and (e) TFN-Z-0.02 membranes

Table 1. The surface roughness parameters of the fabricated membranes (5 µm × 5 µm)

Membrane	Roughness parameters	
	RMS (nm)	R_a (nm)
TFC	29.73	22.74
TFN-Z-0.002	21.81	16.15
TFN-Z-0.005	21.05	13.15
TFN-Z-0.01	28.58	21.98
TFN-Z-0.02	38.01	29.18

The surface functional groups of TFC and TFN-Z-0.005 membranes was investigated using the ATR-FTIR analysis. This test makes it possible to pursue the chemical bonds of the membranes. As observed in Figure 6, both membranes have similar absorption bands; however, the appearance of a weak band at 667 cm^{-1} in TFN-Z-0.005 membrane shows the presence of TiO_2. This band in the FTIR analysis is observed at 628 cm^{-1}. This shift may be related to the probable interaction between the active layer and zeolite. Such shift has also been reported in other reseraches in the literature [60]. The characteristic bands at 1548 and 1606 cm^{-1} correspond to the vibration of the amide II and aromatic ring, respectively. These peaks show the formation of the PA layer on the PSf support [39]. The band at 3361 cm^{-1} belongs to the hydroxyl group, and the appearing bands in the range of 1078-1235 cm^{-1} are attributed to the C–N bendings. The bands at 831 and 1485 cm^{-1} appear due to the deformation vibrations of phenyl groups with 1,4 substitution and aromatic ring stretches, respectively. In addition, the bands at 852 and 872 cm^{-1} are attibuted to the characteristics of aromatic hydrogen. The strong band at 1583 cm^{-1} is formed due to the aromatic in-plane ring vibration. The band at 2964 cm^{-1} corresponds to the aromatic C–H stretching and in-plane bending and that at 1502 cm^{-1} to the stretching mode of C=C [61-63].

Figure 7 lists the contact angles of the fabricated membranes important parameters that play a key role in determining the membrane hydrophilicity. The smaller

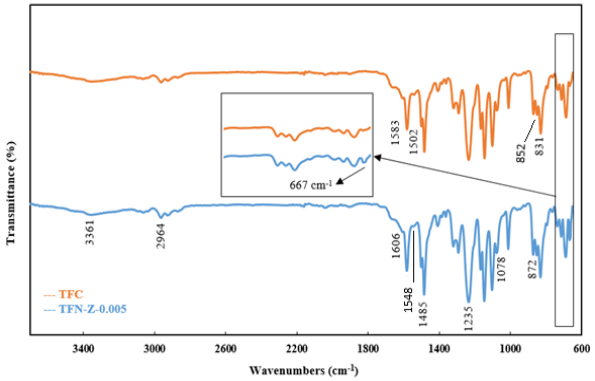

Figure 6. ATR-FTIR spectra of TFC and TFN-Z-0.005 membranes

the contact angle, the higher the hydrophilicity of the membrane. The TFC membrane has a contact angle of 64.44° that decrease with zeolite embedment. The contact angle of TFN-Z-0.005 is 51.32°. The high affinity of TiO_2 group with the negative charge for water molecules is the reason for such a decrease [64]. The contact angles increases upon increasing the zeolite content in both TFN-Z-0.01 and TFN-Z-0.02 membranes. Such behavior results from the aggregation of zeolite particles on the membrane surface under high loadings which in turn leads to a reduction in the effective contact surface of zeolite and consequently membrane hydrophilicity [65].

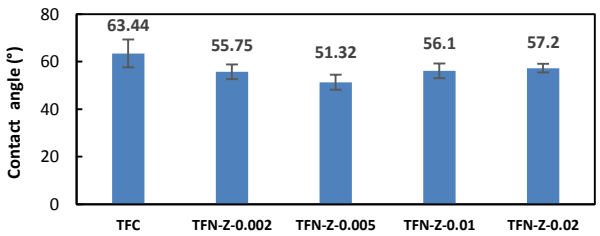

Figure 7. Water contact angle of the TFC membranes PI

3.3. Filtration Performance

In order to evaluate the performance of the fabricated membranes with different zeolite concentrations, the pure water flux values as well as the desalination performance were investigated. Figure 8 presents the water flux of all membranes as a function of the zeolite concentration embedded in the polymer matrix.

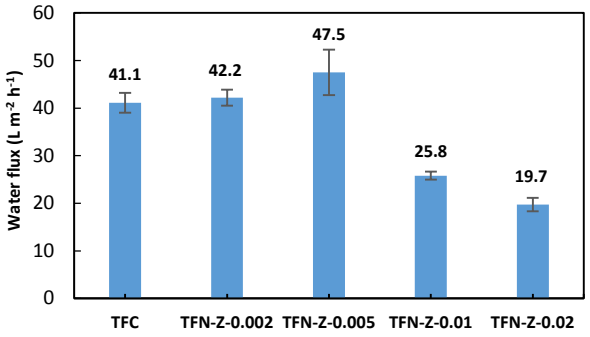

Figure 8. Effect of zeolite concentration on water flux of the fabricated TFC membranes

As reflected, the water flux value for the TFC membrane was obtained as 41.1 $Lm^{-2}h^{-1}$, which grew up to 47.5 $Lm^{-2}h^{-1}$ at the optimal zeolite concentration of 0.005 wt. %. Upon increasing the concentration of the incorporated zeolite, the water flux would sharply decrease. According to Figure 8, the water flux of TFN-Z-0.01 and TFN-Z-0.02 membranes equal 25.8 and 19.7 $Lm^{-2}h^{-1}$, respectively. Improvements in the performance of composite membranes containing nanomaterials were made as a result of variations in the morphology or membrane surface roughness, changes in the PA film cross-linking degree, creation of the preferential diffusion paths for water molecules passage, and changes in the hydrophilicity of the membrane surface with the entry of particles with desirable functional groups such as hydroxyl [66]. In this study, TS-1 zeolite with a three-dimensional pore network larger than water molecules allowed more water to pass through the zeolite-containing membranes compared to the TFC membrane. It should be noted that the presence of extraframework titanium with hydroxyl groups and high affinity to water molecules is another factor that can decrease the water flux. In other words, the bonding between hydroxyl groups of TiO_2 and hydrogen groups in water molecules would improve the membrane hydrophilicity. However, an increase in the zeolite content has a negative effect on water diffusion. With agglomeration and improper distribution of zeolite particles at high concentrations, the amount of effective available pores for the transport of water molecules is reduced, hence a decrease in the water flux [67,68].

To better evaluate the performance of zeolite, the results of salt rejection should be taken into consideration. Figure 9 presents the NaCl rejection values. While the rejection amount in the TFC membrane was 95.01 %, it increased up to 96.78 % with the embedment of 0.005 wt. % zeolite. Negative surface charges of the membranes containing zeolite resulting from the presence of hydroxyl groups of TiO_2 on TS-1 made the electrostatic repulsion reject NaCl. Of note, the pore size of zeolite is smaller than those of Na^+ and Cl^- ions which leads to higher rejection in the TFN membranes than in the TFC. To be specific, the pore size of TS-1 zeolite is 5.6 nm × 5.3 nm [42], and the diameters of the hydrated sodium and chlorine ions are 0.716 nm and 0.664 nm, respectively [69]. The presence of such a pore size will restrict the transport of salt ions. Contrarily, at high concentrations of zeolite, blockage of membranes pores caused by agglomeration of zeolite particles led to an increase in the resistance of TFN-Z-0.01 and TFN-Z-0.02 membranes to the salt passage.

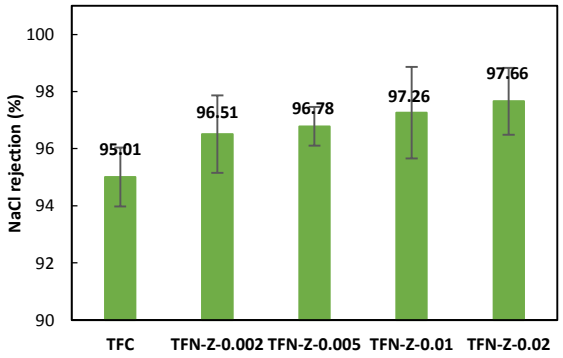

Figure 9. NaCl salt rejection of the fabricated TFC membranes

3.4. Antifouling Performance

Figure 10 shows the antifouling ability of all membranes. The results obtained from examining the a saline solution of 2000 ppm NaCl and 200 ppm BSA indicated that the TFC membrane had the highest flux reduction in the 90 min filtration test, compared to the initial flux. The flux drop in this membrane was 21 % in relation to the initial flux value. However, once TS-1 zeolite was added to the thin active layer, the layer showed high resistance to fouling. In other words, in all membranes containing zeolite, a decrease of less than 10 % of the final flux was observed compared to the flux in the first 10 min filtration. Given that the accumulation of foulants on the membrane surface weakens its performance and increases the operating costs, antifouling potential in the RO membranes gains more significance than ever. Some factors such as feed water properties, hydrodynamic conditions, and membrane surface properties cause fouling [5,10]. Foulant adsorption occurs as a result of the interactions between the membrane surface and foulant as well as some membrane properties such as affinity to water, surface charge, and topology. Increased membrane

hydrophilicity due to the nature of many precipitators can improve membrane fouling resistance.

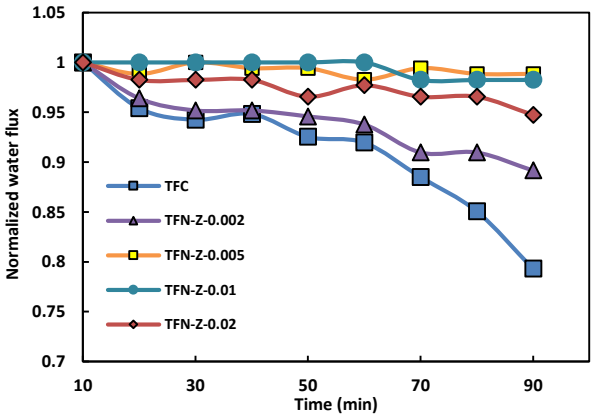

Figure 10. Normalized water flux as a function of BSA/NaCl solution filtration time

Hydrophilic membranes with high surface tensions are able to form hydrogen bonds with the surrounding water molecules which can create an aqueous boundary between the membrane and bulk solution, thus making a severe restriction for the hydrophobic solvent approaching the membrane surface. In case the foulant charge and membrane surface are similar, the electrostatic repulsion force between the membrane and foulant prevents fouling. Increasing the surface negative charge by incorporating functionalities such as hydroxyl can increase the repulsive force with negatively charged foulants namely protein that will subsequentially reduce the membrane fouling. Another important factor in fouling is the roughness of the membrane surfaces. Increased roughness may lead to the formation of a boundary layer or uneven flow distribution on the surface and expand the surface area, thus facilitating the accumulation of foulants on the surface [5]. In membranes containing TS-1 zeolite, the presence of TiO_2 in the PA layer prevents the protein from approaching and adhering to the surface of the membrane by creating a strong repulsive force caused by negative charges to the BSA and also increasing hydrophilicity. In the TFN-Z-0.005 membrane which has the lowest surface roughness according to AFM analysis, the least flux reduction as a result of fouling is observed, indicating an excellent resistance to fouling. In contrast, TFN-Z-0.01 and TFN-Z-0.02 membranes with quite high roughness due to agglomeration of zeolite particles show high resistance to fouling, which may be attributed to the high negative charge density and excretion.

4. CONCLUSION

In this study, TS-1 zeolite with the mean particle size of 180 nm was synthesized based on the hydrothermal method and then added to the polymerization solution to be inserted into a thin film layer of RO composite membranes. The EDX analysis confirmed the presence and relatively uniform distribution of zeolite in the PA layer. The results from the ATR-FTIR analysis also confirmed the presence of TiO_2 on the membrane. Characterized by the hydrophilicity and pore size larger than that of the water molecules at 0.005 wt. % as the optimal concentration of zeolite, the water flux rised from 41.1 $Lm^{-2}h^{-1}$ up to 47.5 $Lm^{-2}h^{-1}$ in the TFC membrane. Evaluation of the findings of the filtration experiments in the membranes containing zeolite indicated their enhanced separation performance and high antifouling potential owing to the negative surface charge produced by TiO_2.

ACKNOWLEDGEMENTS

The authors are grateful to both Arak and Kharazmi Universities for the all supports throughout this research.

NOMENCLATURE

AFM	Atomic Force Microscopy
ATR-FTIR	Attenuated Total Reflection-Fourier Transform Infrared
BSA	Bovine Serum Albumin
CNTs	Carbon Nanotubes
CSA	(+) 10-camphor sulfonic acid
DMF	Dimethylformamide
EDX	Energy Dispersive X-ray
FE-SEM	Field Emission Scanning Electron Microscopy
FTIR	Fourier Transform Infrared spectroscopy
GO	Graphene Oxide
IP	Interfacial Polymerization
MOFs	Metal-Organic Frameworks
MPD	M-Phenylene Diamine
PA	Polyamide
PSf	Polysulfone
RMS	Root Mean Square roughness
RO	Reverse Osmosis
S_a	Average arithmetic roughness
TBOT	Tetra-n-Butyl Orthotitanate
TEA	Triethylamine
TEOS	Tetraethyl orthosilicate
TFC	Thin Film Composite membranes
TFN	Thin Film Nanocomposite
TiO_2	Titanium dioxide
TMC	Tri-Mesoyl Chloride
TPAOH	Tetrapropylammonium hydroxide
TS-1	Titanium silicate-1
XRD	X-Ray Diffraction

REFERENCES

1. Shenvi, S. S., Isloor, A. M., Ismail, A. F., "A review on RO membrane technology: Developments and challenges", ***Desalination***, Vol. 368, (2015), 10-26. https://doi.org/10.1016/j.desal.2014.12.042
2. Hailemariam, R. H., Woo, Y. C., Damtie, M. M., Kim, B. C., Park,

K. D., Choi, J. S., "Reverse osmosis membrane fabrication and modification technologies and future trends: A review", ***Advances in Colloid and Interface Science***, Vol. 276, (2020), 102100. https://doi.org/10.1016/j.cis.2019.102100

3. Greenlee, L. F., Lawler, D. F., Freeman, B. D., Marrot, B, Moulin, P., "Reverse osmosis desalination: Water sources, technology, and today's challenges", ***Water Research***, Vol. 43, No. 9, (2009), 2317-2348. https://doi.org/10.1016/j.watres.2009.03.010
4. Elimelech, M., Phillip, W. A., "The future of seawater desalination: Energy, technology, and the environment", ***Science***, Vol. 333, No. 6043, (2011), 712-717. https://doi.org/10.1126/science.1200488
5. Asadollahi, M., Bastani, D., Musavi, S. A., "Enhancement of surface properties and performance of reverse osmosis membranes after surface modification: A review", ***Desalination***, Vol. 420, (2017), 330-383. https://doi.org/10.1016/j.desal.2017.05.027
6. Cay-Durgun, P., Lind, M. L., "Nanoporous materials in polymeric membranes for desalination", ***Current Opinion in Chemical Engineering***, Vol. 20, (2018), 19-27. https://doi.org/10.1016/j.coche.2018.01.001
7. Al-Karaghouli, A. A., Kazmerski, L. L., "Renewable energy opportunities in water desalination", In Schorr, M. (ed.), ***Desalination, Trends and Technologies***, London, IntechOpen, (2011), 149-184. https://doi.org/10.5772/14779
8. Lee, K. P., Arnot, T. C., Mattia, D., "A review of reverse osmosis membrane materials for desalination—development to date and future potential", ***Journal of Membrane Science***, Vol. 370, No. 1-2, (2011), 1-22. https://doi.org/10.1016/j.memsci.2010.12.036
9. Wang, Y. N., Wang, R., "Reverse osmosis membrane separation technology, In ***Membrane Separation Principles and Applications***, (2019), 1-45. https://doi.org/10.1016/B978-0-12-812815-2.00001-6
10. Jiang, S., Li, Y., Ladewig, B. P., "A review of reverse osmosis membrane fouling and control strategies", ***Science of the Total Environment***, Vol. 595, (2017), 567-583. https://doi.org/10.1016/j.scitotenv.2017.03.235
11. Jhaveri, J. H., Murthy, Z. V. P., "A comprehensive review on anti-fouling nanocomposite membranes for pressure driven membrane separation processes", ***Desalination***, Vol. 379, (2016), 137-154. https://doi.org/10.1016/j.desal.2015.11.009
12. Park, S. J., Kwon, S. J., Kwon, H. E., Shin, M. G., Park, S. H., Park, H., Park, Y. I., Nam, S. E., Lee, J. H., "Aromatic solvent-assisted interfacial polymerization to prepare high performance thin film composite reverse osmosis membranes based on hydrophilic supports", ***Polymer***, Vol. 144, (2018), 159-167. https://doi.org/10.1016/j.polymer.2018.04.060
13. Zhang, Z., Qin, Y., Kang, G., Yu, H., Jin, Y., Cao, Y., "Tailoring the internal void structure of polyamide films to achieve highly permeable reverse osmosis membranes for water desalination", ***Journal of Membrane Science***, Vol. 595, (2020), 117518. https://doi.org/10.1016/j.memsci.2019.117518
14. Zhang, Y., Wan, Y., Pan, G., Shi, H., Yan, H., Xu, J., Guo, M., Wang, Z., Liu, Y., "Surface modification of polyamide reverse osmosis membrane with sulfonated polyvinyl alcohol for antifouling", ***Applied Surface Science***, Vol. 419, (2017), 177-187. https://doi.org/10.1016/j.apsusc.2017.05.047
15. Reis, R., Duke, M., Merenda, A., Winther-Jensen, B., Puskar, L., Tobin, M. J., Orbell, J. D., Dumée, L. F., "Customizing the surface charge of thin-film composite membranes by surface plasma thin film polymerization", ***Journal of Membrane Science***, Vol. 537, (2017), 1-10. https://doi.org/10.1016/j.memsci.2017.05.013
16. Vatanpour, V., Zoqi, N., "Surface modification of commercial seawater reverse osmosis membranes by grafting of hydrophilic monomer blended with carboxylated multiwalled carbon nanotubes", ***Applied Surface Science***, Vol. 396, (2017), 1478-1489. https://doi.org/10.1016/j.apsusc.2016.11.195
17. Saleem, H., Zaidi, S. J., "Nanoparticles in reverse osmosis membranes for desalination: A state of the art review", ***Desalination***, Vol. 475, (2020), 114171. https://doi.org/10.1016/j.desal.2019.114171
18. Mallya, D. S., Yang, G., Lei, W., Muthukumaran, S., Baskaran, K., "Functionalized mos2 nanosheets enabled nanofiltration membrane with enhanced permeance and fouling resistance", ***Environmental Technology & Innovation***, Vol. 27, (2022), 102719. https://doi.org/10.1016/j.eti.2022.102719
19. Tong, Y., Wang, Y., Bian, S., Ge, H., Xiao, F., Li, L., Gao, C., Zhu, G., "Incorporating ag@ RF core-shell nanomaterials into the thin film nanocomposite membrane to improve permeability and long-term antibacterial properties for nanofiltration", ***Science of The Total Environment***, Vol. 839, (2022), 156231. https://doi.org/10.1016/j.scitotenv.2022.156231
20. Wu, C., Xie, Q., Hong, Z., Shen, L., Yu, T., Guo, H., Xiong, Y., Zhang, G., Lu, Y., Shao, W., "Thin-film nanocomposite nanofiltration membrane with enhanced desalination and antifouling performance via incorporating l-aspartic acid functionalized graphene quantum dots", ***Desalination***, Vol. 498, (2021), 114811. https://doi.org/10.1016/j.desal.2020.114811
21. Liao, Z., Zhu, J., Li, X., Van der Bruggen, B., "Regulating composition and structure of nanofillers in thin film nanocomposite (TFN) membranes for enhanced separation performance: A critical review", ***Separation and Purification Technology***, Vol. 266, (2021), 118567. https://doi.org/10.1016/j.seppur.2021.118567
22. Wang, Y., Meng, X., Wu, H., Bian, S., Tong, Y., Gao, C., Zhu, G., "Improving permeability and anti-fouling performance in reverse osmosis application of polyamide thin film nanocomposite membrane modified with functionalized carbon nanospheres", ***Separation and Purification Technology***, Vol. 270, (2021), 118828. https://doi.org/10.1016/j.seppur.2021.118828
23. El-Aassar, A. H. M. A., "Improvement of reverse osmosis performance of polyamide thin-film composite membranes using tio_2 nanoparticles", ***Desalination and Water Treatment***, Vol. 55, No. 11, (2015), 2939-2950. https://doi.org/10.1080/19443994.2014.940206
24. Safarpour, M., Khataee, A., Vatanpour, V., "Thin film nanocomposite reverse osmosis membrane modified by reduced graphene oxide/tio2 with improved desalination performance", ***Journal of Membrane Science***, Vol. 489, (2015), 43-54. https://doi.org/10.1016/j.memsci.2015.04.010
25. Al Mayyahi, A., "TiO_2 polyamide thin film nanocomposite reverses osmosis membrane for water desalination", ***Membranes***, Vol. 8, No. 3, (2018), 66. https://doi.org/10.3390/membranes8030066
26. Chae, H. R., Lee, J., Lee, C. H., Kim, I. C., Park, P. K., "Graphene oxide-embedded thin-film composite reverse osmosis membrane with high flux, anti-biofouling, and chlorine resistance", ***Journal of Membrane Science***, Vol. 483, (2015), 128-135. https://doi.org/10.1016/j.memsci.2015.02.045
27. Baek, Y., Kim, H. J., Kim, S. H., Lee, J. C., Yoon, J., "Evaluation of carbon nanotube-polyamide thin-film nanocomposite reverse osmosis membrane: Surface properties, performance characteristics and fouling behavior", ***Journal of Industrial and Engineering Chemistry***, Vol. 56, (2017), 327-334. https://doi.org/10.1016/j.jiec.2017.07.028
28. Liu, Y., Wang, X. P., Zong, Z. A., Lin, R., Zhang, X. Y., Chen, F. S., Zhang, L. L., Meng, X. M., Hou, J., "Thin film nanocomposite membrane incorporated with 2D-MOF nanosheets for highly efficient reverse osmosis desalination", ***Journal of Membrane Science***, Vol. 653, (2022), 120520. https://doi.org/10.1016/j.memsci.2022.120520
29. Shukla, A. K., Alam, J., Alhoshan, M. S., Ali, F. A. A., Mishra, U., Hamid, A. A., "Thin-film nanocomposite membrane incorporated with porous zn-based metal–organic frameworks: Toward enhancement of desalination performance and chlorine

resistance", ***ACS Applied Materials & Interfaces***, Vol. 13, No. 24, (2021), 28818-28831. https://doi.org/10.1021/acsami.1c05469

30. Safarpour, M., Vatanpour, V., Khataee, A., Zarrabi, H., Gholami, P., Yekavalangi, M. E., "High flux and fouling resistant reverse osmosis membrane modified with plasma treated natural zeolite", ***Desalination***, Vol. 411, (2017), 89-100. https://doi.org/10.1016/j.desal.2017.02.012
31. Dehghanpour, S. B., Parvizian, F., Vatanpour, V., He, T., "Enhancing the flux and salt rejection of thin-film composite nanofiltration membranes prepared on plasma-treated polyethylene using PVA/TS-1 composite", ***Reactive and Functional Polymers***, Vol. 177, (2022), 105329. https://doi.org/10.1016/j.reactfunctpolym.2022.105329
32. Bandehali, S., Parvizian, F., Moghadassi, A., Hosseini, S. M., "Chapter 5 - Nanomaterials for the efficient abatement of wastewater contaminants by means of reverse osmosis and nanofiltration, in Nanomaterials for the detection and removal of wastewater pollutants", In ***Nanomaterials for the Detection and Removal of Wastewater Pollutants***, Elsevier, (2020), 111-144. https://doi.org/10.1016/B978-0-12-818489-9.00005-0
33. Jeong, B. H., Hoek, E. M., Yan, Y., Subramani, A., Huang, X., Hurwitz, G., Ghosh, A. K, Jawor, A., "Interfacial polymerization of thin film nanocomposites: A new concept for reverse osmosis membranes", ***Journal of Membrane Science***, Vol. 294, No. 1-2, (2007), 1-7. https://doi.org/10.1016/j.memsci.2007.02.025
34. Fathizadeh, M., Aroujalian, A., Raisi, A., "Effect of added NaX nano-zeolite into polyamide as a top thin layer of membrane on water flux and salt rejection in a reverse osmosis process", ***Journal of Membrane Science***, Vol. 375, No. 1-2, (2011), 88-95. https://doi.org/10.1016/j.memsci.2011.03.017
35. Dong, H., Zhao, L., Zhang, L., Chen, H., Gao, C., Ho, W. W., "High-flux reverse osmosis membranes incorporated with NaY zeolite nanoparticles for brackish water desalination", ***Journal of Membrane Science***, Vol. 476, (2015), 373-383. https://doi.org/10.1016/j.memsci.2014.11.054
36. Cay-Durgun, P., McCloskey, C., Konecny, J., Khosravi, A., Lind, M. L., "Evaluation of thin film nanocomposite reverse osmosis membranes for long-term brackish water desalination performance", ***Desalination***, Vol. 404, (2017), 304-312. https://doi.org/10.1016/j.desal.2016.10.014
37. Marioryad, H., Ghaedi, A. M., Emadzadeh, D., Baneshi, M. M., Vafaei, A., Lau, W. J., "A thin film nanocomposite reverse osmosis membrane incorporated with S-Beta zeolite nanoparticles for water desalination", ***ChemistrySelect***, Vol. 5, No. 6, (2020), 1972-1975. https://doi.org/10.1002/slct.201904084
38. Liu, Y., Chen, X., "High permeability and salt rejection reverse osmosis by a zeolite nano-membrane", ***Physical Chemistry Chemical Physics***, Vol. 15, No. 18, (2013), 6817-6824. https://doi.org/10.1039/C3CP43854F
39. Li, D., He, L., Dong, D., Forsyth, M., Wang, H., "Preparation of silicalite–polyamide composite membranes for desalination", ***Asia-Pacific Journal of Chemical Engineering***, Vol. 7, No. 3, (2012), 434-441. https://doi.org/10.1002/apj.588
40. Huang, H., Qu, X., Ji, X., Gao, X., Zhang, L., Chen, H, Hou, L., "Acid and multivalent ion resistance of thin film nanocomposite ro membranes loaded with silicalite-1 nanozeolites", ***Journal of Materials Chemistry A***, Vol. 1, No. 37, (2013), 11343-11349. https://doi.org/10.1039/C3TA12199B
41. Taramasso, M., Perego, G., Notari, B., SnamProgetti S. p. A., ***Preparation of Porous Crystalline Synthetic Material Comprised of Silicon and Titanium Oxides***, U.S. Patent 4,410,501A, (1983). Available at: https://patents.google.com/patent/US4410501A/en (Accessed: 07 September 2022).
42. Clerici, M. G., "Titanium silicalite-1", In Jackson, D., Hargreaves, S. J., (eds.), ***Metal Oxide Catalysis***, (2008), 705-754. https://doi.org/10.1002/9783527626113.ch18
43. Zuo, Y., Song, W., Dai, C., He, Y., Wang, M., Wang, X., Guo, X., "Modification of small-crystal titanium silicalite-1 with organic bases: Recrystallization and catalytic properties in the hydroxylation of phenol", ***Applied Catalysis A: General***, Vol. 453, (2013), 272-279. https://doi.org/10.1016/j.apcata.2012.12.027
44. Chen, L., Wang, Y. M., He, M. Y., "Hydrothermal synthesis of hierarchical titanium silicalite-1 using single template", ***Materials Research Bulletin***, Vol. 46, No. 5, (2011), 698-701. https://doi.org/10.1016/j.materresbull.2011.01.015
45. Han, X., Zhang, X., Ma, X., Li, J., "TS-1 molecular sieves filled polydimethylsiloxane membranes for ethanol/water separation via pervaporation", ***Polymer Engineering & Science***, Vol. 56, No. 5, (2016), 583-589. https://doi.org/10.1002/pen.24283
46. Martin-Gil, V., Lopez, A., Hrabanek, P., Mallada, R., Vankelecom, I. F. J., Fila, V., "Study of different titanosilicate (TS-1 and ETS-10) as fillers for mixed matrix membranes for CO_2/CH_4 gas separation applications", ***Journal of Membrane Science***, Vol. 523, (2017), 24-35. https://doi.org/10.1016/j.memsci.2016.09.041
47. Zhang, Q., Liu, Y., Liu, X., Ma, L., "Facile preparation of bilayer titanium silicate (TS-1) zeolite membranes by periodical secondary growth", ***Coatings***, Vol. 9, No. 12, (2019), 850. https://doi.org/10.3390/coatings9120850
48. Du, Q., Guo, Y., Duan, H., Li, H., Chen, Y., Liu, H., "Synthesis of hierarchical ts-1 zeolite via a novel three-step crystallization method and its excellent catalytic performance in oxidative desulfurization", ***Fuel***, Vol. 188, (2017), 232-238. https://doi.org/10.1016/j.fuel.2016.10.045
49. Zuo, Y., Liu, M., Zhang, T., Meng, C., Guo, X., Song, C., "Enhanced catalytic performance of titanium silicalite-1 in tuning the crystal size in the range 1200–200 nm in a tetrapropylammonium bromide system", ***ChemCatChem***, Vol. 7, No. 17, (2015), 2660-2668. https://doi.org/10.1002/cctc.201500440
50. Liu, M., Chang, Z., Wei, H., Li, B., Wang, X., Wen, Y., "Low-cost synthesis of size-controlled ts-1 by using suspended seeds: From screening to scale-up", ***Applied Catalysis A: General***, Vol. 525, (2016), 59-67. https://doi.org/10.1016/j.apcata.2016.07.006
51. Du, Q., Guo, Y., Wu, P., Liu, H., Chen, Y., "Facile synthesis of hierarchical TS-1 zeolite without using mesopore templates and its application in deep oxidative desulfurization", ***Microporous and Mesoporous Materials***, Vol. 275, (2019), 61-68. https://doi.org/10.1016/j.micromeso.2018.08.018
52. Astorino, E., Peri, J. B., Willey, R. J., Busca, G., "Spectroscopic characterization of silicalite-1 and titanium silicalite-1", ***Journal of Catalysis***, Vol. 157, No. 2, (1995), 482-500. https://doi.org/10.1006/jcat.1995.1313
53. Tekin, D., Birhan, D., Kiziltas, H., "Thermal, photocatalytic, and antibacterial properties of calcinated nano-TiO_2/polymer composites", ***Materials Chemistry and Physics***, Vol. 251, (2020), 123067. https://doi.org/10.1016/j.matchemphys.2020.123067
54. Bandehali, S., Moghadassi, A., Parvizian, F., Shen, J., Hosseini, S. M., "Glycidyl POSS-functionalized ZnO nanoparticles incorporated polyether-imide based nanofiltration membranes for heavy metal ions removal from water", ***Korean Journal of Chemical Engineering***, Vol. 37, No. 2, (2020), 263-273. https://doi.org/10.1007/s11814-019-0441-5
55. Xue, T., Liu, H., Wang, Y., Wu, H., Wu, P., He, M., "Seed-induced synthesis of small-crystal TS-1 using ammonia as alkali source", ***Chinese Journal of Catalysis***, Vol. 36, No. 11, (2015), 1928-1935. https://doi.org/10.1016/S1872-2067(15)60955-X
56. Lin, J., Yang, T., Lin, C., Sun, J., "Hierarchical MFI zeolite synthesized via regulating the kinetic of dissolution-recrystallization and their catalytic properties", ***Catalysis Communications***, Vol. 115, (2018), 82-86. https://doi.org/10.1016/j.catcom.2018.07.006
57. Notari, B., "Microporous crystalline titanium silicates", In

Advances in Catalysis, Academic Press, Vol. 41, (1996), 253-334. https://doi.org/10.1016/S0360-0564(08)60042-5

58. Namvar-Mahboub, M., Pakizeh, M., Davari, S., "Preparation and characterization of UZM-5/polyamide thin film nanocomposite membrane for dewaxing solvent recovery", ***Journal of Membrane Science***, Vol. 459, (2014), 22-32. https://doi.org/10.1016/j.memsci.2014.02.014
59. Wang, L., Fang, M., Liu, J., He, J., Deng, L., Li, J., Lei, J., "The influence of dispersed phases on polyamide/ZIF-8 nanofiltration membranes for dye removal from water", ***RSC Advances***, Vol. 5, No. 63, (2015), 50942-50954. https://doi.org/10.1039/C5RA06185G
60. Vatanpour, V., Madaeni, S. S., Khataee, A. R., Salehi, E., Zinadini, S., Monfared, H. A., "TiO_2 embedded mixed matrix PES nanocomposite membranes: Influence of different sizes and types of nanoparticles on antifouling and performance", ***Desalination***, Vol. 292, (2012), 19-29. https://doi.org/10.1016/j.desal.2012.02.006
61. Huang, H., Qu, X., Dong, H., Zhang, L., Chen, H., "Role of NaA zeolites in the interfacial polymerization process towards a polyamide nanocomposite reverse osmosis membrane", ***RSC Advances***, Vol. 3, No. 22, (2013), 8203-8207. https://doi.org/10.1039/C3RA40960K
62. Abdel-Hameed, M., ElFadl, M. M. A., Ali, M. E., Kotp, Y. H., Shawky, H. A., "Effect of manufacture conditions on reverse osmosis desalination performance of polyamide thin film composite membrane and their spiral wound element", ***Desalination and Water Treatment***, Vol. 69, (2017), 65-71. https://doi.org/10.5004/dwt.2017.20293
63. Gryta, M., Bastrzyk, J., Lech, D., "Evaluation of fouling potential of nanofiltration membranes based on the dynamic contact angle measurements", ***Polish Journal of Chemical Technology***, Vol. 14, No. 3, (2012), 97-104. https://doi.org/10.2478/v10026-012-0091-4
64. Safarpour, M., Vatanpour, V., Khataee, A., "Preparation and characterization of graphene oxide/TiO_2 blended PES nanofiltration membrane with improved antifouling and separation performance", ***Desalination***, Vol. 393, (2016), 65-78. https://doi.org/10.1016/j.desal.2015.07.003
65. Anis, S. F., Hashaikeh, R., Hilal, N., "Flux and salt rejection enhancement of polyvinyl (alcohol) reverse osmosis membranes using nano-zeolite", ***Desalination***, Vol. 470, (2019), 114104. https://doi.org/10.1016/j.desal.2019.114104
66. Wang, F., Zheng, T., Xiong, R., Wang, P., Ma, J., "Strong improvement of reverse osmosis polyamide membrane performance by addition of ZIF-8 nanoparticles: Effect of particle size and dispersion in selective layer", ***Chemosphere***, Vol. 233, (2019), 524-531. https://doi.org/10.1016/j.chemosphere.2019.06.008
67. Borjigin, B., Yu, L., Xu, L., Zhao, C., Wang, J., "Influence of incorporating beta zeolite nanoparticles on water permeability and ion selectivity of polyamide nanofiltration membranes", ***Journal of Environmental Sciences***, Vol. 98, (2020), 77-84. https://doi.org/10.1016/j.jes.2020.04.010
68. Parvizian, F., Ansari, F., Bandehali, S., "Oleic acid-functionalized TiO_2 nanoparticles for fabrication of PES-based nanofiltration membranes", ***Chemical Engineering Research and Design***, Vol. 156, (2020), 433-441. https://doi.org/10.1016/j.cherd.2020.02.019
69. Duke, M. C., Zhu, B., Doherty, C. M., Hill, M. R., Hill, A. J., Carreon, M. A., "Structural effects on SAPO-34 and ZIF-8 materials exposed to seawater solutions, and their potential as desalination membranes", ***Desalination***, Vol. 377, (2016), 128-137. https://doi.org/10.1016/j.desal.2015.09.004

Advanced Ceramics Progress: Vol. 8, No. 2, (Spring 2022) 27-33

Materials and Energy Research Center
MERC

Contents lists available at ACERP

Advanced Ceramics Progress

Journal Homepage: www.acerp.ir

Original Research Article

Microstructure, Densification, and Compressive Properties of Al-CNT Metal Matrix Composites Fabricated by Flake Powder Metallurgy and Conventional Sintering Process

Mohammad Reza Akbarpour [a, *]

[a] *Associate Professor, Department of Materials Engineering, Faculty of Engineering, University of Maragheh, Maragheh, East Azerbaijan, Iran*

* Corresponding Author Email: akbarpour@maragheh.ac.ir (M. R. Akbarpour) URL: https://www.acerp.ir/article_155462.html

ARTICLE INFO

Article History:

Received 18 July 2022
Received in revised form 25 August 2022
Accepted 30 August 2022

Keywords:

Aluminum Alloys
Composite
Carbon Nanotube
Powder Metallurgy

ABSTRACT

In this study, flake-like aluminum reinforced with different volume fractions of carbon nanotubes (CNTs) was prepared by mechanical milling and conventional sintering at 600 °C under argon atmosphere. To this end, X-Ray Diffraction (XRD) and Scanning Electron Microscopy (SEM) were used to investigate the microstructure of the powders and bulk composite samples. Compression tests were also conducted on the samples to determine their mechanical properties. The obtained results showed that flake powder metallurgy was an effective method for dispersing CNTs on the surface of Al particles. At the sintering temperature of 600 °C, the highest relative density was obtained for the composites. The compression test results showed that the amount of CNT less than 2 vol. % caused an increase in the yield and compressive strength values as well as Young's modulus. However, the values of the mentioned factors decreased in higher volume percentages. Finally, the contributions of the load bearing and grain size refinement strengthening mechanisms on the final strength of the composites were addressed.

https://doi.org/10.30501/acp.2022.352359.1098

1. INTRODUCTION

Today, aluminum-carbon nanotube (Al-CNT) composites are praised for their mechanical properties such as their high wear and corrosion resistance, enhanced tensile strength, and high hardness as well as their low density, excellent electrical, and thermal properties, especially in automotive and aerospace industries [1-3]. Different methods have been developed to fabricate these composites, among the most significant of which are thermal sprays, powder metallurgy (mechanical mills) and sintering, hot extrusion, casting, etc. [4,5].

The distribution of CNTs, depending on the production method, affects the mechanical properties of Al-CNT composites. A number of challenges still remain in the metals reinforced with CNTs, including poor dispersion of CNTs in Al matrix due to agglomeration, low wettability between nanotubes and Al surfaces, and Van der Waals forces between CNTs [6-8].

Different methods such as ultrasonication of CNTs in a solvent before adding CNTs to the matrix, ball milling, coating of the CNTs using some specific metals, etc. have been used to better distribute the CNTs in the Al matrix [9]. Flake powder metallurgy is a new method that is extensively used to provide better distribution of CNTs

Please cite this article as: Akbarpour, M. R., "Microstructure, Densification, and Compressive Properties of Al-CNT Metal Matrix Composites Fabricated by Flake Powder Metallurgy and Conventional Sintering Process", ***Advanced Ceramics Progress***, Vol. 8, No. 2, (2022), 27-33. https://doi.org/10.30501/acp.2022.352359.1098

on metal particles [1,4,6]. Given a highly specific surface area and flat surface of the powder in this method, this method facilitates the surface in situ reaction and reinforcement dispersion, thereby creating flake Nano-Grains (NG) and Ultra-Fine Grains (UFG). It is possible to retain fine microstructures in bulk materials once they are formed. In the case of the destruction of the flake shape of the powder through the powder consolidation process, either a layered configuration or a nano-reinforced body dispersion structure will be formed [10]. This method was also used for ensuring the well-distribution of CNTs in the Al matrix in previous research studies [4,7]. Jiang et al. [11] used the flake powder metallurgy that was developed to fabricate biomimetic Al_2O_3/Al composites. They used nanoflake Al powders with native Al_2O_3 skins as the building blocks to rapidly assemble them into biomimetic nano-laminated structures by compacting and extrusion, thus resulting in strong and ductile composites with the tensile strength of 262 MPa and plasticity of 22.9 %. In recent years, Al-CNT composites with different CNT contents and consolidation methods have been obtained from flake powders [10,12-16]. Of note, the Al-CNT composites fabricated through this method is characterized by superior mechanical properties to those of other composites formed by conventional methods [12,14-16]. In this study, Al-CNT flake powders with different CNT content were fabricated using mechanical milling and then consolidated using uniaxial pressing and sintering at different temperatures. This study also investigated the effects of the CNT content and sintering temperature on densification and mechanical properties.

2. EXPERIMENTAL

In this study, the particle size of the aluminum powder is less than 5 µm with the purity of > 99.5 %, and the outer diameter of the CNT powder is 40 nm with the purity of 99 %. Using a planetary mill, monolithic Al and Al-2 vol. % CNT, Al-4 vol. % CNT, and Al-8 vol. % CNT powders were separately milled for three hours to achieve homogeneous nanotube distribution. Here, the ball-to-powder ratio and rotational speed values were obtained as 10:1 and 200 rpm, respectively, and 12 mm balls, stainless-steel balls, and cups were used. Followed by milling, the samples were compressed at the pressure of 1 GPa and then sintered at the temperature of 600 °C under Ar atmosphere for an hour. The inner diameter of the steel mold was 6 mm. The green samples were prepared by compressing the die at the load of 2881.7 Kgf. A D8 Advance Bruker diffractometer and Mira 3-XMU Field Emission Scanning Electron Microscopy (FE-SEM) were employed to investigate the microstructure of the materials. In order to record the XRD patterns using Cu Kα radiation, step size of 0.02° were used. Archimedes method was also used to determine the density values, and the compressive test with a speed of 1 mm/min was done to determine the mechanical properties. For compression tests, cylindrical specimens with diameters of 6 mm and heights of 9 mm were used. The obtained results from the three tests conducted on each sample were then averaged and taken into consideration.

3. RESULTS AND DISCUSSION

3.1. Microstructure of the Milled Powders Ation

Figure 1 shows the SEM images of primary Al, three-hour-milled Al and Al-8 vol. % CNT composite powders. High-energy milling repeatedly involves fattening, cold welding, fractureing, and rewelding of powder particles [17]. In the case of a collision between two steel balls, a small amount of CNT powders would be trapped in between Al powders. In addition, plastic deformation of the powder particles occurs as a result of the impact force, hence flattening, hardening, and fracture of particles. By creating new surfaces, the particles can weld together,

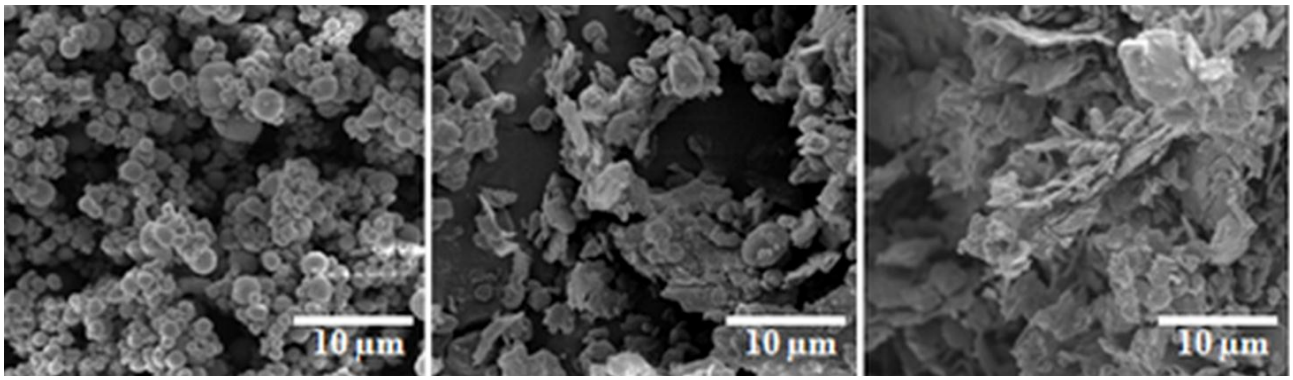

(a) (b) (c)

Figure 1. Morphology of (a) as received Al, (b) Milled Al for 3h, and (c) milled Al-8 vol. % CNT for 3h

thus resulting in their larger size [18,19]. In the early stages of milling (three-hour milling time in this study), the Al particles are soft and consequently, they tend to weld together and form large particles. In this stage, the composite particles have a flake structure composed of a mixture of the constituents. Figure 1a shows the Al powder with spherical morphology. Figures 1b and 1c show the Al and Al-8 vol. % CNT powders, respectively, after three hours of milling.

As a result of milling, flake-shaped powders will be formed. High surface area flakes facilitate CNT dispersion. In Figure 2a, high magnification SEM micrographs show the dispersion of CNTs on the surface of flake Al powders. According to this figure, CNTs were well dispersed. Figure 2b shows the XRD patterns for samples in the (111) planes. The peak in Al with high CNT content is wider and less intense than the others. During three hours of ball milling, addition of CNT to Al facilitated the microstructural evolution. In the presence of CNT reinforcement, the Al matrix undergoes inhomogeneous local deformation which results in a higher work hardening rate, hence finer crystallite sizes of the milled powder, as already reported in previous studies [1,4,8].

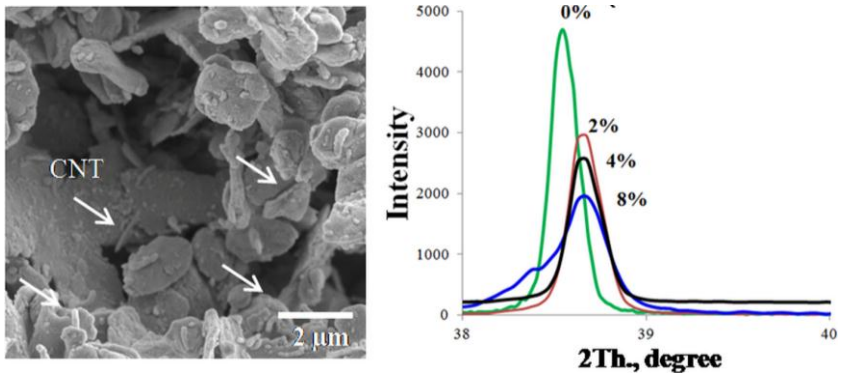

(a) (b)

Figure 2. High magnification SEM micrograph of milled Al-2 vol. % CNT powder showing the dispersion of CNTs on flake powders, and (b) XRD patterns of the samples from the (111) planes

3.2. Sintering Behavior and Microstructure

The milled powders were compressed at the pressure of 1 GPa and then sintered at the temperature of 600 °C. Table 1 shows the density and relative density of the samples measured by Archimedes method.

Table 1. Density and grain size of the bulk samples with different CNT contents

Material	Density (g/cm^3)	Relative Density	Grain Size (nm)
Al	2.47	91.4	220
Al-2 vol. % CNT	2.38	88.9	163
Al-4 vol. % CNT	2.32	87.5	161
Al-8 vol. % CNT	2.28	87.6	156

As seen, the density and relative density of Al decreased by adding CNTs which can be attributed to the presence of some CNT agglomerates in the structure and poor bonding of CNTs with the matrix. This behaviour was already reported for Al-CNT composites prepared through other powder metallurgy methods [4].

Figure 3 shows the microstructure of Al-CNT composites with polished and etched surfaces. As observed in this figure, CNT content caused a decrease in the grain size of Al matrix. In addition, the grain size of the Al matrix remains in the submicron range where the CNT content is a determining factor.

Based on the SEM micrographs, the average grain sizes of the samples were determined using the intercept method. Table 1 presents the grain size values for different samples. The decrease in the grain size of the composite samples is the result of pinning effect of CNT during sintering [20].

Figure 4 demonstrates the XRD patterns of the sintered samples. Due to the small volume fraction of CNTs and their nanometer size, only the peaks related to FCC Al can be observed. According to this figure, the intensity of the diffraction peaks decreases as the CNT volume % increases.

3.3. Compressive Strength and Strengthening Mechanisms

Figure 5 presents the compressive stress-strain response of the sintered samples with different CNT vol. %. Table 2 lists the properties of the materials based on the stress-strain curves given in Figure 5. Although a small amount of CNTs (less than 8 vol. %) was added to the matrix, the compressive strength was significantly enhanced. Under the same processing, Al-2 vol. % CNT composite showed a 30 % increase in the compressive strength compared to that of monolithic Al.

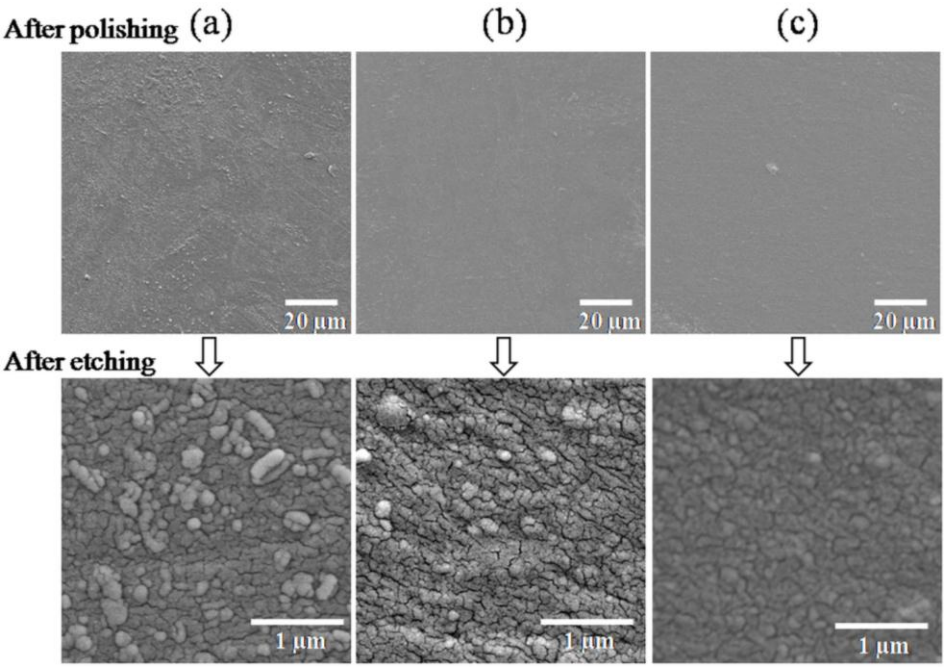

Figure 3. High magnification SEM micrograph of milled Al-2 vol. % CNT powder showing the dispersion of CNTs on flake powders, and (b) XRD patterns of the samples from the (111) planes

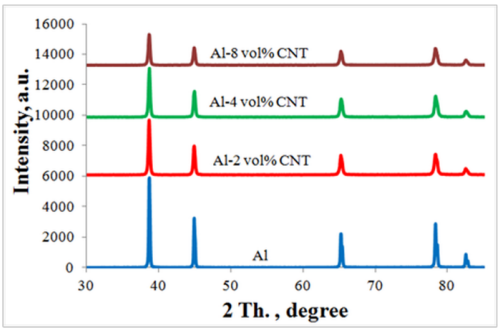

Figure 4. XRD patterns of sintered samples

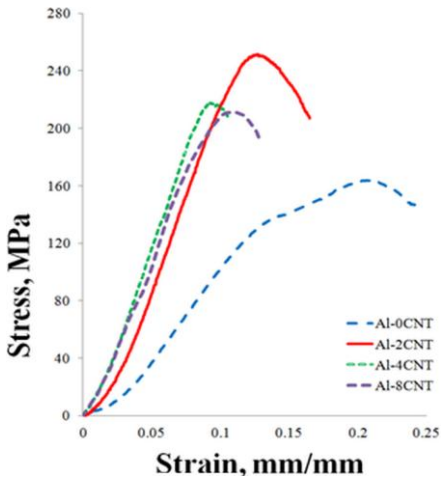

Figure 5. Compressive stress-strain curves of the sintered samples with different CNT vol. %

Table 2. Grain size and strength of the sintered materials

Material	Yield strength (MPa)	Compressive Strength (MPa)	Grain Size (nm)
Al	128.5±8.1	163.8±13.7	220±34
Al-2 vol. % CNT	222.4±14.5	251.3±11.9	163±29
Al-4 vol. % CNT	214.9±11.4	217.6±8.3	161±17
Al-8 vol. % CNT	196.2±16.0	210.9±18.2	156±25

The conventional sintering method resulted in lower strength in samples prepared by flake powders than that of the hot pressed samples [4]. Sintering temperature and time are important factors that determine this difference. hot pressed samples succeeded in obtaining finer structure of the matrix phase due to their lower temperature and shorter soaking time than those of other samples. In addition, the density of the samples plays a role in making this difference. Further, as the compressive strength of the composite increased, its ductility would decrease. Reduced dislocation mobility would lead to decreased ductility.

It should be noted that the CNT content of Al-2 vol. % provided the highest strength. As the CNT content surpassed 2 vol. %, the properties would significantly decrease in comparison to the Al-2 % CNT samples. A decrease in the Al-CNT composite properties at higher CNT contents resulted from the CNT dispersion problems under high reinforcement loads. The results from the Al-CNT samples prepared through different processes [4,21-29] were compared with the optimal results from this study, the summary of which are given in Figure 6. According to the findings, severe plastic

deformations and low temperatures (or short processing times) lead to an improvement in the Al-CNT composite strength mainly due to the refinement of the matrix phase that was altered throughout these processes. In most methods, strength increases at the expense of ductility. On the contrary, those methods that are based on flake powder metallurgy can ensure less ductility reduction.

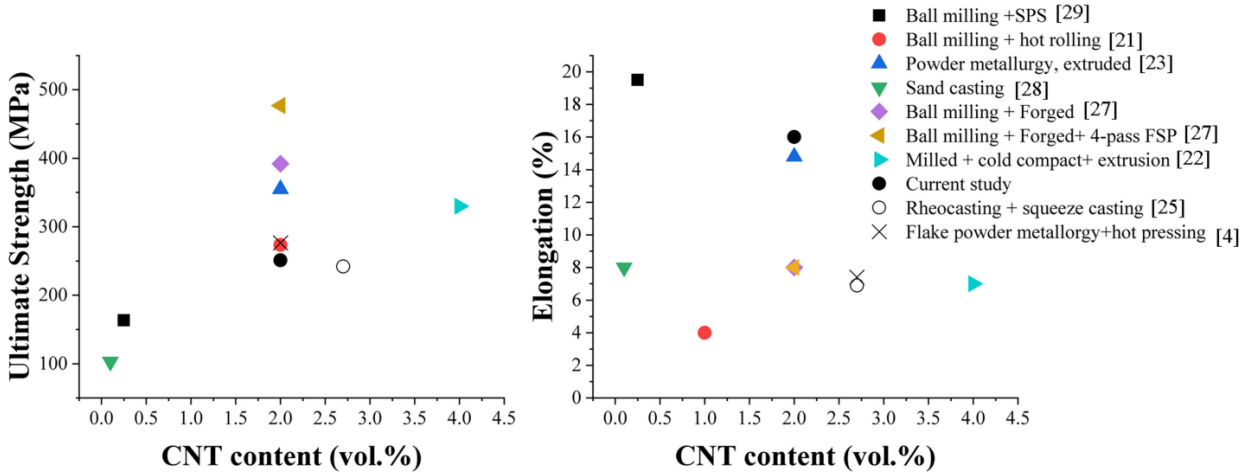

Figure 6. Comparision of strength and ductility of Al-CNT composites prepared by various processes

Two main strengthening mechanisms of load bearing effect and grain size refinement are considered for Al-CNT prepared by the conventional sintering methods. As a result of the high aspect ratio of the CNT, load is transferred from the matrix to the CNTs. According to the Hall-Petch relationship, strength increases as the matrix grain size decreases.

Followed by superimposing two mechanisms contributions, Clyne method calculates yield strength of the composite as follows [30]:

$$\sigma_y = \sigma_0 + \sqrt{{\Delta\sigma_{H-P}}^2 + {\Delta\sigma_{LT}}^2} \quad (1)$$

where σ_0 stands for the intrinsic yield stress (9.8 MPa for Al) [4], $\Delta\sigma_{H-P}$ the grain size effect (Hall-Petch effect), and $\Delta\sigma_{LT}$ the load bearing effect of the CNTs. Based on the equations below, the contribution of each mechanism can be determined. In these equations, some parameters were extracted from the references [4,8].

$$\Delta\sigma_{H-P} = \frac{k}{\sqrt{d}} \quad (2)$$

$$\Delta\sigma_{LT} = V_f\sigma_m \frac{A(l+t)}{4l} \quad (3)$$

where V_f represents the volume fraction of CNTs, and σ_m the yield strength of the unreinforced Al matrix (128.5 MPa). In addition, l and t are the dimensions of the particulate parallel to parallel and perpendicular to the compression direction (l=4 μm and t=60 nm), respectively. The experimental yield strength of Al is used to determine K where A is the aspect ratio of CNTs (66.66) and b the Burgers vector of Al matrix (0.35 nm).

Table 3 presents the results of theoretical calculations of yield stress for the produced nanocomposites. Based on this Table, reducing the grain size or the Hall-Petch mechanism has a greater theoretical contribution than other mechanisms.

Based on the assumptions in theoretical calculations, it can be concluded that the calculated yield stress shows a relatively better fit with the experimental results in the cases of Al and Al-2 vol. % CNT. It is evident that the difference between the theoretical and experimental values is high for CNT content over 2 vol. %.

It should be noted that the probability distribution of the CNTs and relative microstructure heterogeneity are important factors that can better elaborate this difference.

Table 3. Al-CNT composites yield strength and contribution of different strengthening mechanisms

Material	$\Delta\sigma_{H-P}$ (MPa)	$\Delta\sigma_{LT}$ (MPa)	σ_y (MPa)
Al	149.0	-	159.0
Al-2 vol. % CNT	173.3	43.4	226.6
Al-4 vol. % CNT	170.2	86.9	267.0
Al-8 vol. % CNT	177.9	173.8	360.9

4. CONCLUSIONS

1. In this study, Aluminum reinforced with different volume fractions of CNTs was prepared by flake

powder metallurgy through short time milling and conventional sintering methods.
2. The flake powder metallurgy method provided good dispersion of CNTs on the surface of Al particles.
3. The Al- 2 vol. % CNT sintered at 600 °C obtained the highest relative density.
4. The compression test results showed that the CNT volumes less than 2 % led to an increase in the yield and compressive strength values and a higher Young's modulus. However, in higher percentages, the values of these properties would decrease.
5. The contributions of the load bearing and grain size refinement strengthening mechanisms to the final strength of the composites were also investigated, and it was found that the grain size refinement was the dominant strengthening mechanism for Al-CNT composites.

ACKNOWLEDGEMENTS

The author wish to acknowledge University of Maragheh for the all support throughout this work.

REFERENCES

1. Akbarpour, M. R., Alipour, S., Najafi, M., "Tribological characteristics of self-lubricating nanostructured aluminum reinforced with multi-wall CNTs processed by flake powder metallurgy and hot pressing method", ***Diamond and Related Materials***, Vol. 90, (2018), 93–100. https://doi.org/10.1016/j.diamond.2018.10.004
2. Thirugnanasambantham, K. G., Sankaramoorthy, T., Karthikeyan, R., Kumar, K. S., "A comprehensive review: Influence of the concentration of carbon nanotubes (CNT) on mechanical characteristics of aluminium metal matrix composites: Part 1", ***Materials Today: Proceedings***, Vol. 45, (2021), 2561-2566. https://doi.org/10.1016/j.matpr.2020.11.267
3. Thirugnanasambantham, K. G., Sankaramoorthy, T., Reddy, M. K., Aditya, M. P. V. S., "A review: Analysis of load transfer effect in carbon nanotube (CNT) reinforced aluminium (Al) composites", ***Materials Today: Proceedings***, Vol. 60, No. 3, (2022), 1451-1455. https://doi.org/10.1016/j.matpr.2021.11.066
4. Akbarpour, M. R., Pouresmaeil, A., "The influence of CNTs on the microstructure and strength of Al-CNT composites produced by flake powder metallurgy and hot pressing method", ***Diamond and Related Materials***, Vol. 88, (2018), 6-11. https://doi.org/10.1016/j.diamond.2018.06.021
5. Li, A., Xie, M., Yang, Y., Zhang, J., Wang, S., Chen, Y., Zhou, W., "Effect of CNTs content on the mechanical and arc-erosion performance of Ag-CNTs composites", ***Diamond and Related Materials***, Vol. 128, (2022), 109211. https://doi.org/10.1016/j.diamond.2022.109211
6. Akbarpour, M. R., Salahi, E., "Microstructural Characterization and Consolidation of Severely Deformed Copper Powder Reinforced with Multiwalled Carbon Nanotubes", ***Acta Physica Polonica, A.***, Vol. 127, No. 6, (2015), 1722-1726. https://doi.org/10.12693/APhysPolA.127.1722
7. Akbarpour, M. R., Alipour, S., "Microstructure and tribological properties of nanostructured aluminum reinforced with SiC nanoparticles fabricated by powder metallurgy route", ***Transactions of the Indian Institute of Metals***, Vol. 71, No. 3, (2018), 745-752. https://doi.org/10.1007/s12666-017-1207-6
8. Akbarpour, M. R., "Analysis of load transfer mechanism in Cu reinforced with carbon nanotubes fabricated by powder metallurgy route", ***Journal of Materials Engineering and Performance***, Vol. 25, No. 5, (2016), 1749-1756. https://doi.org/10.1007/s11665-016-2042-3
9. Liao, J., Tan, M. J., "A simple approach to prepare Al/CNT composite: Spread–Dispersion (SD) method", ***Materials Letters***, Vol. 65, No. 17-18, (2011), 2742-2744. https://doi.org/10.1016/j.matlet.2011.05.067
10. Fan, G., Xu, R., Tan, Z., Zhang, D., Li, Z., "Development of flake powder metallurgy in fabricating metal matrix composites: a review", ***Acta Metallurgica Sinica (English Letters)***, Vol. 27, No. 5, (2014), 806-815. https://doi.org/10.1007/s40195-014-0148-x
11. Jiang, L., Li, Z., Fan, G., Zhang, D., "A flake powder metallurgy approach to Al_2O_3/Al biomimetic nanolaminated composites with enhanced ductility", ***Scripta Materialia***, Vol. 65, No. 5, (2011), 412-415. https://doi.org/10.1016/j.scriptamat.2011.05.022
12. Liu, L., Li, S., Zhang, X., Pan, D., Gao, L., Chen, B., Umeda, J., Kondoh, K., "Syntheses, microstructure evolution and performance of strength-ductility matched aluminum matrix composites reinforced by nano SiC-cladded CNTs", ***Materials Science and Engineering: A***, Vol. 824, (2021), 141784. https://doi.org/10.1016/j.msea.2021.141784
13. Wan, J., Chen, B., Feng, D., Cao, L., Shen, J., Guo, B., Li, J. S., "Strengthening efficiency competition between carbon nanotubes (CNTs) and in-situ Al_4C_3 nanorods in CNTs/Al composites influenced by alumina characteristics", ***Composites Part A: Applied Science and Manufacturing***, Vol. 152, (2022), 106704. https://doi.org/10.1016/j.compositesa.2021.106704
14. Xu, R., Tan, Z., Xiong, D., Fan, G., Guo, Q., Zhang, J., Su, Y., Li, Z., Zhang, D., "Balanced strength and ductility in CNT/Al composites achieved by flake powder metallurgy via shift-speed ball milling", ***Composites Part A: Applied Science and Manufacturing***, Vol. 96, (2017), 57-66. https://doi.org/10.1016/j.compositesa.2017.02.017
15. Jiang, L., Li, Z., Fan, G., Cao, L., Zhang, D., "Strong and ductile carbon nanotube/aluminum bulk nanolaminated composites with two-dimensional alignment of carbon nanotubes", ***Scripta Materialia***, Vol. 66, No. 6, (2012), 331-334. https://doi.org/10.1016/j.scriptamat.2011.11.023
16. Jiang, L., Li, Z., Fan, G., Cao, L., Zhang, D., "The use of flake powder metallurgy to produce carbon nanotube (CNT)/aluminum composites with a homogenous CNT distribution", ***Carbon***, Vol. 50, No. 5, (2012), 1993-1998. https://doi.org/10.1016/j.carbon.2011.12.057
17. Özer, E., Ayvaz, M., Übeyli, M., Sarpkaya, İ., "Properties of Aluminum Nano Composites Bearing Alumina Particles and Multiwall Carbon Nanotubes Manufactured by Mechanical Alloying and Microwave Sintering", ***Metals and Materials International***, (2022), 1-18. https://doi.org/10.1007/s12540-022-01238-0
18. Akbarpour Arbatan, M. R., Torknik, F. S., "Modelling and Optimization of Densification and Hardness of Cu/SiC Nanocomposites based on Response Surface Methodology (RSM)", ***Advanced Ceramics Progress***, Vol. 7, No. 4, (2021), 28-35. https://doi.org/10.30501/acp.2022.325167.1080
19. Akbarpour Arbatan, M. R., Leisi Azar, F., Alipour, S., "Fabrication of nanostructured cu matrix nanocomposites by high energy mechanical milling and spark plasma sintering", ***Advanced Ceramics Progress***, Vol. 1, No. 3, (2015), 39-43. https://doi.org/10.30501/acp.2015.70011
20. Suárez, S., Ramos-Moore, E., Lechthaler, B., Mücklich, F., "Grain growth analysis of multiwalled carbon nanotube-reinforced bulk Ni composites", ***Carbon***, Vol. 70, (2014), 173-178. https://doi.org/10.1016/j.carbon.2013.12.089
21. Shi, Y., Zhao, L., Li, Z., Li, Z., Xiong, D. B., Su, Y., Osovski, S., Guo, Q., "Strengthening and deformation mechanisms in

nanolaminated single-walled carbon nanotube-aluminum composites", ***Materials Science and Engineering: A***, Vol. 764, (2019), 138273. https://doi.org/10.1016/j.msea.2019.138273

22. Hassan, M. T., Esawi, A. M., Metwalli, S., "Effect of carbon nanotube damage on the mechanical properties of aluminium–carbon nanotube composites", ***Journal of Alloys and Compounds***, Vol. 607, (2014), 215-222. https://doi.org/10.1016/j.jallcom.2014.03.174
23. Bastwros, M. M., Esawi, A. M., Wifi, A., "Friction and wear behavior of Al–CNT composites", ***Wear***, Vol. 307, No. 1-2, (2013), 164-173. https://doi.org/10.1016/j.wear.2013.08.021
24. Xu, R., Tan, Z., Fan, G., Ji, G., Li, Z., Guo, Q., Li, Z., Zhang, D., "Microstructure-based modeling on structure-mechanical property relationships in carbon nanotube/aluminum composites", ***International Journal of Plasticity***, Vol. 120, (2019), 278-295. https://doi.org/10.1016/j.ijplas.2019.05.006
25. Elshalakany, A. B., Osman, T. A., Khattab, A., Azzam, B., Zaki, M., "Microstructure and mechanical properties of MWCNTs reinforced A356 aluminum alloys cast nanocomposites fabricated by using a combination of rheocasting and squeeze casting techniques", ***Journal of Nanomaterials***, Vol. 2014, (2014), 386370. https://doi.org/10.1155/2014/386370
26. Chen, B., Shen, J., Ye, X., Imai, H., Umeda, J., Takahashi, M., Kondoh, K., "Solid-state interfacial reaction and load transfer efficiency in carbon nanotubes (CNTs)-reinforced aluminum matrix composites", ***Carbon***, Vol. 114, (2017), 198-208. https://doi.org/10.1016/j.carbon.2016.12.013
27. Liu, Z. Y., Xiao, B. L., Wang, W. G., Ma, Z. Y., "Singly dispersed carbon nanotube/aluminum composites fabricated by powder metallurgy combined with friction stir processing", ***Carbon***, Vol. 50, No. 5, (2012) 1843-1852. https://doi.org/10.1016/j.carbon.2011.12.034
28. Alekseev, A. V., Dubov, D. Y., Predtechenskiy, M. R., "Influence of carbon nanotubes on mechanical properties of cast aluminum, Grade A5", ***Inorganic Materials: Applied Research***, Vol. 9, No. 2, (2018), 270-278. https://doi.org/10.1134/S2075113318020028
29. Zhang, X., Li, S., Pan, B., Pan, D., Liu, L., Hou, X., Chu, M., Kondoh, K., Zhao, M., "Regulation of interface between carbon nanotubes-aluminum and its strengthening effect in CNTs reinforced aluminum matrix nanocomposites", ***Carbon***, Vol. 155, (2019), 686-696. https://doi.org/10.1016/j.carbon.2019.09.016
30. Clyne, T. W., Hull, D., ***An Introduction to Composite Materials***, 3rd Ed., Cambridge, Cambridge university press, (2019). https://doi.org/10.1017/9781139050586

Advanced Ceramics Progress: Vol. 8, No. 2, (Spring 2022) 34-52

Materials and Energy Research Center
MERC

Contents lists available at ACERP

Advanced Ceramics Progress

Journal Homepage: www.acerp.ir

Original Research Article

Mechanical Strength, Durability, and Environmental Properties of Ternary Blended Self-Compacting Cementitious Mortar Containing Class F Fly Ash and Waste Ceramic Powder

Babak Behforouz [a, *], Behnam Zehtab [b], Shahin Rajaei [c], Misagh Karimzadeh [d], Farshad Ameri [e]

[a] *Assistant Professor, Department of Civil Engineering, Dehaghan Branch, Islamic Azad University, Dehaghan, Isfahan, Iran*
[b] *Adjunct Professor, Department of Civil Engineering, Isfahan (Khorasgan) Branch, Islamic Azad University, Isfahan, Isfahan, Iran*
[c] *Research Assistant, Department of Civil Engineering, Ardestan Branch, Islamic Azad University, Ardestan, Isfahan, Iran*
[d] *Research Assistant, International Institute of Earthquake Engineering and Seismology, Tehran, Tehran, Iran*
[e] *PhD Student, School of Housing, Building and Planning, Universiti Sains Malaysia, 11800 USM Penang, Malaysia*

* Corresponding Author Email: babak_behforooz@pci.iaun.ac.ir (B. Behforouz)

URL: https://www.acerp.ir/article_154885.html

ARTICLE INFO

Article History:

Received 7 May 2022
Received in revised form 8 August 2022
Accepted 16 August 2022

Keywords:

Self-Compacting Mortar (SCM)
Waste Ceramic Powder (WCP)
Fly Ash (FA)
Mechanical Properties
Durability
Environmental Impact

ABSTRACT

In this paper, the mechanical as well as workability and durability properties of Self-Compacting Mortars (SCMs) made of different contents of Waste Ceramic Powder (WCP) and class F Fly Ash (FA) were experimentally assessed. To this end, the fresh properties of the SCM mixtures were evaluated through detailed examination of both mini slump flow and mini V-funnel tests. Ternary SCM mixtures are characterized by more flowability and passing ability than the control mix. The compressive and flexural strength, water absorption, and electrical resistivity tests were also carried out at different curing ages. The obtained results revealed that the compressive and flexural strength of the ternary SCM samples were lower than those of the control mix, especially at the ages of 7 and 28 days. However, there was a strength gain between 28 and 90 days due to the pozzolanic reactivity of both FA and WCP. Water absorption of the ternary SCM specimens containing FA and WCP followed a decreasing trend, thus highlighting the filling effect of the used pozzolans. Ternary SCM samples had considerably higher electrical resistivity (up to 144 % at 90 days) than the binary blends and control mix. Scanning Electron Microscopy (SEM) images confirmed that application of FA and WCP would fill in the pores and micro-cracks. Based on the obtained results, it can be concluded that both FA and WCP act more as a filler rather than a reactive pozzolanic material. Finally, the environmental analysis results revealed that replacement of 50 % of the Portland cement with 30 % FA and 20 % WCP would result in a reduction in the carbon footprint and energy demand by 47 % and 29 %, respectively.

https://doi.org/10.30501/acp.2022.341316.1089

1. INTRODUCTION

One of the most important concerns in sustainable development of construction industry is to build structures with the lowest possible energy consumption and air pollution [1]. Portland cement plants emit about one ton of carbon dioxide released into the air for every ton of cement powder production [2]. However, concrete

Please cite this article as: Behforouz, B., Zehtab B., Rajaei, S., Karimzadeh, M., Ameri, F., "Mechanical Strength, Durability, and Environmental Properties of Ternary Blended Self-Compacting Cementitious Mortar Containing Class F Fly Ash and Waste Ceramic Powder", ***Advanced Ceramics Progress***, Vol. 8, No. 2, (2022), 34-52. https://doi.org/10.30501/acp.2022.341316.1089

is the most consumed man-made material all around the world, and its production is inevitable. To solve this problem, efforts have been made to reduce cement consumption by replacing cement with other supplementary materials. Cement consumption could also be reduced by extending the lifetime of structures. Any weakness in the durability properties used in constructions proved to be a more important reason for failure of the concrete structures rather than the strength loss. Using the waste materials in cementitious mixtures as the supplementary materials enjoys two main benefits: (1) efficient reuse of the agricultural, mining, and industrial by-products or even unusable waste materials in cementitious mixtures significantly contributes to having a cleaner environment [3,4], and (2) partial replacement of cement by supplementary materials will improve the mechanical and durability properties of cementitious mixtures [5-11] and reduce the cement consumption through prolonging the structure service life [12].

The main focus in this study is put on the waste materials called Fly Ash (FA) [13-16] and Waste Ceramic Powder (WCP) [17-20]. Characterized by pozzolanic properties, these materials can be utilized as the supplementary materials. A large amount of waste ceramic tiles is annually discarded in the environment. Grinding the ceramic tiles facilitates use of waste ceramic in the cementitious mixtures so that different sizes of waste ceramic can be transformed into pozzolanic powder as well as fine or coarse aggregates [21-23]. WCP mainly plays the filler role in concrete mixtures. Utilizing the fine particles of WCP as the fine aggregates or fillers make the mixtures more flowable [24], less permeable, and more durable than its regular counterparts, when exposed to chloride ion penetration [25]. In addition to the mentioned role of the WCP, its incorporation into the concrete mixtures can affect the long-term compressive strength of the samples [9]. Moreover, Differential Scanning Calorimetry (DSC) and thermogravimetric analyses confirmed the gradual consumption of calcium hydroxide over time [26]. Based on these two facts as well as the XRD analysis results [20], it can be concluded that when used in cementitious mixtures, WCP had pozzolanic activities. The positive effects of the WCP introduction on the durability as well as mechanical properties of cementitious mixtures can be multiplied by preparing a ternary cementitious mixture by adding a highly-active pozzolan such as FA and nano-SiO_2 [20]. FA is one of the most used materials in cementitious mixtures as a supplementary material in the world [13-16]. It is a by-product produced in coal-fired power plants. Huge tons of FA are annually produced in the world, a majority of which are released into the environment. There are two types of FA that are used in concrete: class C FA and class F FA. Class F FA is pozzolanic while class C FA is both self-cementing and pozzolanic [27]. The main difference between the class F and class C FA is related to their chemical composition. According to the ASTM C-618 [28], both class F and C FA must contain the total amount of aluminum, silicon, and iron oxides higher than 70 % and 50 % wt., respectively. Class F FA is a low-calcium FA containing less than 10 % and 1.5 % CaO and Na_2O, respectively. Class F FA has lower density and higher fineness than those of its class C fly counterpart [27]. The introduced FA powders into the concrete must satisfy the fineness requirements to ensure that the retained materials on the 0.045-mm sieve are lower than 40 % [29]. Of note, non-conforming FA has also several reasonable properties [30]. Self-Compacting Concrete (SCC) samples containing class F FA are characterized by higher compressive strength and lower shrinkage [15,31] than those of their counterparts. However, their compressive strength might not significantly increase, compared to that of the ordinary SCC samples. According to the observations, the value of the mentioned criterion decreased in the mixtures containing high-volume class C FA [32]. Incorporation of finer particles of FA into the self-compacting mixtures would slightly lessen their strength while making them more flowable with better passing ability [33]. In addition, introduction of class F FA into the self-compacting mixtures would significantly increase the electrical resistivity and improve the volume stability of the samples [34]. Incorporation of the FA into the SCC would decrease the total charge passing through the samples, hence higher resistance of the produced samples to the penetration of chloride ions than that of the control samples. In addition, the produced samples had lower weight loss when exposed to acid attack [35]. Higher or similar porosity in Interfacial Transition Zone (ITZ) and significantly better durability of the SCC samples with FA than those of the control samples strongly proved the greater impact of the binder type in the cementitious mixtures than that of porosity on the durability of SCC mixtures in the case of deteriorations caused by penetration of harmful ions and liquids [36].

Numerous research studies have investigated the durability and mechanical properties of binary Self-Compacting Mortars (SCMs) made of either WCP or FA. However, to the best of the authors' knowledge, no research was found in the literature on the properties of ternary blended cementitious mixtures using WCP and FA in the Portland cement. In this regard, the current study selected the FA as a supplementary material to improve the durability and mechanical properties of the self-compacting mixture containing WCP. Then, it evaluated the flowability and passing ability of the SCM mixture using mini slump flow and mini V-funnel tests. In the current research, the compressive and flexural strength, water absorption, and electrical resistivity of the SCC samples were investigated at the age of 7, 28, and 90 days. In addition, the microstructural structure of the hardened samples was evaluated using Scanning Electron

Microscopy (SEM) images. Finally, an environmental assessment was carried out to study the effects of different FA and WCP contents on the carbon dioxide emission and energy consumption of the SCM mixes.

2. EXPERIMENTAL

2.1. Materials

In this paper, the SCM mixtures were prepared using Portland cement, FA, WCP, water, sand, and Super-Plasticizer (SP). The Portland cement used in the mixtures was Type-II cement produced by Sepahan cement Co. Esfahan, Iran, which meets the requirements of ASTM C-150 [37]. Class-F FA was used for constructing the mixture with enough fineness in accordance with the instructions of UNE-EN 933-10 [38]. FA can be appropriately used for blending the pozzolanic cementitious mixtures on condition that the amount of FA powder is about 33 % on the 45 µm sieve. WCP was prepared through some physical processing on the waste ceramic tiles of RAK ceramic company in Isfahan, Iran. Waste ceramic tiles were ground using air jet mill and then, they were passed through a 75 µm (#200) sieve. The materials passing through the 75 µm sieve were used for preparing the paste. Table 1 lists the chemical composition as well as the physical properties of the cement, WCP, and FA.

TABLE 1. Physical and chemical properties of the binders used in this study

	Chemical compound	OPC	WCP	FA
Chemical Composition	SiO_2	21.5	63.29	70.70
	Al_2O_3	6.0	18.29	20.70
	Fe_2O_3	2.5	4.32	3.90
	CaO	66	4.46	1.13
	MgO	2.0	0.72	0.77
	SO_3	0.3	0.10	0.44
	Total Alkali (Na_2O+0.658 K_2O)	0.75	2.18	0.98
	LOI	1.00	1.61	0.70
Physical Properties	Specific Gravity (g/cm^3)	3.18	2.36	2.20
	Specific Surface Area (cm^2/g)	3500	3250	2850

The pozzolanic properties can be attributed to the cementitious raw materials when the total amounts of SiO_2, Fe_2O_3, and Al_2O_3 are higher than 70 %, the volume of SO_3 oxides is lower than 5 %, and their Loss of Ignition (LOI) is lower than 6 % [28]. As observed in Table 1, the total amounts of the WCP and FA are about 85.9 % and 95.3 %, respectively, and their corresponding SO_3 volume and LOI are sufficiently low. Therefore, it can be concluded that both WCP and FA exhibit pozzolanic behavior in a sense that they might contribute in the hydration process along with delay.

Natural river sand was used as fine aggregate. The values of the density, water absorption, and fineness modulus of the used sand were 2460 kg/m^3, 1.8 %, and 3.2, respectively. The specification of the implemented sand meets the ASTM C-778 requirements [39]. Mixing water was supplied from purified drinking municipal water. In order to reduce the required water consumption and make the mixture more flowable, the polycarboxylic-ether-based Superplasticizer (SP) was utilized. The chosen SP type was High-Range Water Reducer (HRWR) with the density of 1.07 g/cm^3 (at 20 °C) and pH of 7.5 ± 1.

2.2. Mix Design and Sample Preparation

This study aims to evaluate the performance of ternary SCM mixes produced from different percentages of FA, WCP, and Portland cement. The primary binder was Portland cement which was then partially substituted by different amounts of FA and WCP. The total replacement ratio of cement with the aforementioned materials was considered to be 50 % to maintain adequate strength development. The replacement ratios of the FA with Portland cement were 10, 20, and 30 %, and those for the WCP were 5, 10, 15, and 20 % (by weight). The WCP and FA were incorporated at the previously mentioned dosages alone and combined with each other to evaluate their sole and combined effects on the properties of the mixtures.

Some preliminary tests were also done to find out the precise amounts of the required contributing materials in the SCM mixtures to obtain a reasonable range of outputs. Different w/c ratios and amounts of the raw materials were examined to obtain the material proportions for different mixes that are listed in Table 2. This table also shows the required weight of materials (kg) used for making one cubic meter of SCM mixtures. In the mix ID letters, W and F stands for WCP and FA, respectively. The total mass of one cubic meter of the blended SCM mixtures for all of the mix IDs was assumed to be 2106 kg. Further, the ratio of water to cementitious materials (w/c) was assumed to be 0.48 for all SCM mixes.

Aggregates and cementitious powders containing cement, FA, and WCP were initially mixed in a dry state. Then, SP and water were mixed to produce a homogenous solution, and the resultant solution was added to the mixture. The mixture was blended until a uniform mortar was created. When the SCM was ready, the fresh properties of the mixture were examined using mini slump flow and mini V-funnel tests according to EFNARC guidelines [40]. The mixture with a larger slump flow diameter is more capable of overcoming friction and the consequent deformation under its weight [6].

The diameter of the fresh mixture must be measured when it was spread on the test plate after removing the standard slump cone.

TABLE 2. Mixture proportions of blended mortars (kg/m^3)

Sample ID	Cement	FA	WCP	Water	Sand	SP
Control	550	-	-	264	1286	6.6
FA10	495	55	-	264	1286	6.6
FA20	440	110	-	264	1286	6.6
FA30	385	165	-	264	1286	6.6
WC5	522.5	-	27.5	264	1286	6.6
WC10	495	-	55	264	1286	6.6
WC15	467.5	-	82.5	264	1286	6.6
WC20	440	-	110	264	1286	6.6
FA10WC5	467.5	55	27.5	264	1286	6.6
FA20WC5	412.5	110	27.5	264	1286	6.6
FA30WC5	357.5	165	27.5	264	1286	6.6
FA10WC10	440	55	55	264	1286	6.6
FA20WC10	385	110	55	264	1286	6.6
FA30WC10	330	165	55	264	1286	6.6
FA10WC15	412.5	55	82.5	264	1286	6.6
FA20WC15	357.5	110	82.5	264	1286	6.6
FA30WC15	302.5	165	82.5	264	1286	6.6
FA10WC20	385	55	110	264	1286	6.6
FA20WC20	330	110	110	264	1286	6.6
FA30WC20	275	165	110	264	1286	6.6

Followed by conducting the tests to evaluate the fresh properties, the whole mixture was blended again before casting. To assess the durability and mechanical properties of different mixes, both prismatic beams and cubic molds are required. Prism mold with dimensions of 40×40×160 mm was used to construct SCM samples and evaluate their flexural strength. The molds with dimensions of 50×50×50 mm were used to cast the cubic samples and assess their compressive strength and water absorption. Followed by 24 hours, the specimens were demolded and cured in the curing room. The specimens were immersed in water at the temperature of 25±3 °C until the desired age was obtained.

2.3. METHODS

2.3.1. Workability

The performance SCM mixes was tested in terms of the workability, mechanical strength, and durability. The mini slump flow and mini V-funnel tests were carried out on the fresh mortar as per EFNARC [40] to evaluate the workability of mixes. In the mini slump flow test, the fresh mix was poured in a cone (100 mm bottom opening, 70 mm top opening, and 60 mm high) and allowed to flow under self-weight once the cone was lifted. The average diameter of the two perpendicular diameters was regarded as the mini slump flow value. The mini V-funnel test measured the filling ability of fresh mix. The test setup has a trap door underneath. The time that took the fresh mortar to flow out of the container was also calculated and reported.

2.3.2. Compressive and Flexural Strengths

The compressive strength of different mixes was examined by exerting universal compression load on the top and bottom faces of cubic specimens at the ages of 3, 7, 28, and 90 days using hydraulic universal testing machine at the loading rate of 0.5 MPa/s, according to the instruction of ASTM C109 [41]. The flexural strength of the SCM prism samples was obtained by measuring the excreted compression loads through one upper loading pin and two lower loading pins using three-point loading setup at the ages of 3, 7, 28, and 90 days, according to the instructions of ASTM C78 [42]. For each individual experiment, three specimens were prepared, and the average value was calculated. Figure 1 demonstrates some of the concrete samples made and tested in terms of their flexural strength.

Figure 1. Some concrete samples were made and tested for flexural strength testing

2.3.3. Water Absorption

In terms of the durability-related properties, the SCM specimens were tested according to ASTM C642 [43] to measure the degree of water absorption. Cubic samples at the ages of 28 and 90 days were placed in the oven at the temperature of 100-110 °C for 24 hours to ensure the complete evaporation of the maintained whole water. Then, the specimens were rested to be cooled at the ambient temperature of the laboratory for one hour.

Afterwards, the SCM cubic sample were saturated in the water at the temperature of 21 °C for 48 hours. The mass of the dried and Saturated Surface-Dried (SSD) specimens were recorded as the oven-dried and SSD mass of the samples, respectively. Water absorption value can be obtained by dividing the SSD mass by the oven-dried mass of the samples in percent. Three samples were tested for each case, and the results were averaged out.

2.3.4. Electrical Resistivity

The electrical resistivity of the cubic samples was measured through ASTM C1760 [44]. Based on the values of the electrical resistivity test, it is possible to estimate the probability of steel rebar corrosion. In case the values of electrical resistivity were higher than the suggested limits allowed by ACI Committee 222 [45], the corrosion rate of the embedded steel reinforcements in concrete would become relatively low.

2.3.5. Environmental Analysis

Mortar mixes were compared from an environmental point of view by computing their Embodied carbon dioxide emitted (ECO_2e) and Embodied Energy (EE). The ECO_2e and EE amounts for one kg of each material were taken from the previous studies [21,46], the results of which are given in Table 3. As mentioned earlier, the environmental analysis was carried out in order to provide better insights into the effect of FA and WCP on the environmental footprint of mortar mixes that is only detected in nature. For a more thorough evaluation, the contribution of other factors such as transportation, maintenance, and material wastage should be taken into account.

TABLE 3. ECO_2e and EE of materials per kg

Materials		ECO_2e ($kgCO_2e$)	EE (MJ)
Binder	OPC	0.93	5.2
	WCP	0.045	1.113
	FA	0.012	0.173
Fine Aggregates	Sand	0.0028	0.081
Water		0.00057	0.2
Admixture	SP	0.6	11.5
Processing		0.0038	0.15

Note: EE = Embodied energy
ECO_2e = Embodied CO_2 emitted

2.3.6. Analysis of Variance (ANOVA)

Analysis of Variance (ANOVA) analysis was also carried out to determine the most significant parameters involved in determining different properties of the SCM mixes [47]. The replacement ratio of FA and WCP, as well as the curing age of mixes were selected as the input variables for the two-way ANOVA.

3. RESULTS AND DISCUSSION

3.1. Workability

The flowability of mortars was evaluated based on mini slump flow and mini V-funnel tests. As illustrated in Figure 2(a), an increase in the WCP content in the fresh mortar would make it less viscous than the ordinary Portland cement mortar. The mixture containing 20 % WCP had the highest slump flow diameter among the others with constant FA amounts, which was about 5.5 % higher than that of the control mix. Clearly, incorporation of FA into the cementitious mortar would lead to increased flowability. Similar to the effect of WCP on the flow value of mixes, increasing the FA content enhanced the workability of the fresh mortar up to approximately 5 % at the FA replacement ratio of 30 %. Such enhancement can be attributed to the spherical shape of FA and WCP particles, which reduced the internal friction between the paste and aggregate and consequently increased the flow value. In addition, use of the WCP and FA combination resulted in the highest improvement in the slump flow value, where incorporation of 30 % FA and 20 % WCP increased the slump flow up to about 8.4 % in the control mix. Jalal et al. [15] reported that an increase in the FA content made the SCM less resistant to flow. They also showed that replacement of 15 % cement with the FA led to an increase up to about 7.7 % and 10 % in the slump flow diameter for binder content of 400 and 500 kg/m^3, respectively. In contrast with the results from the present research, Heidari and Tavakoli [48] observed that fresh concrete mixtures containing WCP had a slump diameter smaller than the corresponding diameter value in the control mixture. The contradiction in the results of the aforementioned research and those of the current one may be due to either the interaction between the use of different SP and WCP or the tiles grinding method. While this study employed the slump flow test was, that of Heidari and Tavakoli's used the conventional slump test.

As shown in Figure 2(b), the same conclusions can be drawn as those presented in Figure 2(a). According to Figure 2(b), the flow time decreased upon increasing the WCP content until it reasched 15 % wt. The minimum time was recorded for SCM mix containing 15 % WCP. It took a little bit more time for the mix containing 20 % WCP to pass through the V-funnel than for the SCMs with 15 % WCP. As observed in Figure 2(b), the flowability of the SCM mixture increased upon increasing the FA content. However, their flow time values decreased when more FA powder was introduced into the mixture. The observed reduction in the measured V-funnel flow time values had no conflict with the estimated trend observed in the literature for the variation of corresponding values for different FA contents [34,35,49]. Jalal et al. [15] showed that the mixture containing 15 % of FA could pass through the V-funnel about three seconds faster than the control mixture.

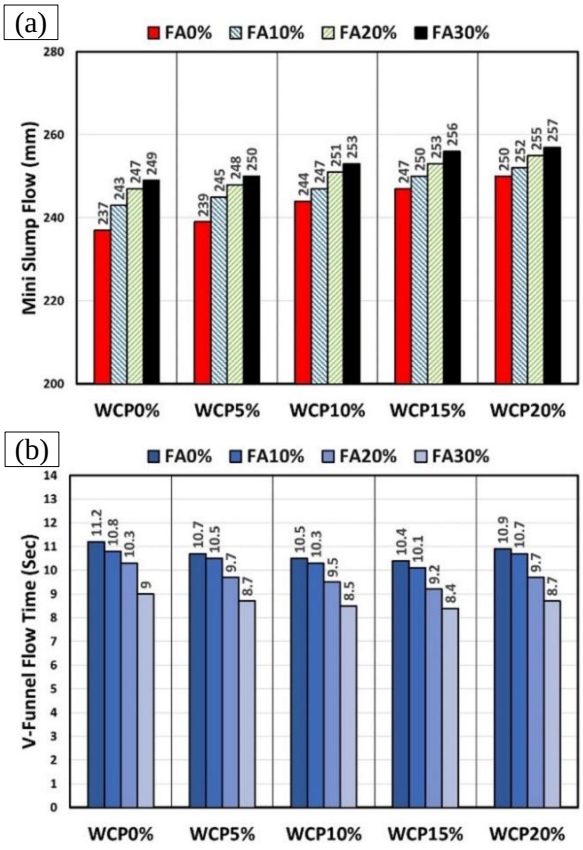

Figure 2. Effect of WCP and FA on (a) mini slump flow and (b) V-funnel flow time

3.2. Mechanical Properties

3.2.1. Compressive Strength

The SCM samples were subjected to compressive loading based on a universal test setup to evaluate their compressive strength at the ages of 3, 7, 28, and 90 days. Figure 3 presents the average values of the compressive strength of the SCM samples at different ages. Evaluation of the ratio of 28-day compressive strength to 90-day compressive strength (Maturing ratio, M) of the samples revealed that the compressive strength of the samples was notably enhanced at the age of 90 days, especially for the samples with low percentages of WCP and FA. Both control and FA30WC20 samples with the M ratio of 92 % and 65 % are characterized by the lowest and highest pozzolanic properties.

According to Figure 3, incorporation of both FA and WCP into the SCM mixtures caused a significant decrease in the compressive strength compared to the control sample at all curing ages. The reduction in the compressive strength might result from the relatively weaker cementitious properties of WCP and FA than those of the Portland cement [49,50]. Mixes containing FA as a partial replacement of OPC showed about 2 %, 21 %, and 31 %, lower 28-day compressive strength than those of the control mix at the FA replacement ratios of 10 %, 20 %, and 30 %, respectively. Utilization of WCP had the same effect on the compressive strength of mixes.

The 28-day compressive strength of mixes incorporating 5 %, 10 %, 15 %, and 20 % WCP was reduced by about 9 %, 16 %, 20 %, 28 % respectively, compared to the control mix. The combined use of FA and WCP further reduced the strength, and the reduction rates became greater upon increasing the FA and WCP contents. For example, blending 5 %, 10 %, 15 %, and 20 % WCP with 30 % FA reduced the 28-day compressive strength by approximately 34 %, 38 %, 45 %, and 49 %, respectively, compared to the control mix. The strength development of the mixes mainly depends on the physical characteristics, reactivity of the binder, and quality of ITZ, i.e., the critical factors for providing adequate physical anchorage and gel formation. FA particles with round edges are more spherical than the OPC, which can reduce the internal friction in the ITZ and lower the load-carrying capacity of mixes. On the contrary, FA has lower pozzolanic reactivity than the OPC which in turn decreases the amount of hydration products, thus reducing the mechanical strength [15,51]. Similarly, WCP particles are not as reactive as the OPC particles, and replacing OPC with the WCP negatively affects the formation of C-S-H gel which in turn makes the microstructure less compact [17,20]. In addition, the XRD results confirmed the presence of higher amount of alumina in the WCP and FA, compared to the OPC, which was already reported as one of the factors with a negative impact on the strength of the cement-based materials [52].

As further observed, incorporation of both FA and WCP had a detrimental effect on the strength development process. In the control mix, the compressive strength after 3, 7, and 90 days of curing was about 55 %, 87 %, and 108 % of the 28-day compressive strength, respectively. However, use of WCP and FA delayed the formation of hydration of products. The lowest strength gains at the ages of 3 and 7 days was recorded for FA30WC10 and FA30WC20 mixes, which was 39 % and 66 % of the corresponding value for the 28-day compressive strength, respectively. Moreover, the negative effects of both FA and WCP were more noticeable at the earlier ages, which could be attributed to their harmful effect on the hydration process. For instance, FA30WC20 mix had about 52 %, 61 %, 49 %, and 27 % lower compressive strength at the age of 3, 7, 28, and 90 days, respectively, than the control mix. As observed, the percentage reduction was higher at the earlier ages; however, with an increase in the curing age, it was considerably controlled. The immature pozzolanic reaction was completed at the later ages, which led to densification of the pore system. According to the results, the ratio of the 90-day to 28-day compressive strength was significantly higher in mixes containing both FA and WCP. As a case in point, the ratio for the FA30WC20 mix was 1.54, while the corresponding value for the control mix was 1.08.

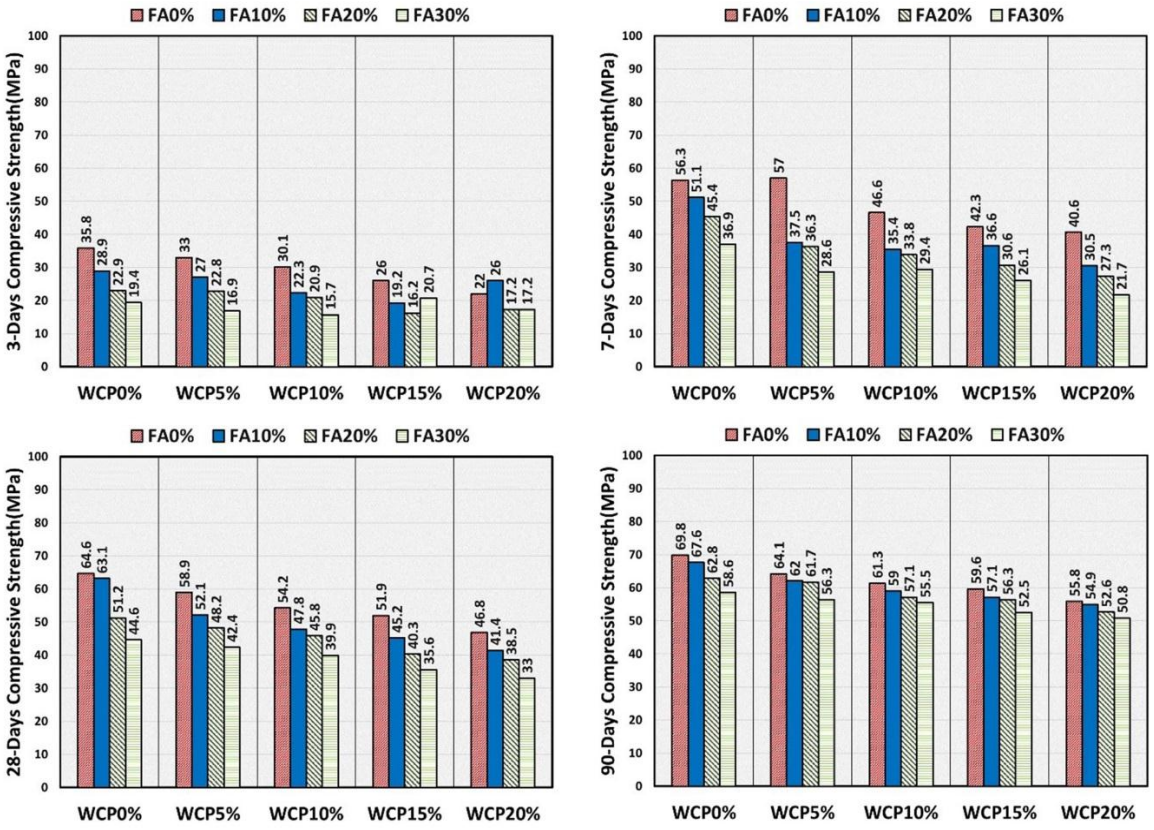

Figure 3. Compressive strength of SCM mixes at 3, 7, 28, and 90 days

The ratio was considerably lower in mixes made solely with either FA or WCP (1.31 in the FA30 mix and 1.19 in the WC20 mix), thus highlighting the remarkable impact of the combined use of these materials on the strength gain. It also indicated that the pozzolanic reaction of the supplementary materials added to the mixes proceeded at a faster rate after 28 days and that many unreacted particles participated in chemical reactions. In fact, the $Ca(OH)_2$ produced as a result of hydration of OPC was consumed by the high silica content available in the WCP and FA [20]. It produced additional gel, thereby contributing to the strength gain at later ages [17]. This conclusion was completely in agreement with the observations of previous researchers in the literature [9,17,20].

3.2.2. Flexural Strength

The flexural strength of the three identical beam specimens was determined for each mix through three-point loading flexural test, the average of which for different curing ages is presented in Figure 4. The obtained results supported those of the compressive strength, and similar trends were obseved for the flexural strength of mixes incorporating different percentages of FA and WCP. As shown in this figure, there was a reduction in the flexural strength at all curing ages with the inclusion of alternative pozzolanic materials. However, the reduction rates were much lower than the compressive strength rates, and maximum reduction was about 16 % in FA20WC20 mix after three days of curing. Use of FA or WCP alone did not have any significant impact on the flexural strength of the mixes. For instance, incorporating up to 30 % FA reduced the 28-day flexural strength by about 9 %, compared the control mix. The reduction ratio in the flexural strength of the binary mixtures contain different amounts of WCP in the range of 5-20 % were 0.9 to 9.7 %.

As already discovered, the flexural strength of the concrete samples with the WCP ratios of 10, 20, and 30 % was about 92.7, 87.9, and 85.4 % of that of the control samples [53]. The reason behind the inferior flexural performance of the mixes containing FA and WCP to that of the plain mix could be the dilution effect of cement replacement that lowered the amount of hydration products. In addition, the rounder morphology of both FA and WCP than that of OPC was another factor for the lower flexural strength of the mixed containing FA and WCP. As shown in the previous studies, FA was found to be effective in reducing the drying shrinkage of the concrete [34,54].

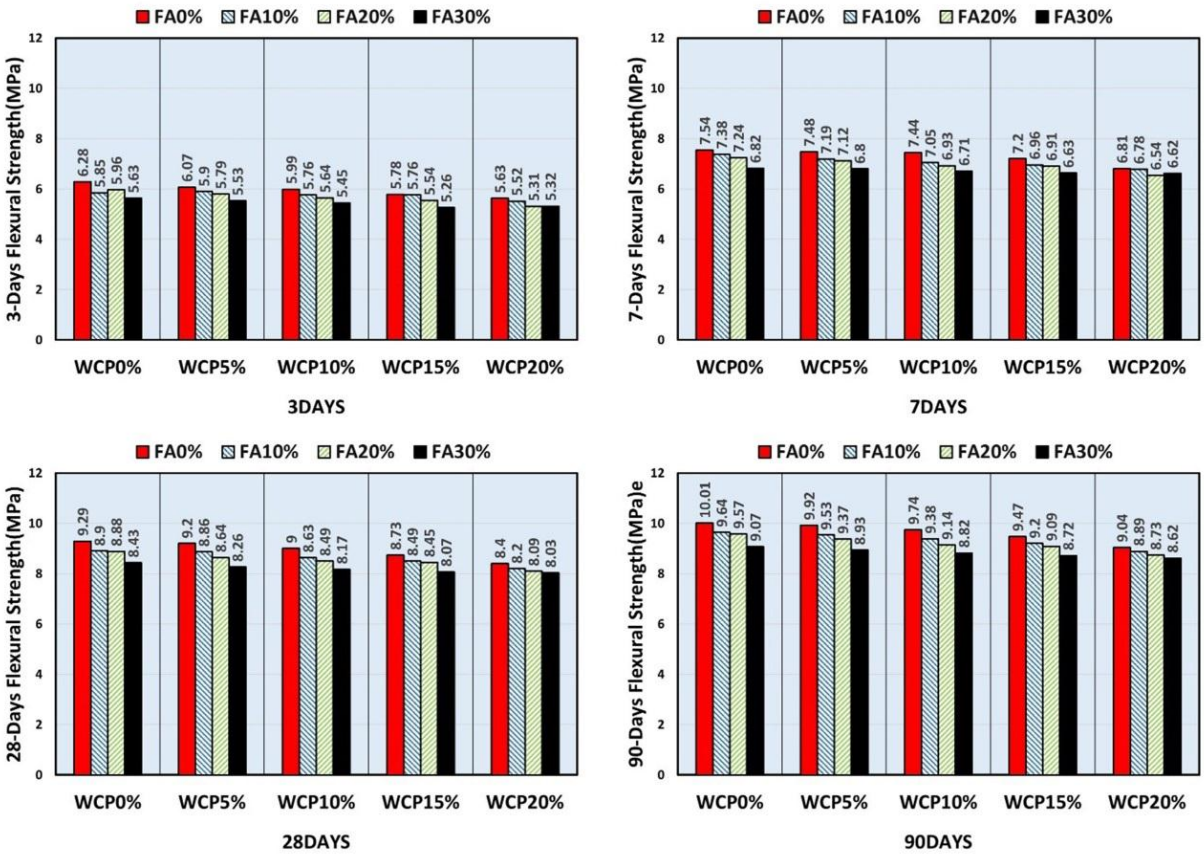

Figure 4. Flexural strength of the SCM mixes at 3, 7, 28, and 90 days

Therefore, it is expected that the number of micro-cracks induced by the drying shrinkage of mortar mixes will decrease while increasing the FA content, thus explaining the lower reduction rates in the flexural strength than those in the compressive strength. The flexural strength obtained by Ferrara et al. [55] in their study showed that the drying shrinkage strain of SCC mixes was reduced using 10 and 30 % WCP as the partial substitution for cement. Similarly, Duran-Herrera et al. [34] reported about 17 % reduction in the drying shrinkage of SCC containing 30 % FA. According to the previous studies, the samples containing FA have a flexural strength of 9.7 % lower than that of the control samples with the replacement ratio of 20 % in the SCM samples [50] and about 7-10 % lower than control concrete samples for replacement ratio of 5-20 % [56].

3.2.3. Linear Regression Analysis and Application of Design Codes for Prediction of Mechanical Strength

In this section, a linear regression model was employed to estimate the flexural strength of the concrete mixtures considering, compressive strength as the input data. Figure 5 shows the experimental data and fitted curve. As observed, the R-factor of regression was 0.88, which is indicative of the accuracy of the proposed model as well as the strong correlation between the compressive and flexural strength values of the mixes.

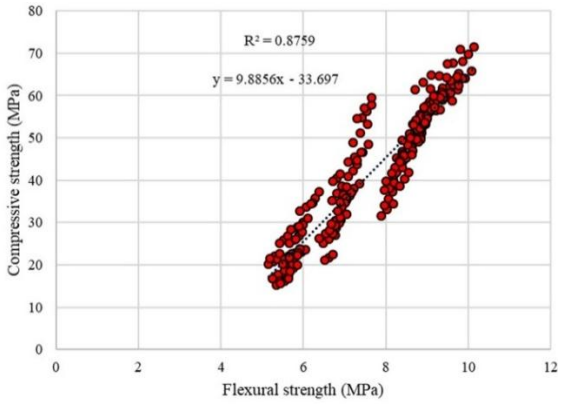

Figure 5. Linear regression model

$$f_c = 9.88f_b - 33.697 \quad (1)$$

The equations proposed by the available design codes were used to estimate the flexural strength of mixes by inserting the considered compressive strength as the

input data. The proposed expressions are presented in Table 4. A comparison was made between the predicted values and those obtained from the flexural strength test. The comparison results were then used to determine the accuracy of the design code relationship in estimating the mechanical properties of SCC incorporating a blend of Portland cement, FA, and WCP.

TABLE 4. Equations proposed by codes

Standard	Flexural strength (f_r) (MPa)
ABA (Iran) [57]	$f_r = 0.60\sqrt{f_c'}$
ACI 318-14 [58]	$f_r = 0.62\sqrt{f_c'}$
CSAA23.3-04 [59]	$f_r = 0.60\sqrt{f_c'}$
EC-04 [60]	$f_r = 0.435 f_c'^{2/3}$
NZS 3101 [61]	$f_r = 0.60\sqrt{f_c'}$

The 28-day flexural strength of the mixes with different percentages of FA and WCP was evaluated based on the 28-day compressive strength.

Table 5 compares the predicted values with the flexural strength values obtained through the experiments. The results indicated that according to the design codes such as ABA, CSAA23.3-04, and NZS 3101, the average ratio of the flexural strength was approximately 0.48 with the standard deviation of 0.024.

In other words, the equations proposed by the previously mentioned design codes should be multiplied by 2.086 to predict the flexural strength of mixes with high accuracy. However, the equations proposed by ACI 318 and EC-04 should be multiplied by 2.019 ($\sigma = 0.025$) and 1.55 ($\sigma = 0.05$), respectively, to estimate the flexural strength of both mixes. Further, the accuracy of the linear regression equation proposed in the present study was reduced when using a combination of FA and WCP. The average ratio of the flexural strength predicted by the linear regression equation to the experimental flexural strength was about 0.96. However, the same ratio for the FA30WC20 mix was measured as 0.84, indicating that the equation underestimated the flexural strength at high replacement rates.

TABLE 5. Comparison test results with the values obtained by the design codes

Code/Mix	Test	Linear regression	ABA	ACI 318	CSAA23.3	EC-04	NZS 3101
Control	9.29	9.95	4.82	4.98	4.82	6.81	4.82
FA10	8.90	9.80	4.77	4.93	4.77	6.71	4.77
FA20	8.88	8.59	4.29	4.43	4.29	5.84	4.29
FA30	8.43	7.92	4.01	4.14	4.01	5.33	4.01
WC5	9.20	9.37	4.61	4.76	4.61	6.41	4.61
WC10	9.00	8.90	4.42	4.57	4.42	6.07	4.42
WC15	8.73	8.66	4.32	4.47	4.32	5.89	4.32
WC20	8.40	8.15	4.10	4.24	4.10	5.51	4.10
FA10WC5	8.86	8.69	4.33	4.48	4.33	5.91	4.33
FA20WC5	8.64	8.29	4.17	4.31	4.17	5.62	4.17
FA30WC5	8.26	7.71	3.91	4.04	3.91	5.16	3.91
FA10WC10	8.63	8.25	4.15	4.29	4.15	5.58	4.15
FA20WC10	8.49	8.05	4.06	4.20	4.06	5.43	4.06
FA30WC10	8.17	7.45	3.79	3.92	3.79	4.96	3.79
FA10WC15	8.49	7.98	4.03	4.17	4.03	5.38	4.03
FA20WC15	8.45	7.49	3.81	3.93	3.81	4.99	3.81
FA30WC15	8.07	7.02	3.58	3.70	3.58	4.60	3.58
FA10WC20	8.20	7.60	3.86	3.99	3.86	5.07	3.86
FA20WC20	8.09	7.30	3.72	3.85	3.72	4.84	3.72
FA30WC20	8.03	6.75	3.45	3.56	3.45	4.37	3.45

3.3. WATER ABSORPTION

Water absorption is a significant criterion for evaluation of the concrete durability and resistance to liquid penetration. Figure 6 presents the average water absorption values of the cube samples after 24 hours of immersion in water at the curing age of 28 and 90 days. Evidently, as observed in this figure, use of FA and WCP as the partial replacement materials of the OPC had a positive impact on the resistance of the SCM mixes to water penetration.

3.4. Electrical Resistivity

The electrical resistivity of the SCM mixes can elaborate the interconnectivity mechanism of the pores and quality of the ITZ. Higher electrical resistivity is indicative of the higher resistance of the material to the aggressive agents and ion transport within the matrix [62]. In this regard, the electrical resistivity of the SCM samples at the ages of 28 and 90 days were obtained through the ACIS method, as shown in Figure 7. According to this figure, the electrical resistivity of the

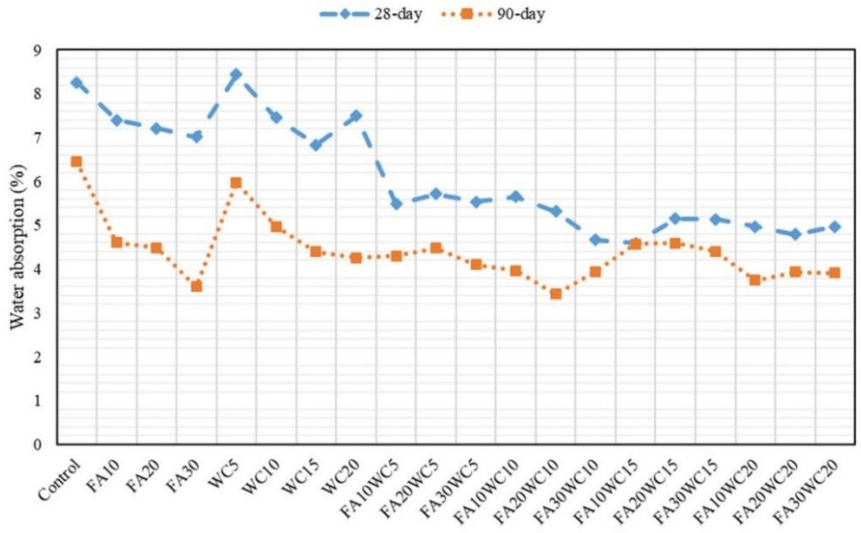

Figure 6. Water absorption of SCM mixes at 28 and 90 days

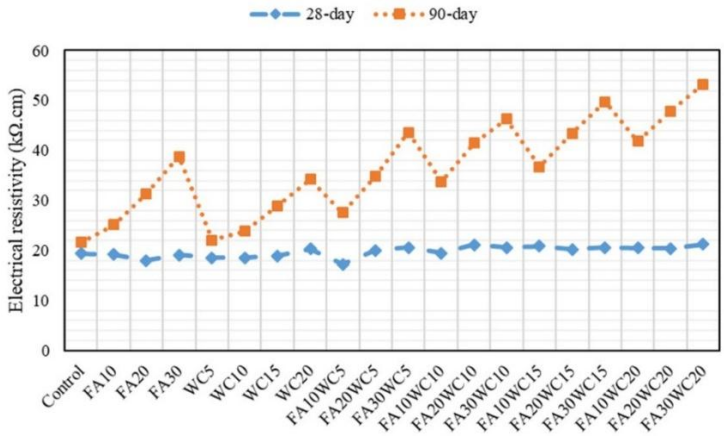

Figure 7. Electrical resistivity of SCM mixes at 28 and 90 days

SCM mixes increased upon increasing the amount of WCP and FA. This finding was in agreement with the already obtained results regarding the water absorption. Such an increase could result from the filling role of the used pozzolans in pore refinement.

In addition, such an increase can be attributed to the products that fill in the pores that are made through delayed reaction of pozzolans with the formed portlandite crystals. To be specific, C-S-H gel which is produced in the available pores densifies the mortar and consequently provides a more compact pore system [24] and lower ionic concentration [63].

The effect of pozzolan addition to the SCM mixes is more visible in the figures at the age of 90 days than at the age of 28 days. This finding is consistent with the results from the compressive strength where there was remarkable enhancement in the 90 day compressive strength, compared to the corresponding value at 28 days.

According to the test results, partial replacement of OPC with FA or WCP did not affect the electrical resistivity at 28 days, and the variations were below 10 %. On the contrary, the SCM mixes enjoyed greater degrees of electrical resistivity at 90 days than those at 28 days, indicating that the major contributions of FA and WCP particles to the chemical reactions begins after 28 days. Jain et al. [49] referred to the non-reactivity of FA at 28 days, which was responsible for the lower mechanical strength of the mix at this age. However, at later ages, the filling effect and formation of ettringite resulting from the pozzolanic reactions facilitated the microstructure densification. Duran-Herrera et al. [34] stated that partial replacement of the OPC with FA would decrease the concentration of Na^+ and K^+ ions in the pore solution which in turn reduced the ion transport, hence higher electrical resistivity.

The highest charges passing through the SCM samples

in the FA30WC20 mix at the age of 28 and 90 days were estimated about 18.59 and 53.27 kΩ.cm for, respectively. In other words, use of 30 % FA in conjunction with 20 % WCP enhanced the electrical resistivity of the mortar by about 146 %, compared to that of the control mix, at 90 days. Kannan et al. [17] found that 40 % cement replacement by the WCP could increase the electrical resistivity up to about 616 % and 765 %, respectively, compared to control samples at the age of 28 and 90 days.

Behforouz et al. [9] also stated that the concrete samples with 50 % WCP content had an electrical resistivity of about 3.7, 3.3, and 4 times higher than that of the control samples at the water-to-binder ratios of 0.3, 0.4, and 0.5, respectively.

Evaluation of the electrical resistivity results provided a tool for assessing the durability of the mixes. A higher electrical resistivity is indicative of a higher density and better durability of the hardened mixture. Fewer pores in the samples make them highly resistant to harmful ions penetration. Many researchers confirmed that cloride ions could penetrate into the inner parts of the concrete elements through the micropores [64,65]. According to the electrical resistivity results, the corrosion potential of the embedded steel rebars in the concrete due to Cl^- ions can be evaluated [66]. It is worth noting that incorporation of aluminum ions into the composition of pozzolanic concretes is the another important reason for their higher durability than that of their ordinary counterpart subject to chloride ions [67]. Of note, the electrical resistivity test did not take into consideration the aforementioned issue.

As already proved in the literature, the corrosion possibility of the steel rebars is relatively low when the electrical resistivity of the samples is higher than 20 kΩ.cm [68]. The electrical resistivity of the SCM mixes in this research exceeded 20 kΩ.cm. Therefore, the corrosion rate in the samples exposed to chloride ions might be low in this project. As previously shown [17], the electrical resistivity of the samples containing WCP increased upon increasing the WCP content even up to higher amounts.

It should be noted that the slight reduction in the compressive strength was less significant than other issues such as improving the durability of the cementitious samples, reusing waste materials, and reducing the cement consumption.

The total amount of water absorbed by the pores in the SCM samples decreased upon increasing the ratios of pozzolans incorporated in the mortar. The lower the rate of the absorbed water in the pores of the samples, the higher resistance of the mortar exposed to penetration of water solute ions into the samples.

Based on the test results, the SCM mixes prepared with 10-30 % FA showed about 10-15 % and 29-44 % lower water absorption rate than the control mix at the age of 28 and 90 days, respectively. Partial replacement of OPC with WCP had similar effects on the water absorption of mixes. Here, use of 20 % WCP led to up to 9 % and 34 % reduction in the 28- and 90-day water absorption rates, respectively, compared to those in the control mix. Of note, there was a considerable difference between the diagrams of the control and pozzolan-included samples. On the contrary, there was a small difference between the water absorption of mixes made with different contents of pozzolans. In other words, incorporation of pozzolan into the mixture even with a low percentage could significantly decrease the water absorption of SCM mixes; however, further increase in the pozzolan content did not considerably change the water absorption value. As expected, lower water absorption values were obtained when FA and WCP were blended with OPC. As discussed earlier, both FA and WCP were finer than the OPC; therefore, when cement was replaced with FA and WCP, the porosity of the mixes decreased. The finer particles of the FA and WCP could fill the pores and gaps, thereby blocking the permeability channels and reducing the water intake [20,49]. An interesting finding here is that the decrease in the water absorption is contrary to the reduction in the mechanical strength of mixes, indicating that FA and WCP act more as a filler rather than a pozzolanic material. This finding can be approved by the observations of Kannan et al. [17] who showed that WCP could reduce the degree of water absorption; however, the compressive strength was reduced by introducing WCP content into the mix. Similar reports were made by Heidari and Tavakoli [48]. Previous studies highlighted that inclusion of FA also enhanced the concrete durability. Abdalhmid et al. [69] observed that the water absorption of the SCC mixes containing FA constantly decreased upon increasing the FA content. They also stated that the higher workability of the mixes due to FA introduction led to better compaction, which consequently reduced the void content as well as the water absorbed by the specimens. This finding was in agreement with those of the present research since the incorporation of FA increased the flowability of the mixes. It should be noted that both FA and WCP could mitigate the drying shrinkage, one of the critical factors in the micro-cracking of mixes [69,70]. Rafieizonooz et al. [51] observed that the drying shrinkage of the concrete mixes could be effectively controlled by incorporating 20 % FA. With less micro-cracking in the mortar, the possibility of the contraction of the paste would also decrease, and the adhesion between the aggregate and paste would be maintained which in turn improved the quality of the ITZ [54]. The reduction in the water absorption in specimens containing both WCP [9,20] and FA [15] was also reported by other researchers. For instance, Heidari and Tavakoli [20] indicated that partial replacement of OPC with 20 % WCP reduced the water absorption rate by 13.5 % of the corresponding value in the control sample. Jalal et al. [15] showed that cement replacement by FA

could reduce the water absorption by 33.8 and 40 % of the those in the control samples for binder content of 400 and 500 kg/m^3, respectively.

In order to verify the obtained results, SEM analysis was carried out on samples taken from the control mix and mix FA30WC20. Figures 8(a) and (b) demonstrate the SEM images for the control specimen and sample containing 30 % FA and 20 % WCP at the age of 90 days. The Portlandite (calcium hydroxide, $Ca(OH)_2$, CH) crystals are detected in these images in the form of hexagonal plates and calcium silicate hydrate (C-S-H) gel that are identified, which surrounds aggregates and crystalline parts [9].

As indicated in Figure 8(a), the size of CH crystals is about 2 µm in the control sample. There are some micro-cracks in the control specimen, as shown in Figure 8(a). Denser microstructure in the samples containing pozzolan is clearly visible in Figure 8(b). Fewer pores and cracks, smaller or less portlandite crystals, and more C-S-H gels could be found in the microstructure images of the mortar samples containing FA and WCP (Figure 8(b)). As mentioned in the previous sections, the differences between the microstructure of the samples containing pozzolan and plain mortar are due to the delayed pozzolanic reaction, which consumes the CH crystals and produce C-S-H products [49]. Evidently, incorporation of either FA or WCP significantly reduced the number of micro-cracks by filling the micro pores. This finding mechanism was in agreement with the observations of Jain et al. [60] and Li et al. [71]. Generally, use of pozzolans would improve the microstructural properties of the mortar and provide better durability for the samples. This conclusion was previously drawn in the assessment of water absorption and electrical resistivity.

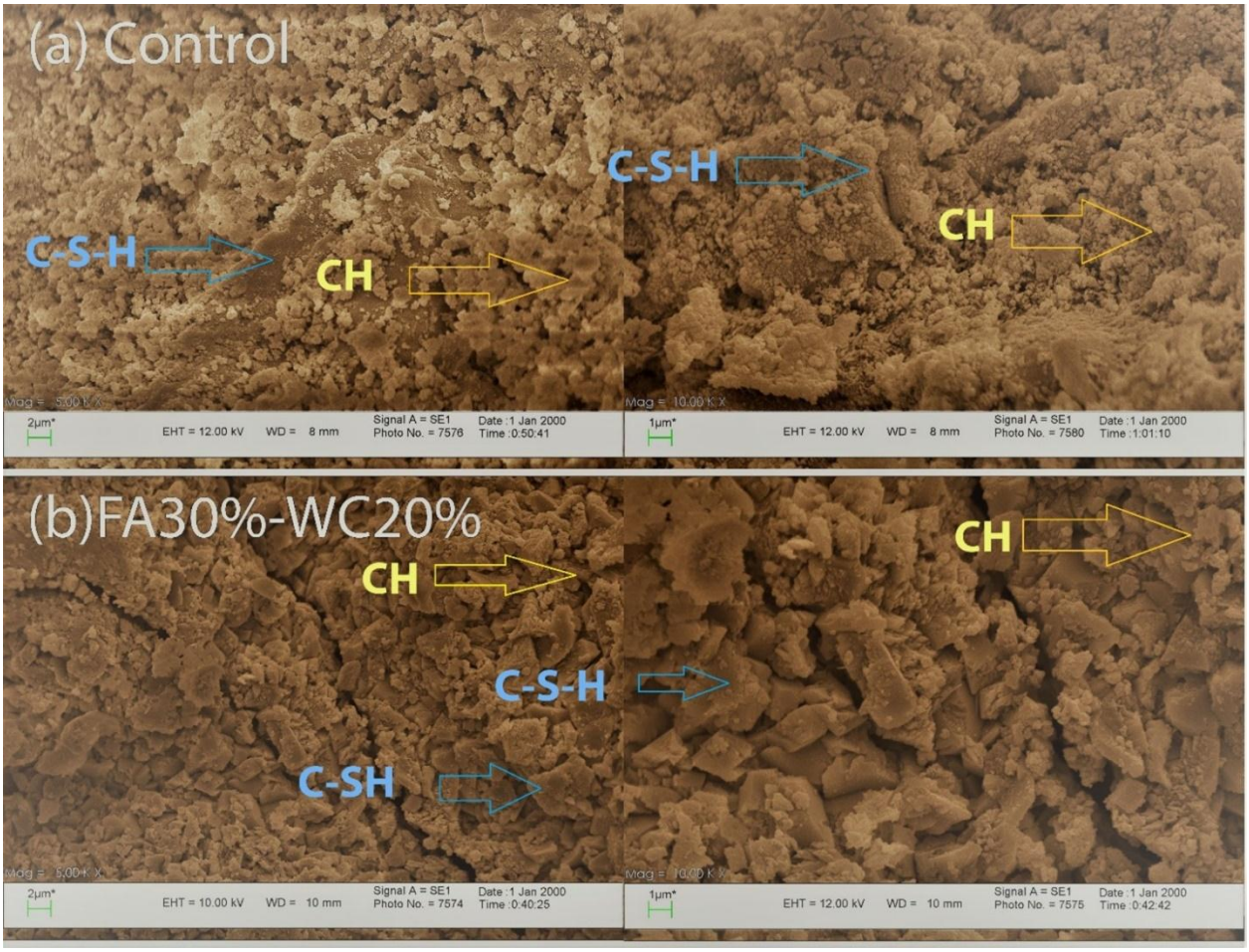

Figure 8. SEM micrograph of SCM (a) Control mix and (b) FA30WC20

3.5. Environmental Analysis

This section compares the environmental impact of the SCM mixes containing different percentages of FA and WCP from the carbon footprint and energy consumption points of view. Contribution of each material to the total ECO_2e and EE of mixes was evaluated based on the factors presented in Table 3. Table 6 presents the total carbon dioxide emission and energy consumed by each

mortar calculated by adding up the contribution of each component. In addition, Figure 9(a) and (b) show the share of each material in the ECO_2e and EE of the mixes, respectively. Based on the environmental analysis results, the application of the pozzolans in this study could effectively mitigate the environmental repercussions of the SCM mixes. For example, incorporating 30 % FA reduced the carbon dioxide emissions and EE by about 28 % and 19 %, respectively. Similarly, 18 % and 10 % reduction in the amounts of ECO_2e and EE, respectively, was observed in the mixes containing WCP, while using 20 % WCP as the partial replacement of cement. As expected, the environmental impact of the ternary blended mixes was lower than the binary blended mixes. The ECO_2e and EE of the mix prepared with 30 % FA, 20 % WCP, and 50 % OPC were about 47 % and 29 %, respectively, lower than those of the control mix, indicating that by reducing the OPC content by 50 %, the carbon footprint of the mix would also be approximately halved. Figures 9(a) and (b) show the share of each component to the total ECO_2e and EE of mixes, respectively. As observed, the largest share in all mixes belonged to the OPC, contributing 95 % and 65 % to the ECO_2e and EE, respectively. The second contributing parameter to the energy demand was the curing water, which was calculated in a 5 m×5 m×0.2 m water tank.

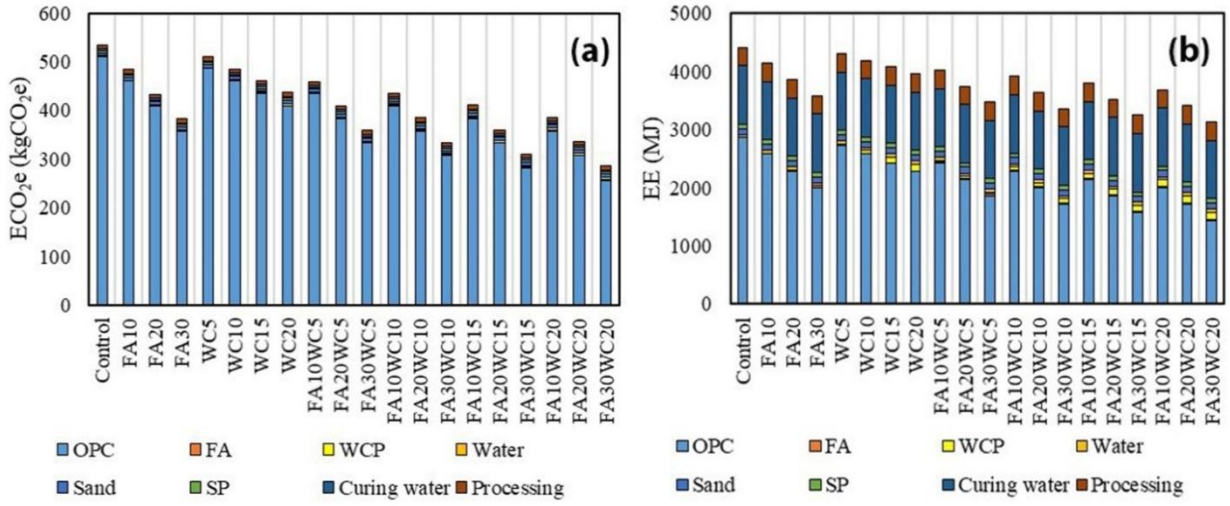

Figure 9. (a) ECO_2e and (b) EE of SCM mixes with different FA and WCP contents

TABLE 6. ECO_2e and EE of mixes

Mix	ECO_2e (kgCO_2e)	EE (MJ)
Control	534.2	4408.9
FA10	483.7	4132.4
FA20	433.3	3855.9
FA30	382.8	3579.4
WC5	509.9	4296.5
WC10	485.6	4184.1
WC15	461.2	4071.7
WC20	436.9	3959.3
FA10WC5	459.4	4020.0
FA20WC5	408.9	3743.5
FA30WC5	358.4	3467.0
FA10WC10	435.1	3907.6
FA20WC10	384.6	3631.1
FA30WC10	334.1	3354.6
FA10WC15	410.7	3795.2
FA20WC15	360.2	3518.7
FA30WC15	309.8	3242.2
FA10WC20	386.4	3682.8
FA20WC20	335.9	3406.3
FA30WC20	285.4	3129.8

The environmental impact assessment can also be evaluated considering the eco-strength efficiency of concrete mixes (Figure 10). This index was obtained in this research by dividing the 90-day compressive strength by the amount of carbon dioxide released in one cubic meter. According to Figure 10, upon increasing the amount of waste tiles and FA at the same time, this amount would significantly increase. This result recommends consideration of this percentage to reduce the amount of produced carbon dioxide.

3.6. ANOVA

ANOVA analysis was carried out on the experimental results to determine the contribution of each variable to the selected properties at different curing ages. Table 7 shows the analysis results for the compressive strength of mixes at different curing ages. As seen in the table, the P-value for all variables was less than 0.05, meaning that all variables had significant contributions to the results. Interestingly, the contributions of FA, WCP, and their interaction varied at different curing ages. At the age of three days, FA had the highest contribution to the compressive strength, the interaction between FA and

WCP comes next, and the WCP content has the least contribution. To be specific, it can be concluded that the FA could patriciate in the chemical reactions more quickly than the WCP at such an early age owing to its higher silica content [46]. As the curing time increased, the contribution of the WCP followed an increasing trend as well. For example, the contribution of WCP to the compressive strength at 7 and 28 days increased up to 37.4 % and 43.4 %, respectively. Meanwhile, the contribution value of the FA remained higher than 50 %, thus highlighting its major impact on the strength development in the SCM mixes. On the contrary, at 90 days, the FA and WCP contribution rates were measured as 68.6 % and 25.6 %, respectively. This finding confirmed the results of the compressive strength where the 90-day compressive strength of the mix containing 30 % FA was about 31 % higher than that of the control mix while the corresponding gain for the mix containing 20 % WCP was about 19 %. Therefore, it can be concluded that the pozzolanic reaction of FA was more productive than that of the WCP between the 28th and 90th days of curing.

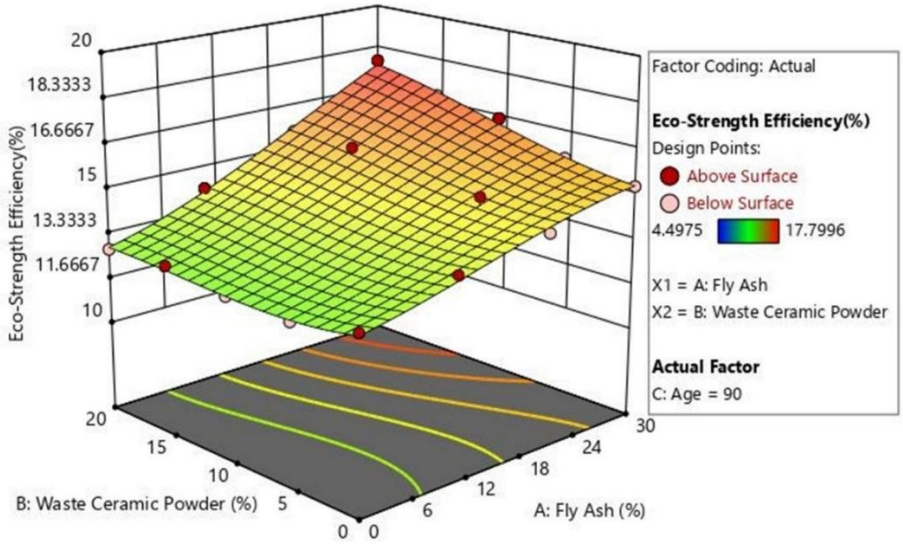

Figure 10. Eco-Strength Efficiency of concrete specimens at 90-days compressive strength

TABLE 7. ANOVA results of compressive strength of SCM mixes at different curing ages

Age	Property	SS	df	MS	F	P-value	F crit	Contribution
3 days	WCP	313.7	4	78.4	106.2	9.5E-21	2.61	17.1 %
	FA	1111.8	3	370.6	502.1	9.2E-32	2.84	60.4 %
	Interaction	384.7	12	32.1	43.4	4.3E-19	2.00	20.9 %
	Error	29.5	40	0.7				1.6 %
7 days	WCP	2097.4	4	524.3	281.3	1.1E-28	2.61	37.4 %
	FA	3169.9	3	1056.6	566.8	8.6E-33	2.84	56.5 %
	Interaction	268.6	12	22.4	12.0	9.2E-10	2.00	4.8 %
	Error	74.6	40	1.9				1.3 %
28 days	WCP	1852.0	4	463.0	170.5	1.5E-24	2.6	43.4 %
	FA	2157.5	3	719.2	264.8	2.1E-26	2.8	50.5 %
	Interaction	153.5	12	12.8	4.7	9.7E-05	2.0	3.6 %
	Error	108.7	40	2.7				2.5 %
90 days	WCP	1012.9	4	253.2	61.5	1.5E-16	2.6	25.6 %
	FA	2718.4	3	906.1	220.2	6.8E-25	2.8	68.6 %
	Interaction	65.3	12	5.4	1.3	2.4E-01	2.0	1.6 %
	Error	164.6	40	4.1				4.2 %

However, the ANOVA results for the flexural strength of mixes was, to some extent, different from those of the compressive strength. The analysis results presented in Table 8 showed that the contributions of FA and WCP did not change over time and remained relatively constant at about 38 % and 45 %, respectively. However,

in agreement with the ANOVA results for the compressive strength, there was an obvious increase in the contribution of FA at the age of 90 days, which can be justified by the reactivity of FA at later ages, as discussed earlier. The ANOVA analysis was also carried out on the durability-related properties investigated in the present research, i.e., the electrical resistivity and water absorption, at 28 and 90 days.

Table 9 and Table 10 present the results regarding the electrical resistivity and water absorption, respectively. Similar to the results of the mechanical properties, it was found that FA had the highest impact on the results, and the interaction between FA and WCP was more significant at 28 days than that at the later ages. Consistent with the results regarding the compressive and flexural strengths, the FA contributions to electrical resistivity and water absorption increased from 19.6 % and 43.8 % (at 28 days) to 65.1 % and 55.8 %, respectively, at 90 days.

TABLE 8. ANOVA results of flexural strength of SCM mixes at different curing ages

Age	Property	SS	df	MS	F	P-value	F crit	Contribution (%)
3 days	WCP	1.76	4	0.44	36.81	6.6E-13	2.61	38.4 %
	FA	2.07	3	0.69	57.56	1.4E-14	2.84	45.1 %
	Interaction	0.28	12	0.02	1.93	5.9E-02	2.00	6.1 %
	Error	0.48	40	0.01				10.4 %
7 days	WCP	2.24	4	0.56	37.21	5.5E-13	2.61	37.9 %
	FA	2.64	3	0.88	58.60	1.1E-14	2.84	44.8 %
	Interaction	0.42	12	0.03	2.32	2.3E-02	2.00	7.1 %
	Error	0.60	40	0.02				10.2 %
28 days	WCP	3.51	4	0.88	33.08	3.3E-12	2.61	38.7 %
	FA	4.12	3	1.37	51.71	7.9E-14	2.84	45.4 %
	Interaction	0.38	12	0.03	1.21	3.1E-01	2.00	4.2 %
	Error	1.06	40	0.03				11.7 %
90 days	WCP	3.89	4	0.97	35.01	1.4E-12	2.61	23.2 %
	FA	11.39	3	3.80	136.69	4.6E-21	2.84	68.0 %
	Interaction	0.37	12	0.03	1.11	3.8E-01	2.00	2.2 %
	Error	1.11	40	0.03				6.6 %

TABLE 9. ANOVA results of electrical resistivity of SCM mixes at different curing ages

Age	Property	SS	df	MS	F	P-value	F crit	Contribution (%)
28 days	WCP	24.53	4	6.13	52.05	2.5E-15	2.61	33.5 %
	FA	14.33	3	4.78	40.55	3.3E-12	2.84	19.6 %
	Interaction	29.59	12	2.47	20.93	1.5E-13	2.00	40.4 %
	Error	4.71	40	0.12				6.4 %
90 days	WCP	1730.66	4	432.67	704.81	1.7E-36	2.61	33.1 %
	FA	3407.16	3	1135.72	1850.08	6.3E-43	2.84	65.1 %
	Interaction	73.74	12	6.15	10.01	1.2E-08	2.00	1.4 %
	Error	24.56	40	0.61				0.5 %

TABLE 10. ANOVA results of water absorption of SCM mixes at different curing ages

Age	Property	SS	df	MS	F	P-value	F crit	Contribution (%)
28 days	WCP	6.60	4	1.65	237.09	2.8E-27	2.61	21.5 %
	FA	13.42	3	4.47	642.77	7.3E-34	2.84	43.8 %
	Interaction	10.35	12	0.86	124.01	1.1E-27	2.00	33.8 %
	Error	0.28	40	0.01				0.9 %
90 days	WCP	33.20	4	8.30	539.20	3.3E-34	2.61	36.2 %
	FA	51.10	3	17.03	1106.55	1.7E-38	2.84	55.8 %
	Interaction	6.67	12	0.56	36.12	1.2E-17	2.00	7.3 %
	Error	0.62	40	0.02				0.7 %

4. CONCLUSIONS

The present research experimentally investigated the rheological, durability, mechanical, and environmental properties of ternary Self-Consolidating Mortars (SCMs). The mix proportions were taken into consideration to evaluate the effects of different mass ratios of WCP and FA on the workability, compressive and flexural strength, water absorption, electrical resistivity, and environmental footprint of SCM samples at different ages. Previous studies have evaluated the effects of both WCP or FA on the performance of SCC mixes; however, no comprehensive study has been conducted on the combined use of these materials. In this regard, the current research aimed to bridge this knowledge gap. Based on the test results, the following conclusions were drawn:

1. Incorporation of FA and WCP into the mixes had a positive impact on the workability of the fresh mortar mixes, which can be attributed to the more spherical shapes of FA and WCP than that of the OPC.
2. The compressive strength of the SCM mixes decreases with incorporation of FA and WCP. Such reduction was more obvious at earlier ages, which can be attributed to the retarding effect of both FA and WCP. The combined use of 20 % WCP and 30 % FA reduced the 28-day compressive strength by about 50 %; however, this value at the 90th was about 27 %, indicating the strength gain resulting from the pozzolanic reaction of both FA and WCP at later ages.
3. Partial replacement of the OPC with FA and WCP had the same effect on the flexural strength of mixes; however, the reduction in the flexural strength was much lower than that in the compressive strength. Followed by substituting 50 % of OPC with FA and WCP (mass ratio of 30:20), the flexural strength decreased by about 15 %, compared to that in the control mix.
4. The the durability-related properties were considerably enhanced by partially replacing OPC with FA and WCP, mainly due to the filling effect of FA and WCP owing to their higher specific surface area than OPC, which densifies the microstructure.
5. The water absorption value was reduced by about 40 % in the mix containing 20 % WCP and 30 % FA, compared to that in the control mix. Similarly, mixes containing pozzolanic materials were characterized by higher electrical resistivity (up to 144 % at 90 days) than the control mix, indicating improvement in interconnectivity of pores. The compact ITZ of the mixes containing pozzolan was verified by SEM examination.
6. Reduction in the mechanical strength and increase in the durability properties of the SCM mixes containing FA and WCP confirmed that these materials acted more as a filler rather than a reactive pozzolan in the OPC-based mixes.
7. The amounts of the embodied CO_2 emitted and EE of WCP and FA were much lower than that of the OPC. The application of WCP and FA as the partial replacement materials of OPC reduced the carbon footprint and energy consumption of SCM mixes by up to 47 % and 29 %, respectively.
8. In summary, ternary blends of FA, WCP, and OPC in self-compacting mixes considerably enhanced their workability and resistance to penetration of harmful substances and significantly reduced the environmental footprint. Such benefits come at a price of lower mechanical strength, which can be compensated by application of several common techniques such as fiber reinforcement or addition of nano-materials.

ACKNOWLEDGEMENT

This research project was conducted at the durability laboratory of department of civil engineering, Islamic Azad University, Dehaghan branch. This project was also financially supported by Islamic Azad University, Dehaghan branch. As a result, the authors express their gratitude to this university.

REFERENCES

1. Vishwakarma, V., Ramachandran, D., "Green Concrete Mix Using Solid Waste and Nanoparticles As Alternatives–A Review", ***Construction and Building Materials***, Vol. 162, (2018), 96-103. https://doi.org/10.1016/j.conbuildmat.2017.11.174
2. Ye, T., Xiao, J., Duan, Z., Li, S., "Geopolymers Made of Recycled Brick and Concrete Powder–A Critical Review", ***Construction and Building Materials***, Vol. 330, (2022), 127232. https://doi.org/10.1016/j.jcou.2018.03.007
3. Murugesan, T., Vidjeapriya, R., Bahurudeen, A., "Reuse of Silica Rich Sugarcane Bagasse Ash in Concrete and Influence of Different Curing on the Performance of Concrete", ***Silicon***, Vol. 14, No. 6, (2022), 3069-3080. https://doi.org/10.1007/s12633-021-01089-1
4. Bheel, N., Memon, F. A., Meghwar, S. L., "Study of Fresh and Hardened Properties of Concrete Using Cement with Modified Blend of Millet Husk Ash as Secondary Cementitious Material", ***Silicon***, Vol. 13, No. 12, (2021), 4641-4652. https://doi.org/10.1007/s12633-020-00794-7
5. Alipour, P., Behforouz, B., Mohseni, E., Zehtab, B., "Investigation of SCC Characterizations Incorporating Supplementary Cementitious Materials", ***Emerging Materials Research***, Vol. 8, No. 3, (2019), 492-507. https://doi.org/10.1680/jemmr.18.00024
6. Ameri, F., Shoaei, P., Bahrami, N., Ameri, F., Shoaei, P., Bahrami, N., Vaezi, M., Ozbakkaloglu, T., "Optimum Rice Husk Ash Content and Bacterial Concentration in Self-Compacting Concrete", ***Construction and Building Materials***, Vol. 222, (2019), 796-813. https://doi.org/10.1016/j.conbuildmat.2019.06.190
7. Nasr, D., Behforouz, B., Borujeni, P. R., Borujeni, S. A., Zehtab, B., "Effect of Nano-Silica on Mechanical Properties and

Durability of Self-Compacting Mortar Containing Natural Zeolite: Experimental Investigations and Artificial Neural Network Modeling", ***Construction and Building Materials***, Vol. 229, (2019), 116888. https://doi.org/10.1016/j.conbuildmat.2019.116888
8. Miyandehi, B. M., Behforouz, B., Khotbehsara, E. M., Balgouri, H. A., Fathi, S., Khotbehsara, M. M., "An Experimental Investigation on Nano-Al_2O_3 Based Self-Compacting Mortar", ***Journal of American Science***, Vol. 10, No. 11, (2014), 229-233. https://doi.org/10.7537/marsjas101114.31
9. Behforouz, B., Memarzadeh, P., Eftekhar, M., Fathi, F., "Regression and ANN Models for Durability and Mechanical Characteristics of Waste Ceramic Powder High Performance Sustainable Concrete", ***Computers and Concrete, An International Journal***, Vol. 25, No. 2, (2020), 119-132. https://doi.org/10.12989/cac.2020.25.2.119
10. Bheel, N., Adesina, A., "Influence of Binary Blend of Corn Cob Ash and Glass Powder as Partial Replacement of Cement in Concrete", ***Silicon***, Vol. 13, No. 5, (2021), 1647-1654. https://doi.org/10.1007/s12633-020-00557-4
11. Bheel, N., Kumar, A., Shahzaib, J., Ali, Z., Ali, M., "An Investigation on Fresh and Hardened Properties of Concrete Blended with Rice Husk Ash as Cementitious Ingredient and Coal Bottom Ash as Sand Replacement Material", ***Silicon***, Vol. 14, No. 2, (2022), 677-688. https://doi.org/10.1007/s12633-020-00906-3
12. Tarighat, A., Zehtab, B., "Structural Reliability of Reinforced Concrete Beams/Columns Under Simultaneous Static Loads and Steel Reinforcement Corrosion", ***Arabian Journal for Science and Engineering***, Vol. 41, No. 10, (2016), 3945-3958. https://doi.org/10.1007/s13369-016-2033-6
13. Malhotra, V., "High-Performance High-Volume Fly Ash Concrete", ***Concrete International***, Vol. 24, No. 7, (2002), 30-34. https://doi.org/10.1016/j.cemconres.2003.11.013
14. Li, G., "Properties of High-Volume Fly Ash Concrete Incorporating Nano-SiO_2", ***Cement and Concrete Research***, Vol. 34, No. 6, (2004), 1043-1049. https://doi.org/10.1016/j.cemconres.2003.11.013
15. Hilal, N., Hadzima-Nyarko, M., "Improvement of Eco-Efficient Self-Compacting Concrete Manufacture by Recycling High Quantity of Waste Materials", ***Environmental Science and Pollution Research***, Vol. 28, No. 38, (2021), 53282–53297. https://doi.org/10.1007/s11356-021-14222-9
16. Alaka, H. A., Oyedele, L. O., "High Volume Fly Ash Concrete: The Practical Impact of Using Superabundant Dose of High Range Water Reducer", ***Journal of Building Engineering***, Vol. 8, (2016), 81-90. https://doi.org/10.1016/j.jobe.2016.09.008
17. Kannan, D. M., Aboubakr, S. H., El-Dieb, A. S., Taha, M. M. R., "High Performance Concrete Incorporating Ceramic Waste Powder As Large Partial Replacement of Portland Cement", ***Construction and Building Materials***, Vol. 144, (2017), 35-41. https://doi.org/10.1016/j.conbuildmat.2017.03.115
18. Ay, N., Ünal, M., "The Use of Waste Ceramic Tile In Cement Production", ***Cement and Concrete Research***, Vol. 30, No. 3, (2000), 497-499. https://doi.org/10.1016/S0008-8846(00)00202-7
19. Tavakoli, D., Hashempour, M., Heidari, A., "Use of Waste Materials in Concrete: A Review", ***Pertanika Journal of Science & Technology***, Vol. 26, No. 2, (2018), 499-522. http://www.pertanika.upm.edu.my/resources/files/Pertanika%20PAPERS/JST%20Vol.%2026%20(2)%20Apr.%202018/02%20JST%20Vol%2026%20(2)%20Apr%202018_JST-0849-2017_pg499-522.pdf
20. Heidari, A., Tavakoli, D., "A Study of the Mechanical Properties of Ground Ceramic Powder Concrete Incorporating Nano-SiO_2 Particles", ***Construction and Building Materials***, Vol. 38, (2013), 255-264. https://doi.org/10.1016/j.conbuildmat.2012.07.110
21. Ameri, F., Zareei, S. A., Behforouz, B., "Zero-Cement vs. Cementitious Mortars: An Experimental Comparative Study on Engineering and Environmental Properties", ***Journal of Building Engineering***, Vol. 32, (2020), 101620. https://doi.org/10.1016/j.jobe.2020.101620
22. Halicka, A., Ogrodnik, P., Zegardlo, B., "Using Ceramic Sanitary Ware Waste as Concrete Aggregate", ***Construction and Building Materials***, Vol. 48, (2013), 295-305. https://doi.org/10.1016/j.conbuildmat.2013.06.063
23. Zareei, S. A., Ameri, F., Bahrami, N., Shoaei, P., Musaeei, H. R., Nurian, F., "Green High Strength Concrete Containing Recycled Waste Ceramic Aggregates and Waste Carpet Fibers: Mechanical, Durability, and Microstructural Properties", ***Journal of Building Engineering***, Vol. 26, (2019), 100914. https://doi.org/10.1016/j.jobe.2019.100914
24. Subaşı, S., Öztürk, H., Emiroğlu, M., "Utilizing of Waste Ceramic Powders As Filler Material in Self-Consolidating Concrete", ***Construction and Building Materials***, Vol. 149, (2017), 567-574. https://doi.org/10.1016/j.conbuildmat.2017.05.180
25. Higashiyama, H., Yagishita, F., Sano, M., Takahashi, O., "Compressive Strength and Resistance to Chloride Penetration of Mortars Using Ceramic Waste As Fine Aggregate", ***Construction and Building Materials***, Vol. 26, No. 1, (2012), 96-101. https://doi.org/10.1016/j.conbuildmat.2011.05.008
26. Pavlík, Z., Trník, A., Kulovaná, T., Scheinherrová, L., Rahhal, V., Irassar, E., Černý, R., "DSC and TG Analysis of a Blended Binder Based on Waste Ceramic Powder and Portland Cement", ***International Journal of Thermophysics***, Vol. 37, No. 3, (2016), 1-14. https://doi.org/10.1007/s10765-016-2043-3
27. Wardhono, A., "Comparison Study of Class F and Class C Fly Ashes as Cement Replacement Material on Strength Development of Non-Cement Mortar", In ***IOP Conference Series: Materials Science and Engineering***, IOP Publishing, Vol. 288, No. 1, (2018), 012019. https://doi.org/10.1088/1757-899x/288/1/012019
28. ASTM, ***Standard Specification for Coal Fly Ash and Raw or Calcined Natural Pozzolan for Use in Concrete***, ASTM C618-19, ASTM International, West Conshohocken, PA, USA, (2019).
29. EUROPEAN STANDARD, ***Tests for Geometrical Properties of Aggregates–Part 4: Determination of Particle Shape–Shape Index***, DIN EN 933-4:2008-06, European Committee for Standardization, Brussels, Belgium, (2008).
30. Esquinas, A. R., Álvarez, J. I., Jiménez, J. R., Fernández, J. M., "Durability of Self-Compacting Concrete Made from Non-Conforming Fly Ash from Coal-Fired Power Plants", ***Construction and Building Materials***, Vol. 189, (2018), 993-1006. https://doi.org/10.1016/j.conbuildmat.2018.09.056
31. Khatib, J. M., "Performance of Self-Compacting Concrete Containing Fly Ash", ***Construction and Building Materials***, Vol. 22, No. 9, (2008), 1963-1971. https://doi.org/10.1016/j.conbuildmat.2007.07.011
32. Wongkeo, W., Thongsanitgarn, P., Ngamjarurojana, A., Chaipanich, A., "Compressive Strength and Chloride Resistance of Self-Compacting Concrete Containing High Level Fly Ash and Silica Fume", ***Materials & Design***, Vol. 64, (2014), 261-269. https://doi.org/10.1016/j.matdes.2014.07.042
33. Rantung, D., Supit, S. W., Nicolaas, S., "Effects of Different Size of Fly Ash As Cement Replacement on Self-Compacting Concrete Properties", ***Journal of Sustainable Engineering: Proceedings Series***, Vol. 1, No. 2, (2019), 180-186. https://doi.org/10.35793/joseps.v1i2.25
34. Duran-Herrera, A., De-León-Esquivel, J., Bentz, D., Valdez-Tamez, P., "Self-Compacting Concretes Using Fly Ash and Fine Limestone Powder: Shrinkage and Surface Electrical Resistivity of Equivalent Mortars", ***Construction and Building Materials***, Vol. 199, (2019), 50-62. https://doi.org/10.1016/j.conbuildmat.2018.11.191
35. Dinakar, P., Babu, K. G., Santhanam, M., "Durability Properties of High Volume Fly Ash Self Compacting Concretes", ***Cement and Concrete Composites***, Vol. 30, No. 10, (2008), 880-886. https://doi.org/10.1016/j.cemconcomp.2008.06.011
36. Leemann, A., Loser, R., Münch, B., "Influence of Cement Type on ITZ Porosity and Chloride Resistance of Self-Compacting Concrete", ***Cement and Concrete Composites***, Vol. 32, No. 2, (2010), 116-120. https://doi.org/10.1016/j.cemconcomp.2009.11.007
37. ASTM, ***Standard Specification for Portland Cement***, ASTM

C150/C150M-20, ASTM International, West Conshohocken, PA, USA, (2020).
38. BRITISH STANDARD, ***Tests for Geometrical Properties of Aggregates-Part 10: Assessment of Fines-Grading of Filler Aggregates (Air Jet Sieving)***, BS EN 933-10:2009, British Standards Institution, Brussels, Belgium, (2009).
39. ASTM, ***Standard Specification for Standard Sand***, ASTM C778-17, ASTM International, West Conshohocken, PA, USA, (2017).
40. EFNARC, ***Specification and Guidelines for Self-Compacting Concrete***, European Federation for Specialist Construction Chemicals and Concrete Systems, Norfolk, UK, English ed., February, (2002).
41. Standard, A. S. T. M., ***ASTM C109-Standard Test Method for Compressive Strength of Hydraulic Cement Mortars***, ASTM International, West Conshohocken, PA, USA, (2008).
42. ASTM, ***Standard Test Method for Flexural Strength of Concrete (Using Simple Beam with Third-Point Loading)***, ASTM C78/C78M-18, ASTM International, West Conshohocken, PA, USA, (2018).
43. ASTM, ***Standard Test Method for Density, Absorption, and Voids in Hardened Concrete***; ASTM C642, ASTM International, West Conshohocken, PA, USA, (2013).
44. ASTM, ***Standard Test Method for Bulk Electrical Conductivity of Hardened Concrete***, ASTM C1760-12, ASTM International, West Conshohocken, PA, USA, (2012).
45. Sengul, O., "Use of Electrical Resistivity as An Indicator for Durability", ***Construction and Building Materials***, Vol. 73, (2014), 434-441. https://doi.org/10.1016/j.conbuildmat.2014.09.077
46. Huseien, G. F., Sam, A. R. M., Shah, K. W., Mirza, J., Tahir, M. M., "Evaluation of Alkali-Activated Mortars Containing High Volume Waste Ceramic Powder and Fly Ash Replacing GBFS", ***Construction and Building Materials***, Vol. 210, (2019), 78-92. https://doi.org/10.1016/j.conbuildmat.2019.03.194
47. Tanyildizi, H., Şahin, M., "Application of Taguchi Method for Optimization of Concrete Strengthened with Polymer after High Temperature", ***Construction and Building Materials***, Vol. 79, (2015), 97-103. https://doi.org/10.1016/j.conbuildmat.2019.03.194
48. Heidari, A., Tavakoli, D., "Performance of Ceramic Tile Powder As A Pozzolanic Material in Concrete", ***International Journal of Advanced Materials Science***, Vol. 3, No. 1, (2012), 1-11. https://www.ripublication.com/Volume/ijamsv3n1.htm
49. Jain, A., Gupta, R., Chaudhary, S., "Sustainable Development of Self-Compacting Concrete by Using Granite Waste and Fly Ash", ***Construction and Building Materials***, Vol. 262, (2020), 120516. https://doi.org/10.1016/j.conbuildmat.2020.120516
50. Jun, C., Gengying, L., "Mechanical Properties and Drying Shrinkage of Self-Compacting Concrete Containing Fly Ash", ***Revista Română de Materiale / Romanian Journal of Materials***, Vol. 46, No. 4, (2016), 480-484. https://www.revista-romana-de-materiale.upb.ro/administrare/content/doc/2016/4/11/server/files/articol.pdf
51. Rafieizonooz, M., Mirza, J., Salim, M. R., Hussin, M. W., Khankhaje, E., "Investigation of Coal Bottom Ash and Fly Ash in Concrete As Replacement for Sand and Cement", ***Construction and Building Materials***, Vol. 116, (2016), 15-24. https://doi.org/10.1016/j.conbuildmat.2016.04.080
52. Hilal, N., Saleh, R. D., Yakoob, N. B., Banyhussan, Q. S., "Utilization of Ceramic Waste Powder in Cement Mortar Exposed to Elevated Temperature", ***Innovative Infrastructure Solutions***, Vol. 6, No. 1, (2021), 1-12. https://doi.org/10.1007/s41062-020-00403-x
53. Prajapati, L., Patel, I. N., Agrawal, V. V., "Analysis of the Strength and Durability of the Concrete with Partially Replaced by the Ceramic Slurry Waste Powder", ***International Journal of Emerging Technology and Advanced Engineering***, Vol. 4, No. 3, (2014), 725-729. https://www.researchgate.net/profile/Vimlesh-Agrawal/publication/314183355_Analysis_Of_The_Strength_And_Durability_Of_The_Concrete_With_Partially_Replaced_By_The_Ceramic_Slurry_Waste_Powder/links/5efb0b41a6fdcc4ca43da388/Analysis-Of-The-Strength-And-Durability-Of-The-Concrete-With-Partially-Replaced-By-The-Ceramic-Slurry-Waste-Powder.pdf
54. Chindaprasirt, P., Homwuttiwong, S., Sirivivatnanon, V., "Influence of Fly Ash Fineness on Strength, Drying Shrinkage and Sulfate Resistance of Blended Cement Mortar", ***Cement and Concrete Research***, Vol. 34, No. 7, (2004), 1087-1092. https://doi.org/10.1016/j.cemconres.2003.11.021
55. Ferrara, L., Deegan, P., Pattarini, A., Sonebi, M., Taylor, S., "Recycling Ceramic Waste Powder: Effects Its Grain-Size Distribution on Fresh and Hardened Properties of Cement Pastes/Mortars Formulated from SCC Mixes", ***Journal of Sustainable Cement-Based Materials***, Vol. 8, No. 3, (2019), 145-160. https://doi.org/10.1080/21650373.2018.1564396
56. Magudeaswaran, P., Eswaramoorthi, P., "Experimental Investigations of Mechanical Properties on Micro Silica (Silica Fume) and Fly Ash as Partial Cement Replacement of High Performance Concrete", ***IOSR Journal of Mechanical and Civil Engineering***, Vol. 6, No. 4, (2013), 57-63. https://doi.org/10.9790/1684-645763
57. ***Iranian Concrete Code (ABA)***, Management and Planning Organization of I. R. Iran, No. 120, Iran, (2001).
58. American Concrete Institute, ***Building Code Requirements for Structural Concrete (ACI 318-14): An ACI Standard: Commentary on Building Code Requirements for Structural Concrete (ACI 318R-14), an ACI Report***, American Concrete Institute, (2012).
59. Canadian Standards Association, ***Design of Concrete Structures (Update No. 2-July 2007)***, CAN/CSA A23. 3-04, Canadian Standards Association, Mississauga, Ontario, Canada, (2004).
60. British Standards Institution, ***Eurocode 2: Design of Concrete Structures-Part 1–1: General Rules and Rules for Buildings***, BS EN 1992-1-1:2004, British Standard Institution, London, UK, (2004).
61. New Zealand Standard, ***Concrete Structures Standard***, NZS 3101:2006, The Design of Concrete Structures, Wellington, New Zealand, (2006).
62. Zamanabadi, S. N., Zareei, S. A., Shoaei, P., Ameri, F., "Ambient-Cured Alkali-Activated Slag Paste Incorporating Micro-Silica As Repair Material: Effects of Alkali Activator Solution on Physical and Mechanical Properties", ***Construction and Building Materials***, Vol. 229, (2019), 116911. https://doi.org/10.1016/j.conbuildmat.2019.116911
63. Kurda, R., de Brito, J., Silvestre, J. D., "Water Absorption and Electrical Resistivity of Concrete with Recycled Concrete Aggregates and Fly Ash", ***Cement and Concrete Composites***, Vol. 95, (2019), 169-182. https://doi.org/10.1016/j.cemconcomp.2018.10.004
64. Zehtab, B., Tarighat, A., "Molecular Dynamics Simulation to Assess the Effect of Temperature on Diffusion Coefficients of Different Ions and Water Molecules in CSH", ***Mechanics of Time-Dependent Materials***, Vol. 22, No. 4, (2018), 483-497. https://doi.org/10.1007/s11043-017-9368-6
65. Zehtab, B., Tarighat, A., "Diffusion Study for Chloride Ions and Water Molecules in CSH Gel in Nano-Scale Using Molecular Dynamics: Case Study of Tobermorite", ***Advances in Concrete Construction***, Vol. 4, No. 4, (2016), 305-317. https://doi.org/10.12989/acc.2016.4.4.305
66. Bremner, T., Hover, K., Poston, R., Broomfield, J., Joseph, T., Price, R., Clear, K., Khan, M., Reddy, D., Clifton, J., Manning, D., Savoly, A., Daily, S., McDonald, D., Scannell, W., Daye, M., McGettigan, E., Schupack, M., Decker, E., Montani, R., Soudki, K., Didelot, R., Nagi, M., Trejo, D., Erlin, B., Neff, T., Weil, T., Grant, J., Pashina, K., West, J., Gu, P., Perenchio, W., Weyers, R., Hamilton, T., "ACI 222R-01 Protection of Metals in Concrete Against Corrosion", In ***Technical Report for ACI Committee 222***, American Concrete Institute, Farmington Hills, MI, USA, (2001). http://dl.mycivil.ir/dozanani/ACI/ACI%20222R-01%20Protection%20of%20Metals%20in%20Concrete%20Against%20Corrosion_MyCivil.ir.pdf

67. Zehtab, B., Tarighat, A., "Effects of Aluminum Incorporation in Tobermorite Structure on Chloride Diffusion: A Molecular Dynamics Simulation Study", ***Civil Engineering Infrastructures Journal***, Vol. 53, No. 1, (2020), 1-13. https://doi.org/10.22059/ceij.2019.255014.1475
68. Broomfield, J. P., ***Corrosion of Steel in Concrete: Understanding, Investigation and Repair***, 2nd Ed., CRC Press, London, UK, (2003).
69. Abdalhmid, J. M., Ashour, A. F., Sheehan, T., "Long-Term Drying Shrinkage of Self-Compacting Concrete: Experimental and Analytical Investigations", ***Construction and Building Materials***, Vol. 202, (2019), 825-837. https://doi.org/10.1016/j.conbuildmat.2018.12.152
70. Atiş, C. D., "High-Volume Fly Ash Concrete with High Strength and Low Drying Shrinkage", ***Journal of Materials in Civil Engineering***, Vol. 15, No. 2, (2003), 153-156. https://doi.org/10.1061/(ASCE)0899-1561(2003)15:2(153)
71. Li, L., Liu, W., You, Q., Chen, M., Zeng, Q., "Waste Ceramic Powder as a Pozzolanic Supplementary Filler of Cement for Developing Sustainable Building Materials", ***Journal of Cleaner Production***, Vol. 259, (2020), 120853. https://doi.org/10.1016/j.jclepro.2020.120853

Advanced Ceramics Progress: Vol. 8, No. 2, (Spring 2022) 53-60

Materials and Energy Research Center
MERC

Contents lists available at ACERP

Advanced Ceramics Progress

Journal Homepage: www.acerp.ir

Original Research Article

A Comparative Study on the Phase Stability of ZrO_2-8 wt. % Y_2O_3 : Nano- and Micro-Particles

Milad Bahamirian [a, *]

[a] *Assistant professor, Department of Mining and Metallurgical Engineering, Yazd University, Yazd, Yazd, Iran*

* Corresponding Author Email: m.bahamirian@yazd.ac.ir (M. Bahamirian)

URL: https://www.acerp.ir/article_159835.html

ARTICLE INFO

Article History:

Received 17 July 2022
Received in revised form 05 September 2022
Accepted 24 September 2022

Keywords:

Thermal Barrier Coatings (TBCs)
YSZ : ZrO_2-8 wt. % Y_2O_3
Wet-Chemical Method
Phase Stability

ABSTRACT

At temperatures above 1200 °C, the phase instability of micro-YSZ : ZrO_2-8 wt. % Y_2O_3 is one of the major causes of damage to Thermal Barrier Coatings (TBCs) of the latest generation of gas turbines. In this study, nano-YSZ was produced using a wet chemical method to improve the phase stability of micro-YSZ. The phase stability of both synthesized nano-YSZ and commercially available micro-YSZ was examined after 50 h of heat treatment at 1300 °C. The data obtained from X-Ray Diffraction (XRD) analysis of nano-YSZ confirmed the formation of the non-transformable tetragonal (tetragonality parameter : $\frac{c}{a\sqrt{2}} < 1.01$) phase of ZrO_2 and its improved stability followed by heat treatment. Micro-YSZ, however, was decomposed into two new phases, i.e., monoclinic and cubic ZrO_2 with the wight percentages of 38 % and 62 wt. %, respectively, under comparable conditions. The morphological features of nano-YSZ were assessed by Field Emission Scanning Electron Microscopy (FESEM), the results of which confirmed the formation of YSZ nanoparticles with an average size of 40 nm. According to the findings, nano-YSZ could be a suitable candidate for use in TBCs of the next generations of gas turbines.

https://doi.org/10.30501/acp.2022.352174.1097

1. INTRODUCTION

Thermal Barrier Coatings (TBCs) have numerous applications in the hot areas of gas turbines and aviation engines that protect metallic components from the damaging effects of combustion chamber heat [1-3]. TBCs are typically deposited on hot pieces (with Ni and Co-based superalloys) by thermal spray techniques. They include two layers: (i) a bond coat of metallic elements with the composition MCrAlY (M could be Ni or Co) that provides proper resistance to high-temperature oxidation [4-6] and hot corrosion [7-9] and (ii) a ceramic top coat [2,3]. For this reason, coat compositions have been developed based on ZrO_2 that are characterized by excellent properties such as low proper thermal conductivity ($k_{top\ coat}$ = 0.7-2.4 W/mK), thermal expansion coefficient ($\alpha_{top\ coat}$ ~ 7.5-10.5×10^{-6} K^{-1}) that is relatively compatible with the substrate ($\alpha_{superalloy}$ ~ 15-17×10^{-6} K^{-1} and $\alpha_{bond\ coat}$ ~ 10-12×10^{-6} K^{-1}), and resistance to high-temperature oxidation and hot corrosion as well as the thermal shock [2,3,10].

ZrO_2 can be found in three allotropic forms namely monoclinic (m), tetragonal (t), and cubic (c). The phase transformation from m-ZrO_2 to t-ZrO_2 is reversible that occurs at ~ 1170 °C while such transformation to m-ZrO_2 phase takes place at ~ 950 °C during the cool-down cycle.

Please cite this article as: Bahamirian M., "A Comparative Study on the Phase Stability of ZrO_2-8 wt. % Y_2O_3 : Nano- and Micro-Particles", ***Advanced Ceramics Progress***, Vol. 8, No. 2, (2022), 53-60. https://doi.org/10.30501/acp.2022.352174.1097

This phase transition can result in a volume variation in the range of 3-5 %, thus leading to cracks formation and eventually disintegration [2,3,11,12]. Stabilizing oxides such as Y_2O_3, MgO, CaO, and CeO_2 are used to prevent transition in the cool-down cycles [10,13]. One of the most well-known and commonly used compositions in this area is Y_2O_3-stabilized ZrO_2 (ZrO_2-8 wt. % Y_2O_3 or YSZ) [3].

Incorporation of the stabilizers into ZrO_2 leads to the formation of the non-transformable tetragonal phase (t'). The t´-ZrO_2 phase is crystallographically similar to the t-ZrO_2 phase; however, it has a smaller tetragonality ($\frac{c}{a\sqrt{2}}$, "c" and "a" represent the lattice parameters of the tetragonal ZrO_2 system) than that of its counterpart. During the cool-down cycles, such a phase will not change into m-ZrO_2 [14]. This phase (t´-ZrO_2) also possesses lower thermal conductivity [15] and better mechanical properties [16] than those of the other ZrO_2 phases. Therefore, this phase is highly favorable in the TBCs [17-19].

According to Equation (1), two phases of Y-rich (c-ZrO_2) and Y-dilute (t-ZrO_2) will be formed in micro-YSZ at the temperatures above 1200 °C. A phase transition from
t'-ZrO_2 to t-ZrO_2 also occurs in the micro-YSZ at temperatures above 1200 °C after which, the t-ZrO_2 will be transformed into m-ZrO_2 by cooling down to the ambient temperature [12].

$$\begin{matrix} \text{T-prime} \xrightarrow{1200\,^{\circ}\text{C (Heating)}} \text{Tetragonal and} \\ \text{Cubic} \xrightarrow{950^{\circ}\text{C (Cooling)}} \text{Cubic + Monoclinic} \end{matrix} \quad (1)$$

Recent studies [4,7,12,20-23] have emphasized the role of smaller ZrO_2 particles in decreasing the tetragonality and enhancing the stability of the t´-ZrO_2 by using the nano-TBCs in the new generation of turbines that can operate at temperatures above 1200 °C. Given the increasing demands for such new generation of gas turbines, the development of ZrO_2-based TBCs requires more precise investigations.

Several methods for production of ceramic nanoparticles have been proposed to date including mechanical milling, chemical procedures, hydrothermal synthesis, chemical vapor synthesis, co-precipitation, and sol-gel techniques, to name a few [17,23,24]. Low synthesis temperature, cost-effectiveness, controlled synthesis parameters, and remarkable capacity to control the chemical composition are among the advantages of the co-precipitation process [23].

To the best of our knowledge, a limited number of studies have addressed these powders and their applications. Therefore, the necessity of investigating the high-temperature phase stability behavior of nano-YSZ powders comes to the fore. The present study used a co-precipitation approach for the synthesis of nano-YSZ. After 50 hours of heat treatment at 1300 °C, the phase stability of the samples was evaluated, and the results were compared with those of the commercial micro-YSZ.

2. MATERIALS AND METHODS

Co-precipitation process is required to prepare nano-YSZ powder. Figure 1 lists the steps required for the synthesis process.

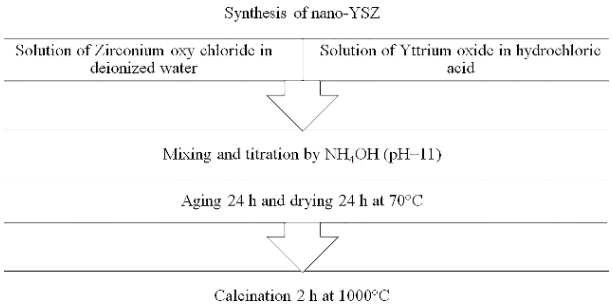

Figure 1. Procedure for the experimental synthesis of nano-YSZ through the co-precipitation method

$ZrOCl_2.8H_2O$ and Y_2O_3 with a purity of 99.9 % (Table 1) were used to supply Zr^{4+} and Y^{3+}, respectively.

TABLE 1. Chemical composition of materials used in fabricating nano-YSZ

Material	Chemical Formula	Purity	Company
Zirconium Oxychloride	$ZrOCl_2.8H_2O$	99.9 %	Merck
Yttrium Oxide	Y_2O_3	99.9 %	Merck

Y_2O_3 was dissolved in HCl to release Y^{3+} ions, as seen in Figure 1. Then, $ZrOCl_2.8H_2O$ was dissolved in double-distilled water. The solutions were mixed, and NH_4OH was gradually added to accelerate the reaction by keeping the pH above 11. The precipitate was rinsed with distilled water and passed through the appropriate filters. It was then dried for 24 hours at 70 °C. The precipitates were then calcined for two hours at 1000 °C.

To investigate the phase stability, micro-YSZ (Metco 204NS-G: ZrO_2-8 wt. % Y_2O_3) and nano-YSZ samples were heat-treated for 50 h at 1300 °C in five-hour cycles. The heating rate was measured as 10 °C/min at the temperatures ranging from the room temperature to 1300 °C and once the peak temperature is reached, the samples were kept for five hours and finally cooled down to the room temperature at the furnace cooling rate. This procedure was selected considering the parameters generally used for cyclic high temperature phase stability of TBCs [12,25]. The crystallographic variation of the samples was assessed at four intervals of t = 0, 10, 20, and 50 h.

To investigate the phases and morphological features

of micro-YSZ and nano-YSZ samples, Field Emission Scanning Electron Microscopy (FESEM) and X-Ray Diffraction (XRD) techniques were employed. Table 2 lists the characteristics of the applied techniques. Material Analysis Using Diffraction (MAUD) software was also for quantitative analysis of the XRD results through Rietveld refinement technique.

TABLE 2. Specifications and parameters of analysis equipment

Equipment	Equipment Model	Parameters
FESEM	MIRA3TESCAN-XMU	
XRD	Philips X'pert X-Ray Diffraction	2θ = 20 - 80° Step Size = 0.02 Time per Step = 0.5 s $\lambda_{Cu\ k\alpha}$ = 1.540598 Å 40 kV, 40 mA T = 25 °C

3. RESULTS AND DISCUSSION

Figure 2 depicts the results of XRD and FESEM analyses of commercial micro-YSZ powder before and after heat treatment (0, 10, 20, and 50 h) at 1300 ºC.

According to Figure 2, the commercial micro-YSZ powder contained a tetragonal ZrO_2 phase (JCDPS: # 01-082-1242). The micro-YSZ, however, exhibited some weak peaks of monoclinic ZrO_2 (JCDPS: # 01-078-1807) amounting to 7 wt. % according to the Rietveld method.

Figure 3 Shows the results of XRD and FESEM analysis for the synthesized nano-YSZ powder before (calcination at 1000 ºC for 2 h) and after heat-treatment (0, 10, 20, and 50 h) at 1300 ºC.

According to Figure 3, the nano-YSZ powder has a tetragonal ZrO_2 phase (JCDPS: # 01-082-1242). However, it exhibits some weak peaks of monoclinic ZrO_2 (JCDPS: # 01-078-1807) amounting to 3 wt. % according to the Rietveld refinement method.

Tetragonality ($\frac{c}{a\sqrt{2}}$), is a determining factor in investigating the stability of the tetragonal phase [23,26]. The tetragonality of the non-transformable (t') and transformable (t) tetragonal phases can be separated. If $\frac{c}{a\sqrt{2}} > 1.01$, the transformable tetragonal phase is stable. On the contrary, if $\frac{c}{a\sqrt{2}} < 1.01$, the non-transformable tetragonal phase is stable [23,27]. Since the calculated tetragonality values of the synthesized nano-YSZ and commercial micro-YSZ (by the Rietveld method) were $\frac{c}{a\sqrt{2}} = \frac{5.163}{3.645\sqrt{2}} = 1.001$ and $\frac{c}{a\sqrt{2}} = \frac{5.177}{3.641\sqrt{2}} = 1.005$, respectively, both samples had a non-transformable tetragonal phase of ZrO_2 before heat treatment at 1300 ºC.

According to Figure 2, the peaks related to 2θ = 27-33° (111) and 2θ = 72-76° (400) (corresponding to the monoclinic and tetragonal/cubic ZrO_2, respectively) emerged by prolonging the heat-treatment process. The presence of the mentioned peaks is indicative of the $t \longrightarrow m$ phase transformation in the cooling cycles and instability of the micro-YSZ. Upon prolonging the heat-treatment duration, the weight percentage of the monoclinic phase increased from 7 to 38 wt. %. In addition, the cubic phase (62 wt. %) was also formed (50 h at 1300 °C).

According to the quantitative calculations of the XRD results based on the Rietveld method, the tetragonality values of the nano-YSZ powder were obtained as $\frac{c}{a\sqrt{2}} = \frac{5.163}{3.645\sqrt{2}} = 1.001$, $\frac{c}{a\sqrt{2}} = \frac{5.144}{3.634\sqrt{2}} = 1.0009$, $\frac{c}{a\sqrt{2}} = \frac{5.145}{3.635\sqrt{2}} = 1.0008$, and $\frac{c}{a\sqrt{2}} = \frac{5.147}{3.637\sqrt{2}} = 1.0006$ after 0, 10, 20, and 50 hours of heat-treatment, respectively, at 1300 °C (Figure 3). Qualitative and quantitative results of the XRD analysis confirmed the stability of the t´-phase ZrO_2 and absence of the cubic and monoclinic phases in the nano-YSZ samples after 50 hours of heat-treatment at 1300 °C.

In the XRD analysis of the YSZ composition, differentiation of the structures of "t" and "c" ZrO_2 requires careful examination of the (400)/(004) peaks at the angle ranges of 72-76°. The "c" phase at these angles is observed as a single peak while the "t" phase is shown in split peaks [28,29].

Figure 2 presents the peak associated with (111) and (400) plates ("m", "t", and "c") for the micro-YSZ sample after 0, 10, 20, and 50 hours of heat-treatment at 1300 °C. The peaks of (111) "m" and (400) "c" emerged by prolonging the heat-treatment duration. The presence of the mentioned peaks is indicative of the phase transformation of the "t" to the "m" during the cooling process and phase instability of the micro-YSZ compound.

$t \longrightarrow m$ phase transformation in the ZrO_2-based compounds can be thermodynamically assessed. According to the available theories mentioned in [30], the initiation temperature of $t \longrightarrow m$ phase transformation can be attributed to the stability of these two phases. The stability of these two phases depends on the surface "γ_s" and volume "γ_v" free energies of the particles. The free energy of the monoclinic phase is lower than that of the tetragonal phase ($\gamma_v^m \leq \gamma_v^t$), and the surface free energy of the tetragonal phase is lower than the monoclinic ($\gamma_s^t \leq \gamma_s^m$) one. In this situation, when the mean particle size of the ZrO_2 powder is smaller than a critical value in the given temperature ($r \leq r^*$), the role of the surface free energy (γ_s) will be more determinative than the volume free energy (γ_v) [30-33]. Therefore, the stability of the tetragonal ZrO_2 phase is thermodynamically feasible.

Upon increasing the particle size ($r \geq r^*$), the monoclinic phase will be stable. Therefore, in the case of nano-YSZ, the particle size of the ZrO_2 powder after 50 hours of heat treatment at 1300 °C is still smaller than the critical size (r^*) to provide the possibility of $t \longrightarrow m$ phase

transformation; therefore, the thermodynamic condition of transformation from the tetragonal to monoclinic phases is not fulfilled. In the case of micro-YSZ, the larger initial sizes of the ZrO_2 particles in addition to their growth during the heat-treatment process provided the thermodynamic condition for $t \longrightarrow m$ phase transformation.

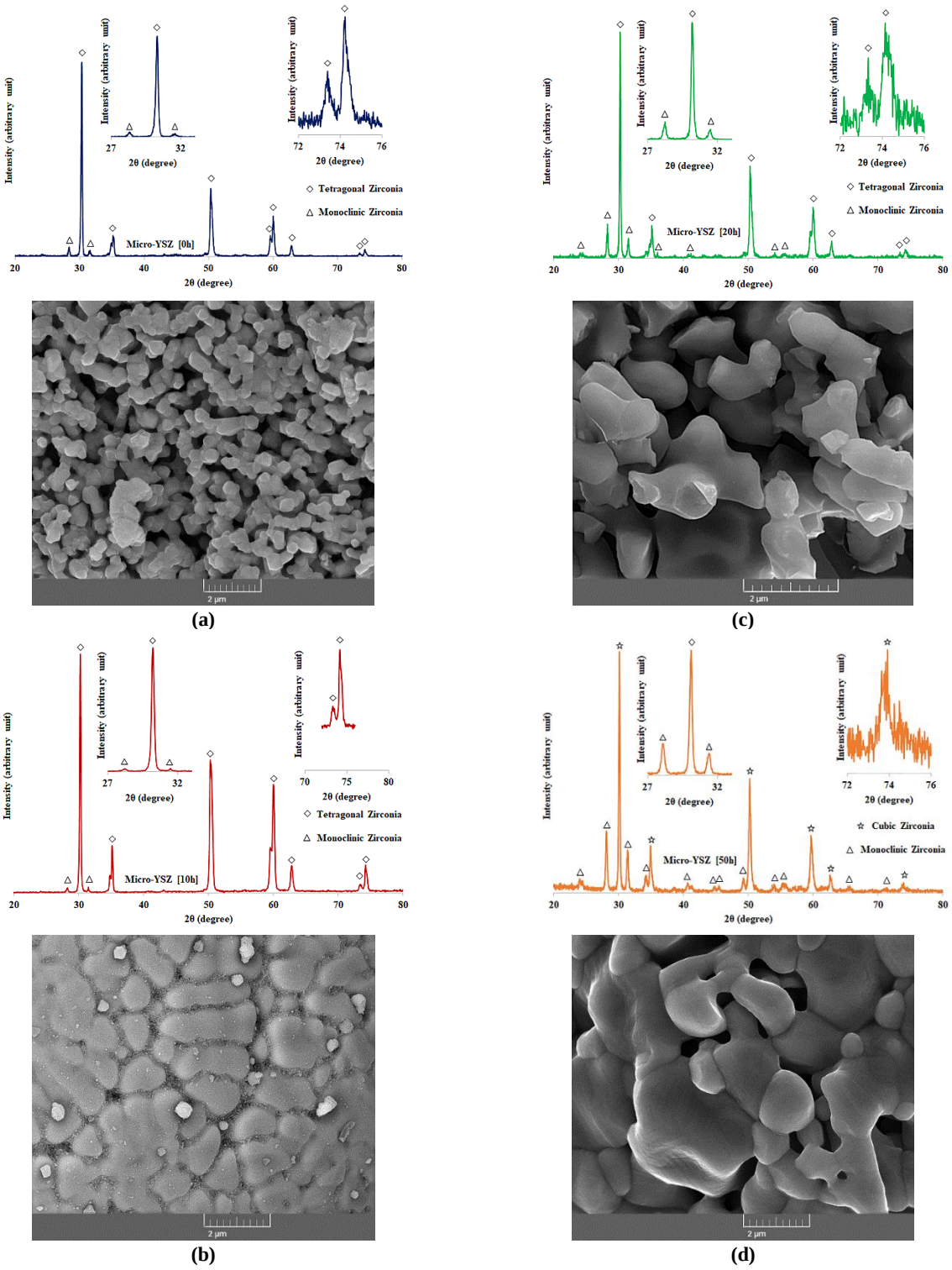

Figure 2. Results of XRD and FESEM analyses of the commercial micro-YSZ powder before and after heat treatment for (a) 0 h, (b) 10 h, (c) 20 h, and (d) 50 h at 1300 ºC

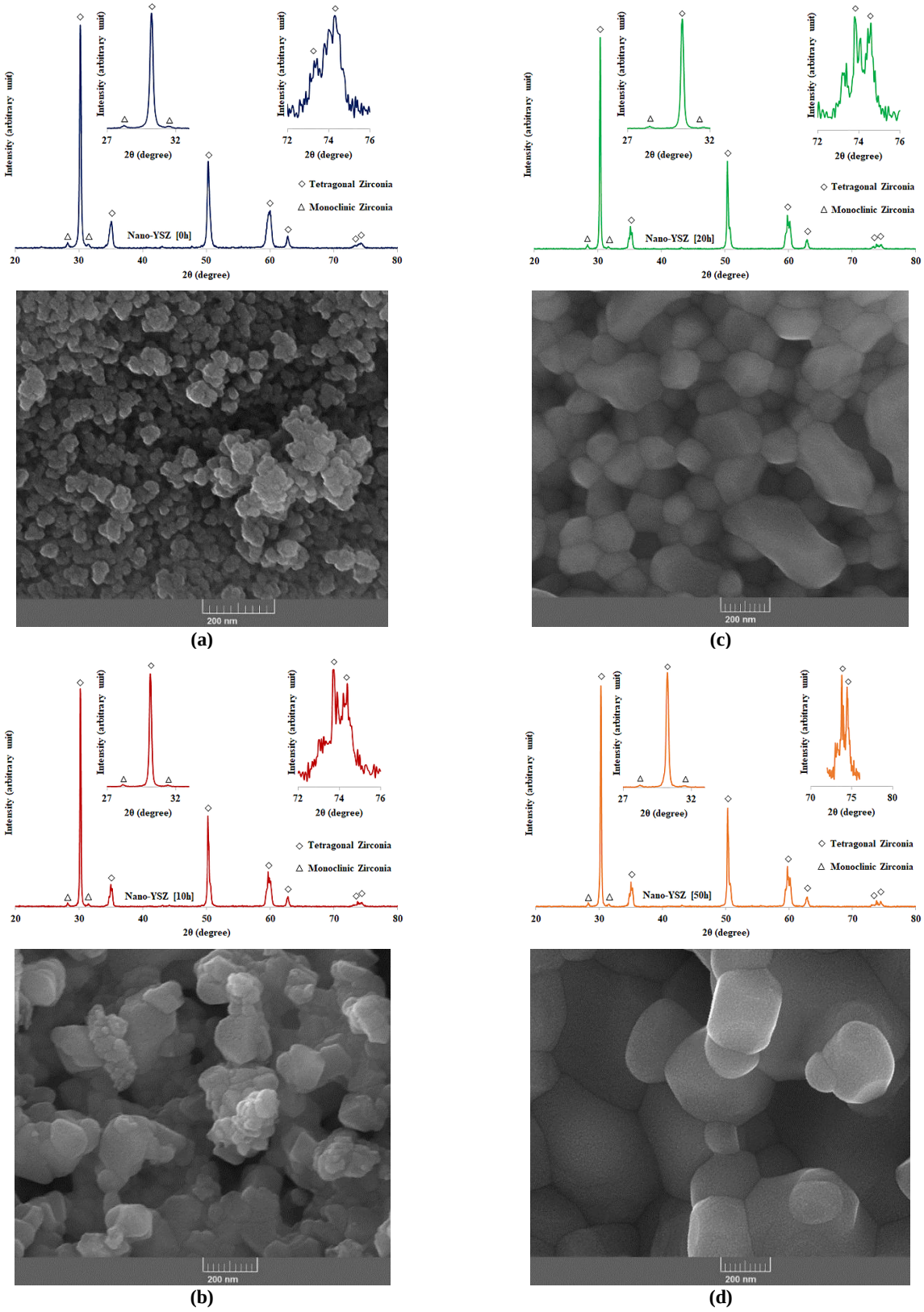

Figure 3. Results of XRD and FESEM analyses of the synthesized nano-YSZ powder before (calcinated at 1000 ºC for two hours) and after heat treatment for (a) 0 h, (b) 10 h, (c) 20 h, and (d) 50 h at 1300 ºC

For a better understanding of this phenomenon, the thermodynamic relations were also evaluated. In Equation (2), G shows the free energy of the spherical particles, r their diameter, γ the surface energy. Equation (3) was proposed to calculate the difference in the free energies of the tetragonal and monoclinic phases. Followed by computing the critical radius and differentiating Equation (3), we will have Equation (4) [31,34].

$$G = \frac{4}{3}\pi r^3 G_v + 4\pi r^2 \gamma \quad (2)$$

$$\Delta G(r) = \frac{4}{3}\pi r^3 \Delta G_v + 4\pi r^2 (\gamma_t - \gamma_m) \quad (3)$$

γ_t (tetragonal) = 0.77 Jm^{-2}

γ_m (monoclinic) = 1.13 Jm^{-2}

$$r^* = -2\frac{(\gamma_t - \gamma_m)}{\Delta H(1 - \frac{T}{T_b})} \quad (4)$$

where T_b = 1175 °C shows the transformation temperature of an infinite crystal and $\Delta H = 2.82 \times 10^8$ Jm^{-3} (all determined from calorimetry studies) represents the transformation heat per unit volume of an infinite crystal [31,34].

Based on Equations (2-4), the stability of the tetragonal or monoclinic phases of ZrO_2 at different temperatures depends on their particle sizes. Therefore, the probability of $t \longrightarrow m$ phase transformation will be incremented by increasing the temperature of the heat-treatment.

Figures 2 and 3 (a-d) depict the FESEM images of micro-YSZ and nano-YSZ after heat treatment at 1300 °C for 0, 10, 20, and 50 h. The growth of ZrO_2 particles due to the sintering and application of the thermal cycles can be observed in these images. A comparison of Figure 2 and Figure 3 confirmed the growth of particles due to heat treatment at high temperatures. It seems that followed by the heat treatment at high temperatures, grain rotation among the neighboring grains occurs, producing a coherent grain–grain interface associated with the disappearance of grain boundaries and consequently with the grain coalescence. This results in a change of grain orientation and formation of some equiaxed grains. Digimizer image analysis software was used to determine the average particle size of different powders (micro-YSZ and nano-YSZ) at different heat-treatment temperatures (Figure 4).

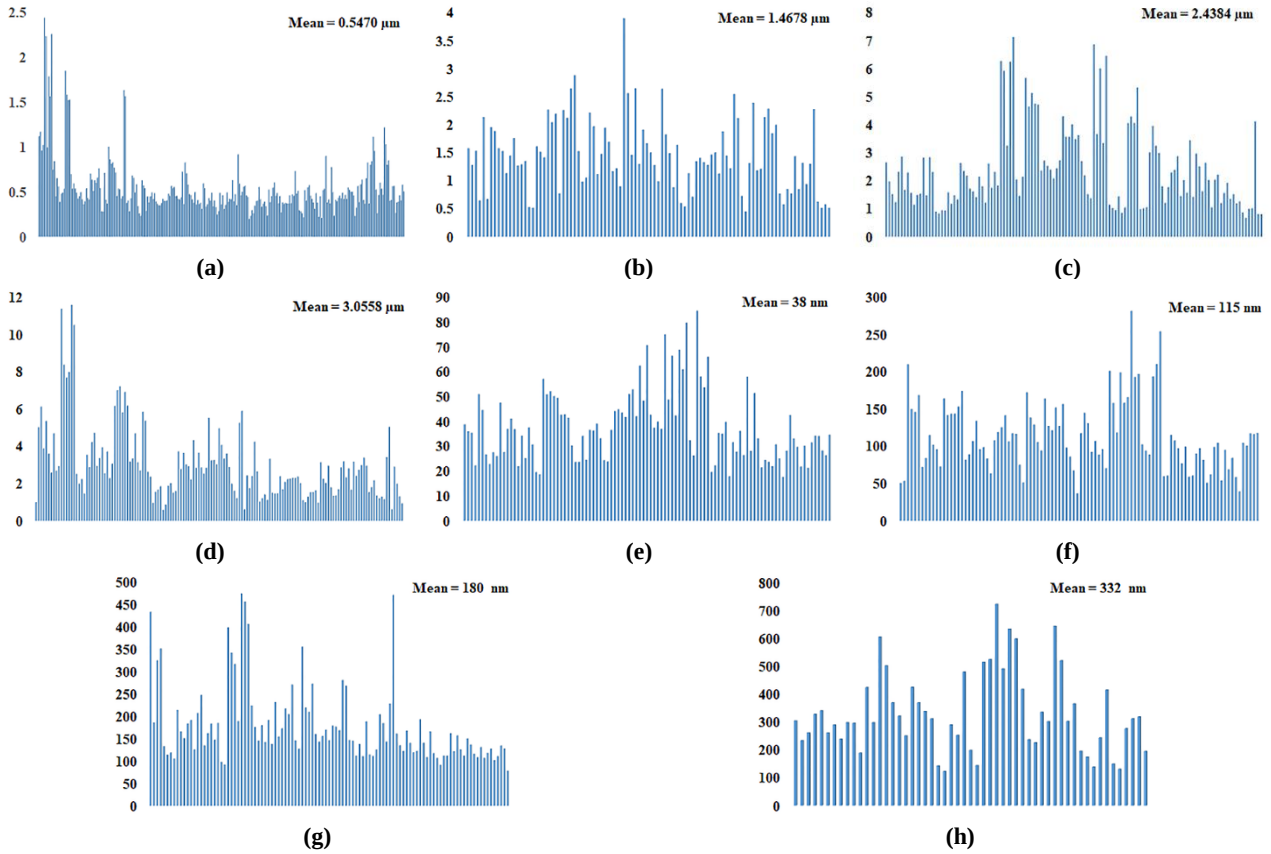

Figure 4. The average particle size of (a-d) micro-YSZ and (e-h) nano-YSZ powders at different heat-treatment temperatures

Upon extending the heat-treatment duration, the temporal variations in Full Width at Half Maximum (FWHM) parameter (Figure 5) predicts a decrease in the peak width and an increase in the particle growth rate. The FWHM variation trend in the nano-YSZ particle can be separated into two parts: in the first part (0-20 h) a steep slope is observed while in the second part (20-50 h) a linear trend is followed. It can be said that during the beginning stages of heat-treatment, the growth rate of the nano-YSZ particles was higher.

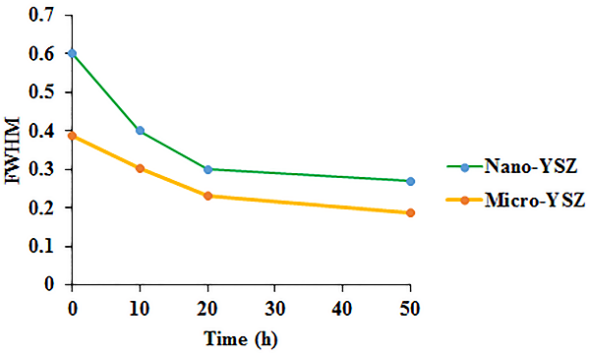

Figure 5. FWHM variation of micro- and nano-YSZ after heat-treatment at 1300 °C for 0, 10, 20, and 50 hours.

Based on the findings in this study, it can be concluded that nano-YSZ ceramic powder can be considered as a suitable candidate for potential TBC applications at ultra-high temperatures (higher than 1200 °C) owing to its improved phase stability, compares to that of micro-YSZ. However, additional research on the phase stability at longer exposure times is required to confirm this statement.

4. CONCLUSIONS

The main objective of the current study was to improve the functionality of the micro-YSZ in TBCs. Followed by synthesizing the nano-YSZ using precipitation methods and evaluating the phase stability of the samples at the working temperature of the new generation of gas turbines, the following conclusions were drawn (1300 °C):

- Based on the co-precipitation approach, nano-YSZ powder, including t'-phase, was successfully created at 1000 °C for two hours.
- The t-prime phase was not found in the heat-treated micro-YSZ after 50 hours of heat treatment at 1300 °C, indicating the instability of micro-YSZ at ultra-high temperatures.
- Investigation of the phase stability of nano-YSZ powders at 1300 °C revealed their high potential capabilities while applied to the new generation of TBCs.

ACKNOWLEDGEMENTS

The authors would like to express their gratitude to the honorable managing director of the "Barad Technology Co" (new technology-based firm, https://www.baradtechno.ir), Dr. Mahmoud Shahriari, and all of the personnel who work in the research and development department of the company.

REFERENCES

1. Rajendran, R., "Gas turbine coatings–an overview", ***Engineering Failure Analysis***, Vol. 26, (2012), 355-69. https://doi.org/10.1016/j.engfailanal.2012.07.007
2. Vaßen, R., Jarligo, M. O., Steinke, T., Mack, D. E., Stöver, D., "Overview on advanced thermal barrier coatings", ***Surface and Coatings Technology***, Vol. 205, No. 4, (2010), 938-942. https://doi.org/10.1016/j.surfcoat.2010.08.151
3. Cao, X. Q., Vassen, R., Stoever, D., "Ceramic materials for thermal barrier coatings", ***Journal of the European Ceramic Society***, Vol. 24, No. 1, (2004), 1-10. https://doi.org/10.1016/S0955-2219(03)00129-8
4. Bahamirian, M., Hadavi, S. M. M., Farvizi, M., Keyvani, A., Rahimipour, M. R., "Thermal durability of YSZ/nanostructured $Gd_2Zr_2O_7$ TBC undergoing thermal cycling", ***Oxidation of Metals***, Vol. 92, No. 5, (2019), 401-421. https://doi.org/10.1007/s11085-019-09937-7
5. Keyvani, A., Bahamirian, M., Kobayashi, A., "Effect of sintering rate on the porous microstructural, mechanical and thermomechanical properties of YSZ and CSZ TBC coatings undergoing thermal cycling", ***Journal of Alloys and Compounds***, Vol. 727, (2017), 1057-1066. https://doi.org/10.1016/j.jallcom.2017.08.184
6. Keyvani, A., Bahamirian, M., "Oxidation resistance of Al_2O_3-nanostructured/CSZ composite compared to conventional CSZ and YSZ thermal barrier coatings", ***Materials Research Express***, Vol. 3, No. 10, (2016), 105047. https://doi.org/10.1088/2053-1591/3/10/105047
7. Bahamirian, M., Hadavi, S. M. M., Farvizi, M., Rahimipour, M. R., Keyvani, A., "Enhancement of hot corrosion resistance of thermal barrier coatings by using nanostructured $Gd_2Zr_2O_7$ coating", ***Surface and Coatings Technology***, Vol. 360, (2019), 1-12. https://doi.org/10.1016/j.surfcoat.2018.12.113
8. Keyvani, A., Bahamirian, M., "Hot corrosion and mechanical properties of nanostructured Al_2O_3/CSZ composite TBCs", ***Surface Engineering***, Vol. 33, No. 6, (2017), 433-443. https://doi.org/10.1080/02670844.2016.1267423
9. Bahamirian, M., Khameneh Asl, S., "An investigation on effect of bond coat replacement on hot corrosion properties of thermal barrier coatings", ***Iranian Journal of Materials Science and Engineering***, Vol. 10, No. 3, (2013), 12-21. http://ijmse.iust.ac.ir/article-1-571-en.html
10. Padture, N. P., Gell, M., Jordan, E. H., "Thermal barrier coatings for gas-turbine engine applications", ***Science***, Vol. 296, No. 5566, (2002), 280-284. https://doi.org/10.1126/science.1068609
11. Keyvani, A., Mostafavi, N., Bahamirian, M., Sina, H., Rabiezadeh, A., "Synthesis and phase stability of zirconia-lanthania-ytterbia-yttria nanoparticles; a promising advanced TBC material", ***Journal of Asian Ceramic Societies***, Vol. 8, No. 2, (2020), 336-344. https://doi.org/10.1080/21870764.2020.1743419
12. Bahamirian, M., Hadavi, S. M. M., Farvizi, M., Rahimipour, M. R., Keyvani, A., "Phase stability of ZrO_2 $9.5Y_2O_3$ $5.6Yb_2O_3$ $5.2Gd_2O_3$ compound at 1100 °C and 1300 °C for advanced TBC

applications", ***Ceramics International***, Vol. 45, No. 6, (2019), 7344-7350. https://doi.org/10.1016/j.ceramint.2019.01.018

13. Xu, H., Wu, J., "15 - New materials, technologies and processes in thermal barrier coatings", In ***Thermal Barrier Coatings***, Woodhead Publishing, (2011), 317-328. https://doi.org/10.1533/9780857090829.3.317
14. Khor, K. A., Yang, J., "Lattice parameters, tetragonality (ca) and transformability of tetragonal zirconia phase in plasma-sprayed ZrO_2-Er_2O_3 coatings", ***Materials Letters***, Vol. 31, No. 1-2, (1997), 23-27. https://doi.org/10.1016/S0167-577X(96)00245-5
15. Pan, W., Phillpot, S. R, Wan, C., Chernatynskiy, A., Qu, Z., "Low thermal conductivity oxides", ***MRS Bulletin***, Vol. 37, No. 10, (2012), 917-922. https://doi.org/10.1557/mrs.2012.234
16. Basu, B., "Toughening of yttria-stabilised tetragonal zirconia ceramics", ***International Materials Reviews***, Vol. 50, No. 4, (2005), 239-256. https://doi.org/10.1179/174328005X41113
17. Hajizadeh-Oghaz, M., Shoja Razavi, R., Loghman-Estarki, M. R., "Synthesis and characterization of non-transformable tetragonal YSZ nanopowder by means of Pechini method for thermal barrier coatings (TBCs) applications", ***Journal of Sol-Gel Science and Technology***, Vol. 70, No. 1, (2014), 6-13. https://doi.org/10.1007/s10971-014-3266-z
18. Loghman-Estark, M. R., Razavi, R. S., Edris, H., "Synthesis and Thermal Stability of Nontransformable Tetragonal (ZrO_2) 0.96 ($REO_{1.5}$) 0.04 (Re= Sc^{3+}, Y^{3+}) Nanocrystals", In ***Defect and Diffusion Forum***, Trans Tech Publication Ltd., Vol. 334, (2013), 60-64. https://doi.org/10.4028/www.scientific.net/DDF.334-335.60
19. Zhou, F., Wang, Y., Wang, Y., Wang, L., Gou, J., Chen, W., "A promising non-transformable tetragonal YSZ nanostructured feedstocks for plasma spraying-physical vapor deposition", ***Ceramics International***, Vol. 44, No. 1, (2018), 1201-1204. https://doi.org/10.1016/j.ceramint.2017.10.012
20. Bahamirian, M., Hadavi, S. M. M., Farvizi, M., Keyvani, A., Rahimipour, M. R., "ZrO_2 9.5Y_2O_3 5.6Yb_2O_3 5.2Gd_2O_3; a promising TBC material with high resistance to hot corrosion", ***Journal of Asian Ceramic Societies***, Vol. 8, No. 3, (2020), 898-908. https://doi.org/10.1080/21870764.2020.1793474
21. Keyvani, A., Mahmoudinezhad, P., Jahangiri, A., Bahamirian, M., "Synthesis and characterization of (($La_{1-x}Gd_x)_2Zr_2O_7$; x= 0, 0.1, 0.2, 0.3, 0.4, 0.5, 1) nanoparticles for advanced TBCs", ***Journal of the Australian Ceramic Society***, Vol. 56, No. 4, (2020), 1543-1550. https://doi.org/10.1007/s41779-020-00500-1
22. Keyvani, A., Bahamirian, M., Esmaeili, B., "Sol-gel synthesis and characterization of ZrO_2-25wt.%CeO_2-2.5wt.%Y_2O_3 (CYSZ) nanoparticles", ***Ceramics International***, Vol. 46, No. 13, (2020), 21284-21291. https://doi.org/10.1016/j.ceramint.2020.05.219
23. Bahamirian, M., Hadavi, S. M. M., Rahimipour, M. R, Farvizi, M., Keyvani, A., "Synthesis and characterization of yttria-stabilized zirconia nanoparticles doped with ytterbium and gadolinium: ZrO_2 9.5 Y_2O_3 5.6 Yb_2O_3 5.2 Gd_2O_3", ***Metallurgical and Materials Transactions A***, Vol. 49, No. 6, (2018), 2523-2532. https://doi.org/10.1007/s11661-018-4555-x
24. Hajizadeh-Oghaz, M., Shoja Razavi, R., Ghasemi, A., "Synthesis and characterization of ceria–yttria co-stabilized zirconia (CYSZ) nanoparticles by sol–gel process for thermal barrier coatings (TBCs) applications", ***Journal of Sol-Gel Science and Technology***, Vol. 74, No. 3, (2015), 603-612. https://doi.org/10.1007/s10971-015-3639-y
25. Guo, L., Li, M., Ye, F., "Phase stability and thermal conductivity of RE_2O_3 (RE= La, Nd, Gd, Yb) and Yb_2O_3 co-doped Y_2O_3 stabilized ZrO_2 ceramics", ***Ceramics International***, Vol. 42, No. 6, (2016), 7360-7365. https://doi.org/10.1016/j.ceramint.2016.01.138
26. Li, Q. L., Cui, X. Z., Li, S. Q., Yang, W. H., Wang, C., Cao, Q., "Synthesis and phase stability of scandia, gadolinia, and ytterbia co-doped zirconia for thermal barrier coating application", ***Journal of Thermal Spray Technology***, Vol. 24, No. 1-2, (2015), 136-143. https://doi.org/10.1007/s11666-014-0158-2
27. Viazzi, C., Bonino, J. P., Ansart, F., Barnabé, A., "Structural study of metastable tetragonal YSZ powders produced via a sol–gel route", ***Journal of Alloys and Compounds***, Vol. 452, No. 2, (2008), 377-383. https://doi.org/10.1016/j.jallcom.2006.10.155
28. Sheu, T. S., Tien, T. Y., Chen, I. W., "Cubic-to-tetragonal (t') transformation in zirconia-containing systems", ***Journal of the American Ceramic Society***, Vol. 75, No. 5, (1992), 1108-1116. https://doi.org/10.1111/j.1151-2916.1992.tb05546.x
29. Srinivasan, R., De Angelis, R. J., Ice, G., Davis, B. H., "Identification of tetragonal and cubic structures of zirconia using synchrotron x-radiation source", ***Journal of Materials Research***, Vol. 6, No. 6, (1991), 1287-1292. https://doi.org/10.1557/JMR.1991.1287
30. Suresh, A., Mayo, M. J., Porter, W. D., Rawn, C. J., "Crystallite and grain-size-dependent phase transformations in yttria-doped zirconia", ***Journal of the American Ceramic Society***, Vol. 86, No. 2, (2003), 360-362. https://doi.org/10.1111/j.1151-2916.2003.tb00025.x
31. Chraska, T., King, A. H., Berndt, C. C., "On the size-dependent phase transformation in nanoparticulate zirconia", ***Materials Science and Engineering: A***, Vol. 286, No. 1, (2000), 169-178. https://doi.org/10.1016/S0921-5093(00)00625-0
32. Garvie, R. C., Goss, M. F., "Intrinsic size dependence of the phase transformation temperature in zirconia microcrystals", ***Journal of Materials Science***, Vol. 21, No. 4, (1986), 1253-1257. https://doi.org/10.1007/BF00553259
33. Garvie, R. C., "The occurrence of metastable tetragonal zirconia as a crystallite size effect", ***The Journal of Physical Chemistry***, Vol. 69, No. 4, (1965), 1238-1243. https://doi.org/10.1021/j100888a024
34. Shukla, S., Seal, S., "Mechanisms of room temperature metastable tetragonal phase stabilisation in zirconia", ***International Materials Reviews***, Vol. 50, No. 1, (2005), 45-64. https://doi.org/10.1179/174328005X14267

Advanced Ceramics Progress: Vol. 8, No. 2, (Spring 2022) 61-72

Materials and Energy Research Center
MERC

Contents lists available at ACERP

Advanced Ceramics Progress

Journal Homepage: www.acerp.ir

Original Research Article

Improvement of the Effective Parameters of 1-3 Piezocomposite Using Multi-Layer Polymer and PMN-PT Relaxor Single Crystal

Bentolhoda Amanat [a, *]

[a] *Assistant Professor, Department of Physics, Faculty of Sciences, Payame Noor University, Tehran, Tehran, Iran*

* Corresponding Author Email: amanat@pnu.ac.ir (B. Amanat)

URL: https://www.acerp.ir/article_159842.html

ARTICLE INFO

Article History:

Received 13 August 2022
Received in revised form 20 September 2022
Accepted 24 September 2022

Keywords:

1-3 Piezocomposite
Multi-Layer Polymer
Filling Fraction
Effective Parameter
PMN-PT

ABSTRACT

In this study, 1-3 piezocomposite with multi-layer polymer based on PZT piezoceramics and PMN-0.33PT relaxor single crystal was modeled and analyzed, and the obtained results were assessed. Recently, PMN-PT relaxor single crystals have been introduced as a suitable alternative to the PZTs due to their great piezoelectric coefficients. In addition, use of multi-layer polymers made from a combination of a polymer with a high stiffness coefficient for maintaining strength and a polymer with a much lower stiffness coefficient for increasing the electromechanical coupling coefficient improved the parameters of 1-3 piezocomposite. In addition, 1-3 piezocomposite with a multi-layer polymer based on PMT-PT increased the electromechanical coupling coefficient as well as the bandwidth of the filling fraction with the maximum value of k_t. This finding facilitated producing a piezocomposite at low filling fractions with very high k_t and very low characteristic acoustic impedance close to the characteristic impedance of the environment. It was shown that in the case where 75 % of the volume of the polymer phase was composed of silicone rubber, 1-3 piezocomposite with multi-layer polymer based on PMN-0.33PT single crystal could increase the electromechanical coupling coefficient to values greater than 0.95. In addition, in this case, it is possible to achieve a coupling coefficient of 0.94 and a characteristic impedance of 7 MRayl at the filling fraction of 0.2. The obtained results were analytically confirmed through the finite element numerical results.

https://doi.org/10.30501/acp.2022.355196.1099

1. INTRODUCTION

Piezoelectric materials are widely used in engineering sciences, materials, and smart structures [1,2]. The piezoelectric effect was first discovered by the Curie brothers in quartz [3,4]. A year later, in 1881, the converse piezoelectric effect was discovered by Lippmann [5]. Then, Newnham proposed the idea of polymer composites known as piezocomposite based on the PZT ceramics in 1978. Piezocomposite usually consists of two phases. The first phase is the active or piezoelectric phase while second phase is the inactive or the polymer phase with a specific connection mode, mass or volume ratio, and spatial geometric distribution [6]. In composites with two phases, 10 compounds are identified by two numbers [7].

One of the most widely used piezocomposites is 1-3 piezocomposite. High-performance 1-3 piezocomposites are widely utilized in high-frequency ultrasound transducers that are used for medical imaging [8-11]. Generally, 1-3 piezocomposite is preferred to the standard piezoceramics owing to its advantageous

Please cite this article as: Amanat, B., "Improvement of the Effective Parameters of 1-3 Piezocomposite Using Multi-Layer Polymer and PMN-PT Relaxor Single Crystal", ***Advanced Ceramics Progress***, Vol. 8, No. 2, (2022), 61-72. https://doi.org/10.30501/acp.2022.355196.1099

characteristics namely its low acoustic impedances, high electromechanical coupling coefficients, and high bandwidth [12-14]. However, compared to the bulk piezoceramics, piezocomposites components have some drawbacks such as their relatively high costs and limited operating temperature range [15,16]. The mentioned piezocomposite is commonly applied in Non-Destructive Testing (NDT) and sonar systems [17]. Yet, the biggest market for such materials is the medical diagnostic ultrasound market. Current medical ultrasound imaging systems cannot efficiently operate without application of 1-3 piezocomposite [18].

Owing to their beneficial features, they have been popular subjects of many research studies conducted to further improve the determining parameters in two ways: first, using materials with better piezoelectric properties in the piezocomposite structure and second, making changes in the structure and composition of the piezocomposite to facilitate the improvement of the electromechanical coupling coefficient parameters as much as possible so that the characteristic acoustic impedance (Z) of the piezocomposite would be close to the characteristic acoustic impedance of water (Z_{water} = 1.5 MRayl).

PZT ceramic is characterized by high electromechanical properties and advantages such as low cost and ease of production [19]. However, to overcome the problems caused by application of this material, a great deal of research has been conducted on how to replace the PZTs with more efficient materials with much better performance. In recent years, a new class of single-crystal piezoelectric materials called relaxor-based ferroelectric single crystals has received considerable attention mainly because these crystals, such as relaxor ferroelectric PMN-PT single crystals, have much higher and better piezoelectric properties than other ones such as quartz and piezoceramic materials (PZTs). Owing to their very high dielectric and piezoelectric constants, they have a very good electromechanical coupling coefficient, compared to the PZT piezoceramics. It is expected that 1-3 piezocomposites based on PMN-PT single crystal would have much better piezoelectric properties than those of their counterparts [18].

Efforts have been made to improve the electromechanical coupling coefficient by changing the structure of piezocomposites. In this regard, several researchers prepared a 1-3 piezocomposite by using other flexible polymers and attempted to enhance its electromechanical coupling coefficient [20,21]. According to the observations, the more flexible the polymer was, the more it succeeded in enhancing the electromechanical coupling of the composite [22]. However, high flexibility makes the composite susceptible to deformation [23,24]. A recent suitable solution to this problem is to use multi-layer piezocomposites.

Therefore, to increase the electromechanical coupling coefficient and decrease the characteristic acoustic impedance of 1-3 piezocomposite, the current study suggested application of relaxor ferroelectric PMN-0.33PT single crystals in a piezocomposite with a three-layer polymer structure. It is expected that using this relaxor single crystal in the structure of a 1-3 piezocomposite with a three-layer polymer will yield the desired results.

Different models have been designed to examine the effective properties of piezocomposites [25]. In this paper, some series and parallel theoretical models were used to determine the effective properties of three-layer piezocomposite [26,27]. Based on the results from the theoretical model and finite element numerical method, the behavior of electromechanical coupling coefficient and characteristic acoustic impedance of 1-3 piezocomposite were evaluated, and the obtained results were compared with each other. As observed, 1-3 piezocomposite with a three-layer polymer based on PMN-PT is characterized by a much better electromechanical coupling coefficient and acoustic impedance than the conventional 1-3 piezocomposites.

2. THEORETICAL FOUNDATIONS

1-3 Piezocomposite with a multi-layer polymer structure includes piezoceramic rods that are placed in a multi-layer polymer (one layer of polyethylene in the middle and two layers of silicone rubber at the top and bottom of piezocomposite). Figure 1 illustrates the structure of 1-3 piezocomposite with multi-layer polymer. In this model, the thickness direction of the piezocomposite is assumed to be in the z axis, and its transverse directions are assumed to be along the x and y axes. Piezoceramic columns are placed along the direction of the thickness of the piezocomposite. In the following, the relationships that clarify a piezoelectric material are presented [28].

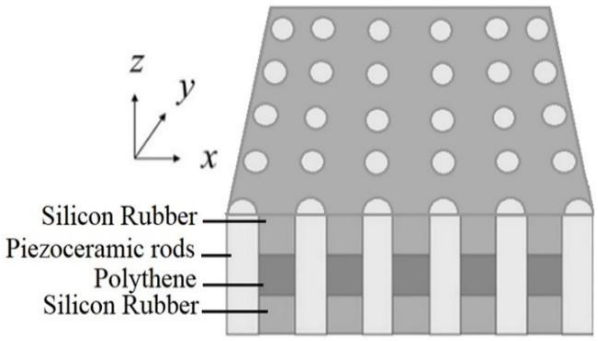

Figure 1. Schematic of 1-3 piezocomposite with three-layer polymer

$$\begin{cases} T_i = c_{ij}^D S_j + h_{ni} D_n \\ E_m = -h_{mj} S_j + \beta_{mn}^S D_n \end{cases} \quad (1)$$

where T is the mechanical stress tensor, S the mechanical strain tensor, D the electric charge displacement vector, E the electric field vector, c^D the elastic stiffness tensor in constant electric displacement, h the piezoelectric coefficient, and β^S the imprimitivity tensor in constant strain [29]. The polarization axis of the piezoelectric material is considered to be in the z axis. Of note, 1-3 piezocomposite can be considered as a homogeneous piezoelectric material with new effective parameters [30].

A series of assumptions based on uniform field theories as well as the rule of mixtures was taken into consideration to obtain the effective material parameters [31]. In the thickness mode, the lateral dimensions of the composite are sufficiently larger than the thickness one. According to the properties of the thickness mode, the piezocomposite was assumed to be parallel and symmetrical in the x and y axes, respectively.

Since it is quite difficult to obtain the relationship describing a piezocomposite using full field equations. Therefore, some simplifying approximations were used to obtain the essential physics. Given that the piezocomposite layers are in series on top of each other, due to the homogeneous displacement of the layers, the normal strains in the transverse directions of the piezocomposite are considered the same and equal to the effective strain for all three layers. In this regard, we assume that the strain and electric field in all piezocomposite plates that are placed on top of each other independent of x and y axes.

Therefore, shear strains and electric fields in the x and y axes can be ignored. In addition, the amount of electrical displacement of each layer and effective electrical displacement in transverse directions will be equal to zero. Since the polymers are connected in series, the vertical effective strain (S_3) of 1-3 piezocomposite with three-layer polymer along the thickness direction is equal to the weighted sum of the strains of all layers.

Moreover, the effective stress along the thickness direction in the piezocomposite is equal to the stress value along the thickness direction in each layer. The transverse effective stresses (T_1, T_2) will also be equal to the weighted sum of the transverse stresses of each layer.

The electrode surfaces are perpendicular to the z axis. Therefore, the effective electric field in the z direction, which is the same direction as the thickness one, is equal to the sum of the electric field in each layer of the piezocomposite with three layers of polymer. Due to the perpendicularity of the electrode surfaces to the z axis, the electric displacement in each layer of piezocomposite is the same and equal to the effective electric displacement of the piezocomposite along the thickness direction [32].

According to the mentioned assumptions, the relationships between the effective the electric field E_3, stresses T_1 and T_3 for each layer can be obtained as [33,34]:

$$\bar{S}_3 = -2\frac{\bar{c}_{13}^D}{\bar{c}_{33}^D}\bar{S}_1 + \frac{1}{\bar{c}_{33}^D}\bar{T}_3 + \frac{\bar{h}_{33}}{\bar{c}_{33}^D}\bar{D}_3 \quad (2)$$

$$\bar{T}_1 = \left(\bar{c}_{11}^D + \bar{c}_{12}^D - 2\frac{(\bar{c}_{13}^D)^2}{\bar{c}_{33}^D}\right)\bar{S}_1 + \frac{\bar{c}_{13}^D}{\bar{c}_{33}^D}\bar{T}_3 + \left(\bar{c}_{13}^D\frac{\bar{h}_{33}}{\bar{c}_{33}^D} - \bar{h}_{31}\right)\bar{D}_3 \quad (3)$$

$$\bar{E}_3 = (2\bar{h}_{33}\frac{\bar{c}_{13}^D}{\bar{c}_{33}^D} - 2\bar{h}_{31})\bar{S}_1 + \frac{-\bar{h}_{33}}{\bar{c}_{33}^D}\bar{T}_3 + \left(\bar{\beta}_{33}^s - \frac{(\bar{h}_{33})^2}{\bar{c}_{33}^D}\right)\bar{D}_3 \quad (4)$$

The sign ($\bar{}$) above each parameter indicates the effective value of that parameter in a layer. In addition, for the effective strain, effective stress, and effective electric field, we have [34]:

$$\bar{\bar{S}}_3 = v_1\bar{S}_3^1 + v_2\bar{S}_3^2 + v_3\bar{S}_3^3 \quad (5)$$

$$\bar{\bar{T}}_1 = v_1\bar{T}_1^1 + v_2\bar{T}_1^2 + v_3\bar{T}_1^3 \quad (6)$$

$$\bar{\bar{E}}_3 = v_1\bar{E}_3^1 + v_2\bar{E}_3^2 + v_3\bar{E}_3^3 \quad (7)$$

The sign ($\bar{\bar{}}$) above T, E, and S parameters indicates their effective value in 1-3 piezocomposite with a three-layer polymer. In addition, v_1, v_2, and v_3 are the volume fraction of the first, second, and third layers, respectively. Equations (2), (3), and (4) are substituted in Equations (5), (6), and (7) and then simplified.

According to the relationships related to the thickness mode in piezoelectric materials, the final relationships for 1-3 piezocomposite with three-layer polymer in thickness mode will be as follows [28]:

$$\begin{cases} \bar{\bar{T}}_3 = \bar{\bar{c}}_{33}^D\bar{\bar{S}}_3 - \bar{\bar{h}}_{33}\bar{\bar{D}}_3 \\ \bar{\bar{E}}_3 = -\bar{\bar{h}}_{33}\bar{\bar{S}}_3 + \bar{\bar{\beta}}_{33}^S\bar{\bar{D}}_3 \end{cases} \quad (8)$$

where both $\bar{\bar{c}}_{33}^D$, $\bar{\bar{h}}_{33}$ and $\bar{\bar{\beta}}_{33}^S$ are obtained according to the coefficients of the piezocomposite components.

For the thickness mode, the electromechanical coupling coefficient (k_t), characteristic acoustic impedance, and the longitudinal velocity are obtained in the following equations [28]:

$$k_t = \sqrt{\frac{\bar{\bar{h}}_{33}^2}{\bar{\bar{c}}_{33}^D}\bar{\bar{\epsilon}}_{33}^S} \quad (9)$$

$$c_t^D = \sqrt{\frac{\bar{\bar{c}}_{33}^D}{\bar{\bar{\rho}}}} \quad (10)$$

$$Z = \bar{\bar{\rho}}.\overline{\overline{c_t^D}} \quad (11)$$

where $(\bar{\bar{\rho}})$ is the effective density which is defined as:

$$\bar{\bar{\rho}} = v_c\rho_c + (1 - v_c)(v_e\rho_e + (1 - v_e)\rho_s) \quad (12)$$

In the above relationship, v_c is the volume fraction of piezoceramic in the 1-3 piezocomposite, and v_e the volume fraction of epoxy resin in the inactive or polymer phase of the piezocomposite. In addition, ρ_c, ρ_e, and ρ_s represent the density of the active phase of piezocomposite, density of epoxy resin, and density of silicone rubber, respectively.

3. SOLUTION METHOD AND HYPOTHESES

Here, consider a piezocomposite 1-3 consisting of three polymer layers, as shown in Figure 1. Table 1 lists the characteristics of the constituent polymer layers. In this research, PZT-4, PZT-8, and PMN-PT piezoceramics were used as the active piezoelectric phase, and their specifications are given in Table 2.

We define the V_{SR} parameter as:

$$V_{SR}\% = \frac{\text{Silicon Rubber volume} \times 100}{\text{Silicon Rubber volume} + \text{Polythene volume}}$$

As a result, the filling fraction of piezoelectric phase in piezocomposite as defined as:

$$\text{filling fraction of piezoelectric phase} = \frac{\text{volume of piezoelectric phase material}}{\text{volume of piezocomposite}}$$

Based on Equations (9), (10), and (11), the electromechanical coupling coefficient, longitudinal velocity, and characteristic impedance, respectively, were plotted for different V_{SR} (V_{SR} =0 %, 25 %, 50 %, and 75 %) as the functions of active piezoelectric phase filling fraction.

In these figures, the horizontal axis shows the filling fraction of the active piezoelectric phase, and the plot corresponding to V_{SR} =0 (shown by the solid line in all plots) refers to the simple 1-3 piezocomposite with monolayer polymer.

To confirm the results, the electromechanical coupling coefficient and characteristic acoustic impedance at several filling fractions (0.01, 0.1, 0.2, 0.3, 0.4, 0.5, 0.6, 0.7, and 0.8) for V_{SR} = 50 % were calculated using the finite element numerical method. Then, the numerical results were compared with the theoretical results. For this purpose, first, the piezocomposite electrical impedance was extracted as a function of frequency for the mentioned states.

TABLE 1. Specifications of polymers

Material parameters of the polymer		
Parameter	Polythene	Silicon Rubber
ρ (kg/)	1180	1150
c_{11}^E (GPa)	5.54	0.004
c_{12}^E (GPa)	2.98	0.0023
$\varepsilon_{11}^S(10^{-10})$	0.204	3.45

TABLE 2. Specifications of piezoceramics

Material parameters of the piezoelectric			
Parameter	PZT-8	PZT-4	PMN-0.33PT
ρ	7600	7500	8038
c_{11}^E (GPa)	149	139	115
c_{12}^E (GPa)	81.1	77.8	103
c_{13}^E (GPa)	81.1	74.3	102
c_{33}^E (GPa)	132	115	103.8
e_{31} (c/m^2)	-4.1	-5.2	-3.390
e_{33} (c/m^2)	14	15.1	20.4
$\varepsilon_{11}^S/\varepsilon_0$	900	730	1434
$\varepsilon_{33}^S/\varepsilon_0$	600	635	679

Figure 2 shows a schematic view of the electrical impedance curve as a function of frequency.

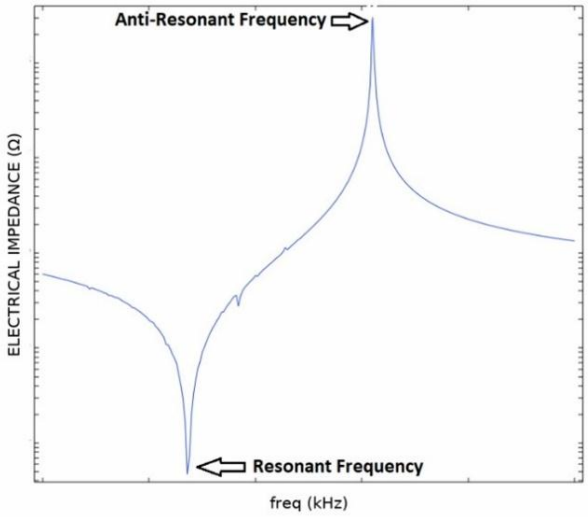

Figure 2. The electrical impedance of a piezoelectric material as a function of frequency

Based on this curve, the resonance and anti-resonance frequencies as well as the characteristic impedance and the electromechanical coupling coefficient were extracted through Equations (13) and (14) [34].

$$k_t = \sqrt{\frac{\pi f_s}{2f_p}\tan\frac{\pi(f_p - f_s)}{2f_p}} \quad (13)$$

$$Z = 2\bar{\rho}f_p t \quad (14)$$

where f_p is the anti-resonance frequency, f_s the resonance frequency, and t the thickness of the piezocomposite.

In practice, a network analyzer was employed to extract the electrical impedance diagram in terms of frequency. In addition, Relations (13) and (14) are used to calculate the electromechanical coupling coefficient and characteristic acoustic impedance.

3. RESULTS AND DISCUSSION

Figure 3 illustrates the variations of the electromechanical coupling coefficient for a 1-3 piezocomposite with a three-layer polymer based on PZT-8 piezoceramic at V_{SR} = 0 %, 25 %, 50 %, and 75 %. As observed in all four cases, V_{SR}, with an increase in the piezoelectric phase filling fraction from 0.1 to 0.3, the electromechanical coupling coefficient would rapidly increase. However, its value remains almost constant in a certain range (0.3 to 0.7) which is near to the maximum value of the electromechanical coupling coefficient. Next, with an increase in the filling fraction from 0.7 to 0.9, the coupling coefficient would rapidly decrease. The first point in this diagram is that upon increasing the value of V_{RS}, the value of k_t would consequently increase. As a result, the maximum value of k_t increases from 0.625 at V_{SR} =0 % to about 0.638 at V_{SR} =75 %, indicating an increase of 2 % in the maximum k_t value. Such an increase in the coupling coefficient results from using silicone rubber polymer, which is more flexible than polyethylene, as part of the inactive phase in the piezocomposite. The effective factor in this problem is the values of the elastic constant c_{11} in the polymer. The lower the value of this constant, the higher the electromechanical coupling coefficient.

According to the observations, with an increase in the V_{SR}, the electromechanical coupling coefficient reaches its maximum value in a larger range of the piezoceramic filling fraction; therefore, in the case of V_{SR}=0 %, the electromechanical coupling coefficient in the piezoceramic filling fraction range of 0.45 to 0.65 of the reaches its maximum value. In the case of V_{SR} =75 %, this range is from about 0.3 to 0.8, meaning that this range increased almost 2.5 times. Increasing the width of the filling fraction with the maximum k_t allows for more

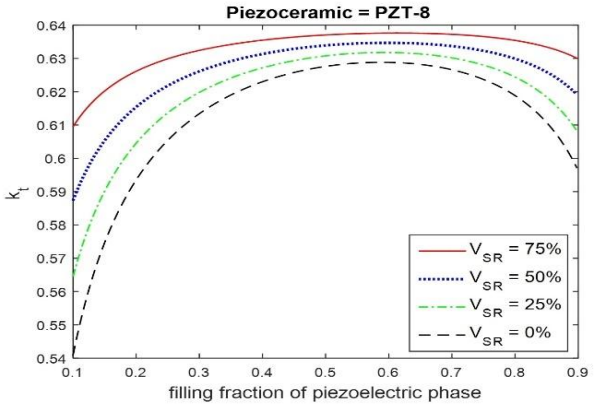

Figure 3. Variations in the electromechanical coupling factor for 1-3 piezocomposite with multi-layer polymer versus variations in the filling fraction of piezoceramic PZT-8 for different values of V_{SR}

freedom in determining other parameters such as the characteristic acoustic impedance. In fact, at V_{SR} =75 %, values near the maximum value of k_t are obtained in a larger range of filling fraction versus V_{SR} = 0 %.

In addition, at the filling fraction of 0.1 in V_{SR} =0 %, the value of k_t equals 0.54 while in V_{SR}=75 %, it equals 0.61. In other words, at the filling fraction of 0.1, the k_t value was improved up to about 13 %. Similarly, at the filling fractions of 0.9 and 0.5, there was about 5.5 % and 3 % increase in k_t, respectively.

Figure 4 shows the variations of the electromechanical coupling coefficient with the same conditions as before for 1-3 piezocomposite with a three-layer polymer based on piezoceramic PZT-4. Here, like the previous case, the electromechanical coupling coefficient increased with an increase in the value of V_{SR} at a constant filling fraction.

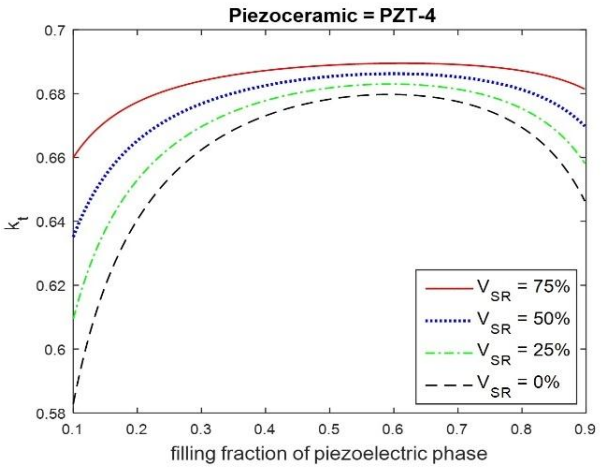

Figure 4. Variations in the electromechanical coupling factor for 1-3 piezocomposite with multi-layer polymer versus variations in the filling fraction of piezoceramic PZT-4 for different values of V_{SR}

Therefore, its maximum value of k_t from about 0.675 at V_{SR} =0 % increases up to about 0.69 at V_{SR}=75 %. That is, the k_t value increased up to about 2.2 % which a change in the V_{SR} from 0 % to 75 % at the filling fraction of 0.5. Such an increase in the k_t value by variation V_{SR} at the filling fractions 0.1 and 0.9 is about 14 % and 5 %, respectively.

Further, the bandwidth of the filling fraction where the value of k_t is constant at its maximum value considerably increased at V_{SR}=75 %, compared to that at V_{SR}=0 %.

Upon using PZT-4, the maximum value of k_t at the filling fraction of 0.5 and V_{SR}=75 % is equal to 0.688. This value shows an increase of about 8 % compared to that in the previous case where PZT-8 was used as the active phase. Such an increase occurs as a result of the higher value of k_t in PZT-4 than that of PZT-8.

Figure 5 shows the variations in the electromechanical coupling coefficient for 1-3 piezocomposite with a three-layer polymer based on PMN-0.33PT single crystal under the same conditions as before. In this figure, similar to Figures 3 and 4, the value of the coupling coefficient increases with an increase in the V_{SR} value from 0 % to 75 % at the constant filling fraction. The percentages of such increase at the volume fractions of about 0.5, 0.1, and 0.9 were 1.1 %, 16 %, and 8 %, respectively. This value is higher than that in the case where PZT-4 and PZT-8 were used as an active phase in the piezocomposite. On the contrary, the maximum value of k_t in this case was obtained as 0.95 at the filling fraction of 0.5 and V_{SR}=75 %, indicating a 38 % increase compared to the case where PZT-4 was used as the active phase. Such an increase in the maximum value of k_t results from the high electromechanical coupling coefficient of PMN-0.33PT single crystal. Apparently, use of PMN-0.33PT single crystal could significantly improve the electromechanical coupling coefficient.

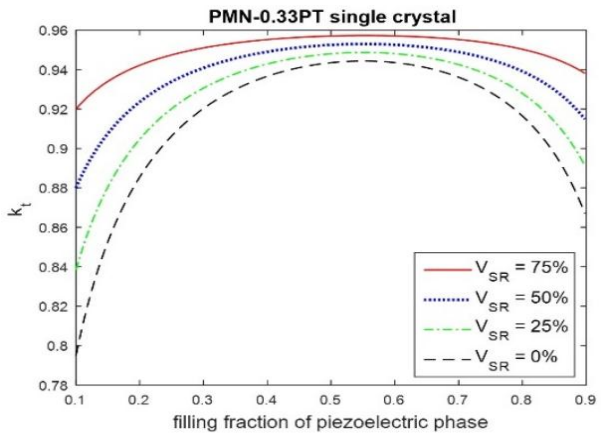

Figure 5. Variations in the electromechanical coupling factor for 1-3 piezocomposite with multi-layer polymer versus changes in the filling fraction of PMN-033PT single crystal for different values of V_{SR}

In the followingis examined the longitudinal velocity changes as a function of active phase filling fractions for 1-3 piezocomposite with a three-layer polymer for V_{SR} = 0 %, 25 %, 50 %, and 75 %.

Figure 6 shows the longitudinal velocity changes for 1-3 piezocomposite with three-layer polymer based on PZT-8. According to Figure 6, in general, the longitudinal velocity at V_{SR}=0 %, 25 %, 50 %, and 75 % starts to decrease with a slow slope as the filling fraction decreases by below 0.9. This trend continues until the filling fraction of 0.4 is reached; however, at the volume fraction values lower than 0.4, the decrease in the longitudinal velocity continues at higher rates. The effect of changing V_{SR} from 0 % to 75 % on the reduction of longitudinal velocity is much greater in the filling fractions close to 0.1 and 0.9. In this regard, at the filling fraction of 0.1 and V_{SR}=75 %, the longitudinal velocity is equal to 2800 m/s, showing a reduction of about 250 m/s compared to that in the case of V_{SR}=0 %. At the filling fraction of 0.9, the amount of such decrease is about 100 m/s. However, in the filling fraction range of 0.5 to 0.7, the longitudinal velocity does not change with variations in the V_{SR}, and these variations depend only on the changes in the piezoelectric active phase filling fraction.

Figure 7 shows the longitudinal velocity changes in 1-3 piezocomposite with a three-layer polymer based on PZT-4 as the function of piezoceramic filling fraction. The behavior of the longitudinal velocity changes in Figure 7 is similar to the changes in Figure 6. At the filling fractions of 0.1 and 0.9, the change in V_{SR} would cause a decrease in the longitudinal velocity by 220 m/s and 70 m/s, respectively, and in the filling fraction range of about 0.4 to 0.8, changes in V_{SR} do not have much effect on the longitudinal velocity. These changes result from the variations in the piezoceramic filling fraction.

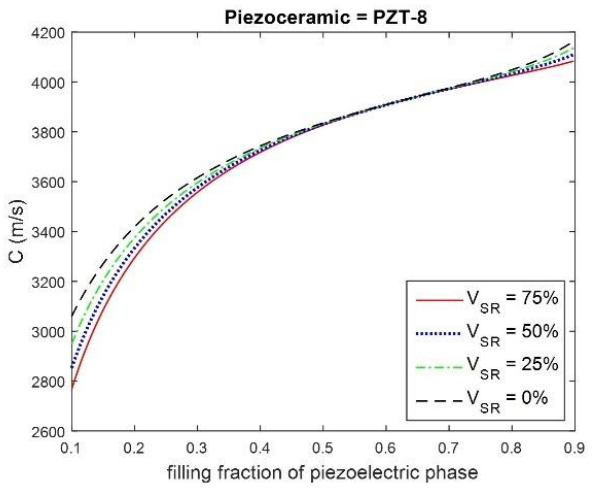

Figure 6. Variation of Longitudinal velocity for 1-3 piezocomposite with multi-layer polymer versus to changes in filling fraction of piezoceramic PZT-8 for different values of V_{SR}

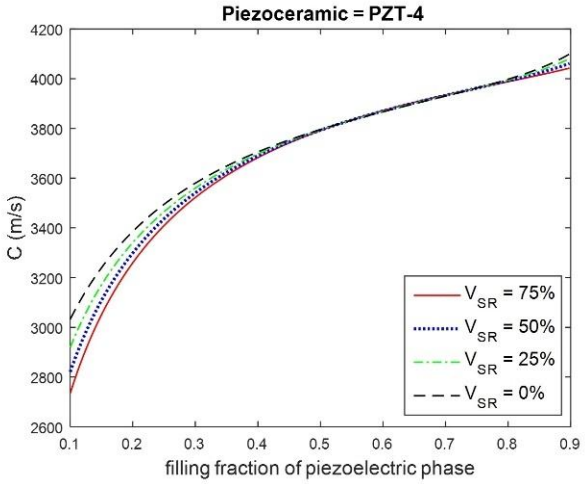

Figure 7. Variation of Longitudinal velocity for 1-3 piezocomposite with multi-layer polymer versus to changes in filling fraction of piezoceramic PZT-4 for different values of V_{SR}

As observed in Figures 6 and 7, at different volume fractions, the longitudinal velocity at V_{SR}=0 % is higher than those at V_{SR} = 25 %, 50 %, and 75 %. Yet, at the filling fraction of approximately 0.6, the longitudinal velocity at V_{SR}=0 % is slightly lower than those at other values of V_{SR}.

Figure 8 represents the longitudinal velocity changes in 1-3 piezocomposite with a three-layer polymer based on PMN-0.33PT as a function of filling fraction. The general behavior of this diagram is similar to those shown in Figures 6 and 7. With a reduction in the volume fraction value, the longitudinal velocity first decreases and then in the range of filling fractions of 0.6 to 0.4, it slightly decreases. In addition, at the volume fraction of 0.4, the longitudinal velocity begins to decrease with a relatively large slope.

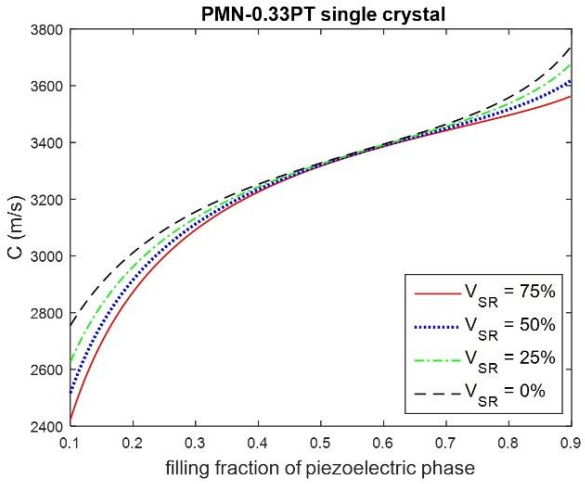

Figure 8. Variation of Longitudinal velocity for 1-3 piezocomposite with multi-layer polymer versus to changes in filling fraction of piezoceramic PMN-0.33PT for different values of V_{SR}

At the filling fraction of 0.1, the longitudinal velocity decreases from about 2750 m/s at V_{SR}=0 % to 2450 m/s at V_{SR}=75 %. At the filling fraction of 0.9, with a change in the value of V_{SR}, the longitudinal velocity decreases from about 3750 m/s at V_{SR}=0 % to 3550 m/s at V_{SR}=75 %. Therefore, the amount of longitudinal velocity changes in the filling fractions 0.1 and 0.9 are equal to 300m/s and 200m/s, respectively. In addition, as shown in Figure 8, in the volume fraction range of 0.6 to 0.5, the longitudinal velocity remains almost constant with a change in the V_{SR}; hence, the variations in the longitudinal velocity depend only on the variations in the filling fraction of the PMN-0.33PT. A comparison of Figures 6, 7, and 8 shows that compared to the case while PZT-4 and PZT-8 are applied, when PMN-0.33PT is used in the 1-3 piezocomposite with three-layer polymer, a reduction of at least 10 % is observed in the longitudinal velocity.

In the following, the changes in the characteristic acoustic impedance in 1-3 piezocomposite with multi-layer polymer is assessed based on piezoceramics PZT-4 and PZT-8 and PMN-0.33PT single crystal. Figure 9 shows the changes in the characteristic acoustic impedance of 1-3 piezocomposite with three-layer polymer based on piezoceramic PZT-8.

As observed in Figure 9, upon decreasing the piezoceramic filling fraction from 0.9 to 0.1, the characteristic acoustic impedance would also decrease, following an almost constant slope from about 28 MRayl to about 5 MRayl. This reduction is caused by a reduction in the piezoceramic filling fraction and effective density of the piezocomposite, as shown in Equation (12). In addition, increasing the amount of polymer by reducing the piezoceramic filling fraction also makes the

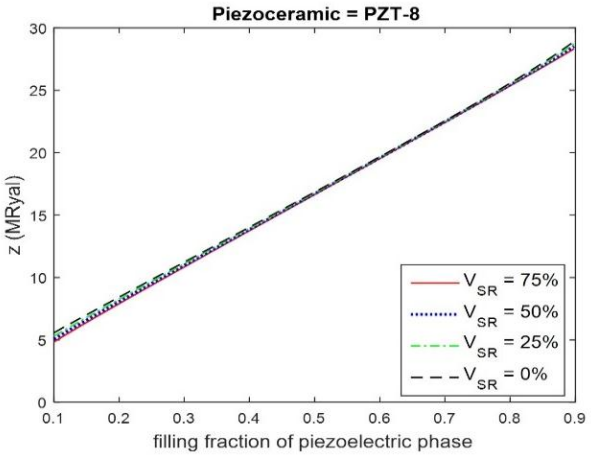

Figure 9. Variation of characteristic impedance for 1-3 piezocomposite with multi-layer polymer versus changes in the filling fraction of piezoceramic PZT-8 for different values of V_{SR}

piezocomposite softer than usual. As the V_{SR} value changed from 0 % to 75 %, a negligible decrease was observed in the characteristic impedance at a constant filling fraction, which was also caused by an increase in the proportion of silicone rubber.

Figure 10 depicts the diagram of the characteristic impedance changes for 1-3 piezocomposite with a three-layer polymer based on piezoceramic PZT-4. This diagram also exhibits a behavior similar to that observed in Figure 9. Upon decreasing the filling fraction in the range of 0.9 to 0.1, the characteristic acoustic impedance would also decrease almost linearly. Further, with a change in the V_{SR}, the value of the characteristic impedance decreased slowly due to an increase in the silicon rubber volume at a constant volume fraction of piezoceramic. Of note, at the filling fraction values close to 0.1, the effect of V_{SR} changes is relatively enormous, and as the volume fraction approaches 0.6, the number of changes in the characteristic impedance decreases. Then, as the filling fraction reaches the value close to 0.9, the amount of the characteristic impedance reduction would increase with an increases in the V_{SR}.

Figure 11 also shows the acoustic characteristic impedance variation for 1-3 piezocomposite with three-layer polymer based on single crystal PMN-0.33PT.

As observed in Figure 11, the acoustic characteristic impedance decreases almost linearly with a decrease in the filling fraction values. In addition, as a result of increasing V_{SR} at the constant filling fraction, the value of the characteristic impedance would slowly decrease. At the filling fraction values close to 0.9 and 0.1, such decrease is considerable.

The characteristic impedance of 1-3 piezocomposite with three-layer polymer based on PMN-0.33PT at the filling fraction of approximately 0.9 is lower than that of 1-3 piezocomposite with three-layer polymer based on PZT-4 and PZT-8, indicating the better performance of PMN-0.33PT than that of the others. For a better understanding of the difference in the characteristic acoustic impedance of 1-3 piezocomposite with a three-layer polymer based on PZT-8 and PZT-4 piezoceramics and PMN-0.33PT single crystal, Figure 12 makes a comparison of the characteristic impedance of these piezocomposites at V_{SR} =50 %. Apparently, in this figure, PMN-0.33PT single crystal outperforms the other two piezoceramics PZT-8 and PZT-4 in the three-layer 1-3 piezocomposite structure.

It should be noted that the three-layer polymer in 1-3 piezocomposite can significantly improve the characteristic impedance in practice. As previously

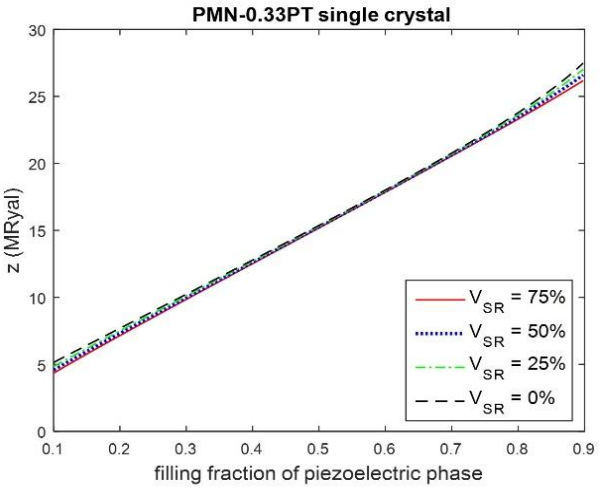

Figure 11. Variation of characteristic impedance for 1-3 piezocomposite with multi-layer polymer versus to changes in the filling fraction of piezoceramic PMN-0.33PT for different values of V_{SR}

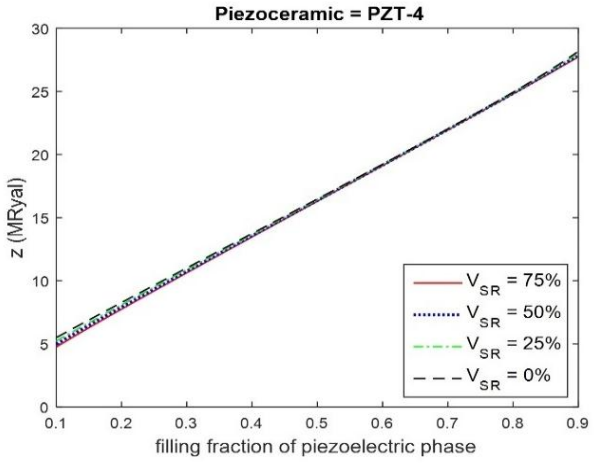

Figure 10. Variation of characteristic impedance for 1-3 piezocomposite with multi-layer polymer versus to changes in the filling fraction of piezoceramic PZT-4 for different values of V_{SR}

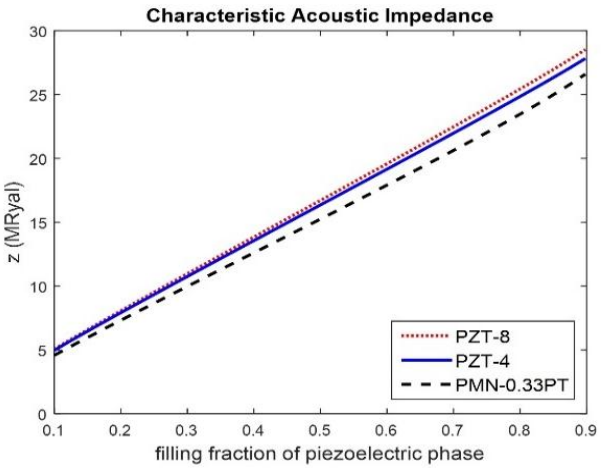

Figure 12. A comparison of the characteristic impedance of 1-3 piezocomposite with a three-layer polymer based on PZT-8 and PZT-4 piezoceramics and PMN-0.33PT single crystal at V_{SR} = 50 %

mentioned in the electromechanical coupling coefficient discussion, an increase in the V_{SR} value from 0 % to 75 % would increase the bandwidth of the filling fraction with a constant k_t value (in this filling fraction bandwidth, k_t is almost constant close to its maximum value).

This finding helps us obtain the maximum value of k_t at lower filling fractions. In other words, by reducing the filling fraction, we can obtain the highest value of k_t in lower characteristic acoustic impedances.

Next, to confirm the results obtained from the analytical method through the finite element numerical method for 1-3 piezocomposite with three-layer polymer based on piezoceramics PZT-4, PZT-8 and PMN-0.33PT single crystal at V_{SR} = 50 %, the electromechanical coupling coefficient and characteristic acoustic impedance at the filling fraction values of 0.01, 0.1, 0.2, 0.3, 0.4, 0.5, 0.6, 0.7, and 0.8 were calculated. Then, the results were compared with the graphs illustrated based on the analytical method.

Table 3 presents the results of 1-3 piezocomposite with a three-layer polymer based on PMN-0.33PT. Figure 13 shows the values for the electromechanical coupling coefficient through both analytical and numerical methods. As observed, the results obtained from the two methods agree with each other with a very good approximation.

Figure 14 represents the characteristic impedance values for 1-3 piezocomposite with three-layer polymer obtained from two analytical and numerical methods based on PMN-0.33PT single crystal at V_{SR} = 50 % for volume fractions of 0.01, 0.1, 0.2, 0.3, 0.4, 0.5, 0.6, 0.7, and 0.8. As observed, these results are also in good agreement with each other.

Next, the same operation was repeated on 1-3 piezocomposite with a three-layer polymer based on PZT-8 and PZT-4 piezoceramics. Tables 4 and 5 elaborate the results for 1-3 piezocomposite with a three-layer polymer based on PZT-8 and PZT-4. Figures 15 and 16 show the electromechanical coupling coefficient through the analytical and numerical methods.

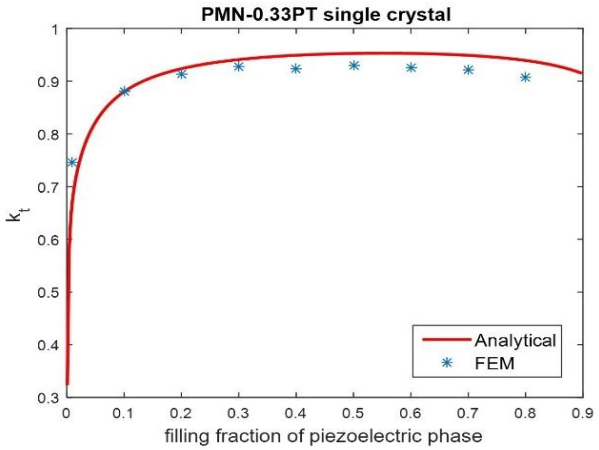

Figure 13. The electromechanical coupling coefficient obtained from two analytical and numerical methods for 1-3 piezocomposite with three-layer polymer based on PMN-0.33PT at V_{SR} = 50 %

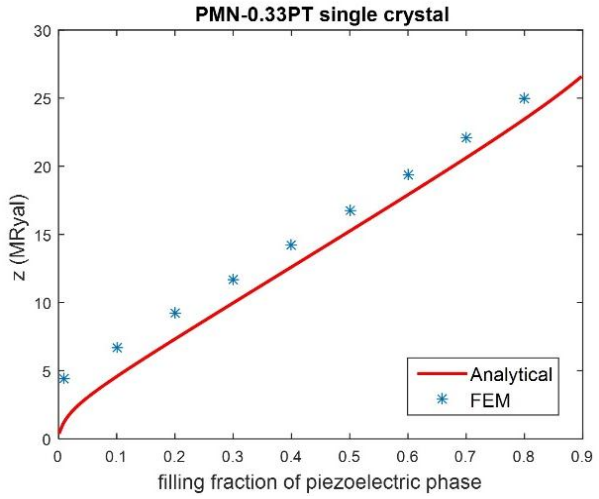

Figure 14. The characteristic impedance values obtained from two analytical and numerical methods for 1-3 piezocomposite with three-layer polymer based on PMN-0.33PT at V_{SR} = 50 %

TABLE 3. Numerical results for 1-3 piezocomposite with a three-layer polymer based on PMN-0.33PT

Filling Fraction	f_p (Hz)	f_s (Hz)	k_t	Z (Rayl)
0.8	374000	170000	0.907743	24957020
0.7	370000	156000	0.921592	22124150
0.6	367300	150400	0.926357	19415478
0.5	365000	147000	0.928922	16762625
0.4	363700	151300	0.923819	14180663
0.3	364600	148600	0.927088	11687253
0.2	366500	161200	0.914103	9206480
0.1	370000	189000	0.880671	6728450
0.01	403000	283000	0.746441	4374364

TABLE 4. Numerical results for 1-3 piezocomposite with a three-layer polymer based on PZT-8

Filling Fraction	f_p (Hz)	f_s (Hz)	k_t	Z (Rayl)
0.8	419000	342000	0.617043632	26334150
0.7	421000	341000	0.62567158	23691775
0.6	419000	337000	0.633319626	20824300
0.5	417000	337000	0.628145088	17983125
0.4	415000	335000	0.6293927	15168250
0.3	414000	335000	0.626756067	12409650
0.2	413000	337000	0.617390806	9664200
0.1	410000	341000	0.594675678	6898250
0.01	420000	393000	0.385912266	4581150

TABLE 5. Numerical results for 1-3 piezocomposite with a three-layer polymer based on PZT-4

Filling Fraction	f_p (Hz)	f_s (Hz)	k_t	Z (Rayl)
0.8	410000	324000	0.651509719	25440500
0.7	411000	324000	0.653921791	22841325
0.6	409000	319000	0.664217888	20081900
0.5	403000	318350	0.651879111	17177875
0.4	406000	318000	0.660197414	14676900
0.3	405000	318000	0.65781786	12018375
0.2	405000	321000	0.648538844	9396000
0.1	403000	328100	0.619945805	6740175
0.01	417000	380000	0.448114453	4647465

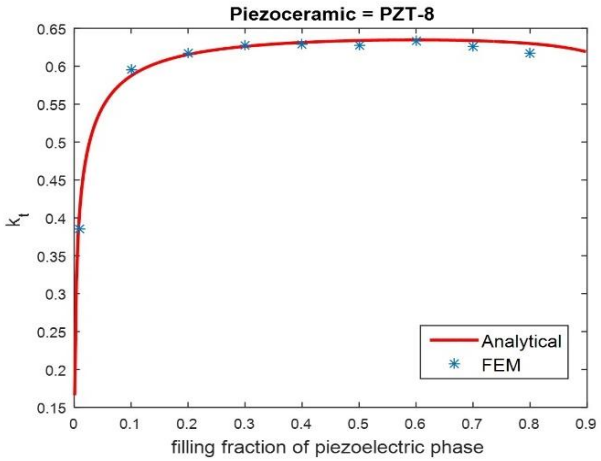

Figure 15. The electromechanical coupling coefficient obtained from two analytical and numerical methods for 1-3 piezocomposite with three-layer polymer based on PZT-8 at V_{SR} = 50 %

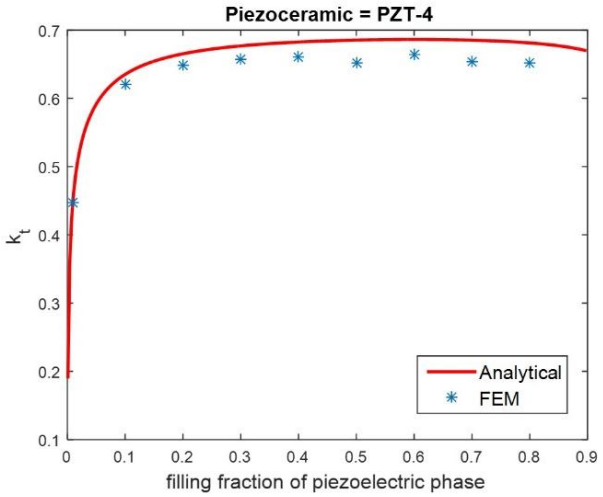

Figure 16. The electromechanical coupling coefficient obtained from two analytical and numerical methods for 1-3 piezocomposite with three-layer polymer based on PZT-4 at V_{SR} = 50 %

As observed in both piezocomposites, the results were consistent with each other for the piezocomposite based on PZT-4 and PZT-8.

Figures 17 and 18 also list the values for characteristic acoustic impedance through the numerical and analytical methods, respectively, for piezocomposite based on PZT-8 and PZT-4. In this case, the obtained results also agreed with each other.

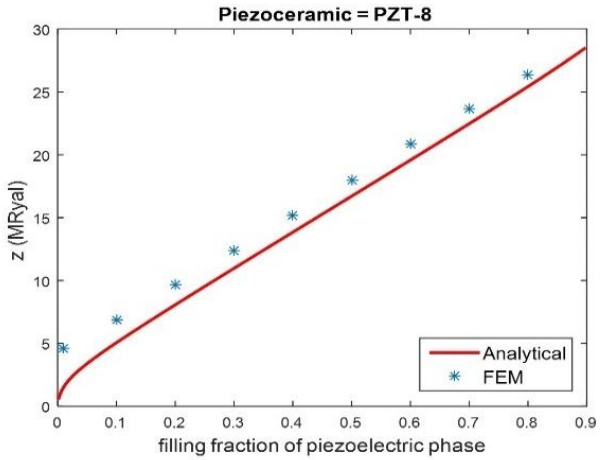

Figure 17. The characteristic impedance values obtained from two analytical and numerical methods for 1-3 piezocomposite with three-layer polymer based on PZT-8 at V_{SR} = 50%

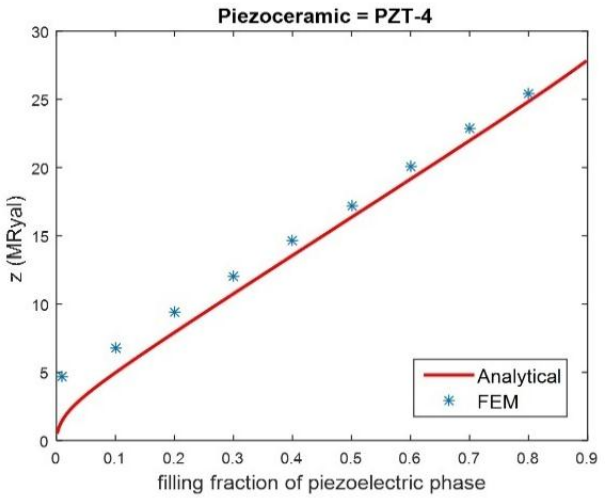

Figure 18. The characteristic impedance values obtained from two analytical and numerical methods for 1-3 piezocomposite with three-layer polymer based on PZT-4 at V_{SR} = 50 %

4. CONCLUSION

The current research aimed to produce 1-3 piezocomposite with a three-layer polymer, in which the polymer played the role of the inactive phase, and the

piezoceramic rods the role of the active phase. To obtain the parameters of the effective materials, a series of assumptions based on uniform field theories and rule of mixtures as well as the proposed relations were used to obtain the values of the electromechanical coupling coefficient, longitudinal velocity, and characteristic impedance, in terms of the coefficients of the components of the piezocomposite. In this study, 1-3 piezocomposite with a three-layer polymer was used where the middle layer is polyethylene while the other two layers are a polymer like silicone rubber, characterized by a lower stiffness coefficient (c_{11}) than that of polyethylene. Upon increasing the volume of silicone rubber, compared to that of polyethylene, the electromechanical coupling coefficient would increase while the values for longitudinal velocity and characteristic acoustic impedance of the piezocomposite would decrease. Such an increase in the volume would in turn increased the bandwidth of the filling fraction, and k_t reached its maximum value. As a result, a freedom of action was given to determine the appropriate characteristic acoustic impedance at the maximum k_t value, thus making it possible to bring the characteristic acoustic impedance as close as possible to the environment's one by reducing the filling fraction without reducing the k_t value. However, given the very good piezoelectric properties of PMN-PT single crystals, upon using these single crystals instead of PZT piezoceramics, the coupling coefficient values in piezocomposites with multi-layer polymers increased up to more than 0.95 mainly due to the higher value of the k_t coefficient and their lower stiffness coefficient (c_{11}) than those of PZT piezoceramic materials. These single crystals, due to their low stiffness coefficient (c_{11}), are characterized by much lower longitudinal velocity and characteristic impedance than those of the piezoceramics. In addition, it was observed that the degree of improvement in the piezocomposite functional parameters, including electromechanical coupling coefficient, longitudinal velocity, and characteristic impedance, was greater at low and high filling fractions (less than 0.4 and more than 0.7) than usual, indicating that implementation of this structure can be a suitable solution to improving the performance of 1-3 piezocomposite at the filling fraction values of less than 0.4 and more than 0.7. To confirm the analytical results, the values obtained from the theoretical method and finite element numerical method were compared with each other, and it was found that they were in good agreement.

ACKNOWLEDGEMENTS

The authors wish to acknowledge Payame Noor University for the all support throughout this work.

NOMENCLATURE

T	Mechanical stress tensor
S	Electric charge vector
D	Electric charge vector
E	Electric field vector
c^D	Elastic stiffness tensor in constant electrical displacement
h	Piezoelectric coefficient
β^S	Constant strain incompressibility tensor
k_t	Electromechanical coupling coefficient
ρ	Density
Z	Characteristic acoustic impedance

REFERENCES

1. Mishra, A. K., Priya, V. J. K., Pradeep, K., Vaishnav, J. S., Kabhilesh, G., "Smart materials for ultrasonic piezoelectric composite transducer: A short review", ***Materials Today: Proceedings***, Vol. 62, No. 4, (2022), 2064–2069. https://doi.org/10.1016/j.matpr.2022.02.514
2. Kamel, N. A., "Bio-piezoelectricity: fundamentals and applications in tissue engineering and regenerative medicine", ***Biophysical Reviews***, Vol. 14, No. 3, (2022), 717–733. https://doi.org/10.1007/s12551-022-00969-z
3. Cheng, L. C., Brahma, S., Huang, J. L., , Liu, C. P., "Enhanced piezoelectric coefficient and the piezoelectric nanogenerator output performance in Y-doped ZnO thin films", ***Materials Science in Semiconductor Processing***, Vol. 146, (2022), 106703. https://doi.org/10.1016/j.mssp.2022.106703
4. Akhtar, M., Raza, S., and Hasan, S., "Green Energy Harvesting from Speed Breakers using Piezoelectric Materials", ***International Journal of Research in Engineering and Science (IJRES)***, Vol. 9, No. 2, (2021), 11–16. https://ijres.org/papers/Volume-9/Issue-2/C09021116.pdf
5. Pradeesh, E. L., Udhayakumar, S., Vasundhara, M. G., Kalavathi, G. K., "A review on piezoelectric energy harvesting", ***Microsystem Technologies***, Vol. 28, No. 8, (2022), 1797–1830. https://doi.org/10.1007/s00542-022-05334-4
6. Mha, P. T., Maréchal, P., Ntamack, G. E., d'Ouazzane, S. C., "Homogenized electromechanical coefficients and effective parameters of 1–3 piezocomposites for ultrasound imaging transducers", ***Physics Letters A***, Vol. 408, (2021), 127492. https://doi.org/10.1016/j.physleta.2021.127492
7. Uchino, K., "9 - Piezoelectric composite materials", In ***Advanced Piezoelectric Materials: Science and Technology***, Woodhead Publishing, Cambridge, UK, (2010), 318–346. https://doi.org/10.1533/9781845699758.1.318
8. Li, X., Tian, J., Yan, D., Tao, C., Zhou, J., Su, Y., "Soft Mold Process for 1-3 Piezocomposite and Its Application in High Frequency Medical Ultrasound Imaging", In ***2021 IEEE International Ultrasonics Symposium (IUS)***, IEEE, (2021), 1–4. https://doi.org/10.1109/IUS52206.2021.9593444
9. Chen, D., Hou, C., Fei, C., Li, D., Lin, P., Chen, J., Yang, Y., "An optimization design strategy of 1–3 piezocomposite ultrasonic transducer for imaging applications", ***Materials Today Communications***, Vol. 24, (2020), 100991. https://doi.org/10.1016/j.mtcomm.2020.100991
10. Tian, J., Li, X., Liang, Z., Ding, W., Li, X., Tao, C., Nie, S., "Fabrication of 1–3 piezoelectric composites via modified soft mold process for 40 MHz ultrasonic medical transducers", ***Ceramics International***, Vol. 48, No. 3, (2022), 3841–3848. https://doi.org/10.1016/j.ceramint.2021.10.168
11. Lin, P., Zhu, Y., Chen, Z., Fei, C., Chen, D., Zhang, S., Li, D., Feng, W., Yang, Y., Chai, C., "Design and fabrication of non-periodic 1–3 composite structure for ultrasonic transducer application", ***Composite Structures***, Vol. 285, (2022), 115249.

https://doi.org/10.1016/j.compstruct.2022.115249

12. Wang, J., Zhong, C., Hao, S., Wang, L., "Design and Properties Analysis of Novel Modified 1-3 Piezoelectric Composite", ***Materials***, Vol. 14, No. 7, (2021). https://doi.org/10.3390/ma14071749
13. Zhong, C., Xu, J., Hao, S., Zhang, Y., Wang, L., Qin, L. "High-frequency wide beam underwater transducer based on 1–3 piezocomposite", ***Ferroelectrics Letters Section***, Vol. 48, No. 4–6, (2021), 93-103. https://doi.org/10.1080/07315171.2021.1971009
14. Wu, Q., Chen, Q., Lian, G., Wang, X., Song, X., Zhang, X., "Investigation of an air-coupled transducer with a closed-cell material matching strategy and an optimization design considering the electrical input impedance", ***Ultrasonics***, Vol. 115, (2021), 106477. https://doi.org/10.1016/j.ultras.2021.106477
15. Li, Z., Lv, J., Zhu, X., Cui, Y., Jian, X., "Development of high frequency piezocomposite with hexagonal pillars via cold ablation process", ***Ultrasonics***, Vol. 114, (2021), 106404. https://doi.org/10.1016/j.ultras.2021.106404
16. Li, F., Chen, C., Li, W., Zeng, D.,"The electro-acoustic output behavior and thermal stability of 1–3 piezoelectric composite transducers applied to FUS surgery", ***Journal of Materials Science: Materials in Electronics***, Vol. 31, No. 15, (2020), 12066–12073. https://doi.org/10.1007/s10854-020-03735-7
17. Kim, T., Cui, Z., Chang, W. Y., Kim, H., Zhu, Y., Jiang, X., "Flexible 1–3 Composite Ultrasound Transducers with Silver-Nanowire-Based Stretchable Electrodes", In ***IEEE Transactions on Industrial Electronics***, Vol. 67, No. 8, (2020), 6955-6962. https://doi.org/10.1109/TIE.2019.2937063
18. Lv, J., Xie, X., Zhu, X., Li, Z., Han, Z., Cui, Y., Zhang, B., Jian, X., "Cold ablated high frequency PMN-PT/Epoxy 1-3 composite transducer", ***Applied Acoustics***, Vol. 188, (2022), 108540. https://doi.org/10.1016/j.apacoust.2021.108540
19. Kasaeipoor Naeini, P., Delshad Chermahin, M., Shayegh Boroujeny, B., Ebadzadeh, T., Nilforoushan, M., Abdollahi, M., "Study of Dielectric Properties of Lead-Free Multiferroic KNN/22.5 $BaFe_{12}O_{19}$ Composites", ***Advanced Ceramics Progress***, Vol. 7, No. 3, (2021), 23–28. https://doi.org/10.30501/acp.2021.298611.1071
20. Xu, J., Wang, L., Zhong, C., "The effect of thickness on properties of three-phase piezocomposites", In ***IOP Conference Series: Earth and Environmental Science***, Vol. 446, No. 2, (2020), 022008. https://doi.org/10.1088/1755-1315/446/2/022008
21. Zhong, C., Wang, L., Qin, L., Zhang, Y., "Characterization of an Improved 1-3 Piezoelectric Composite by Simulation and Experiment", ***Journal of Applied Biomaterials & Functional Materials***, Vol. 15 (1_suppl), (2017), 38-44. https://doi.org/10.5301/jabfm.500036
22. Jae Lee, H., Zhang, S., Meyer Jr, R. J., Sherlock, N. P., Shrout, T. R., "Characterization of piezoelectric ceramics and 1-3 composites for high power transducers", ***Applied Physics Letters***, Vol. 101, No. 3, (2012), 032902. https://doi.org/10.1063/1.4737651
23. Cheng, K. C., Chan, H. L. W., Choy, C. L., Yin, Q., Luo, H., Yin, Z., "Single crystal PMN-0.33PT/epoxy 1-3 composites for ultrasonic transducer applications", In ***IEEE Transactions on Ultrasonics Ferroelectrics and Frequency Control***, Vol. 50, No. 9, (2003), 1177-1183. https://doi.org/10.1109/TUFFC.2003.1235328
24. Zhang, H., Wei, Z., Fan, L., Qu, J., Zhang, S., "Tunable sound transmission at an impedance-mismatched fluidic interface assisted by a composite waveguide", ***Scientific Reports***, Vol. 6, No. 1, (2016), 34688. https://doi.org/10.1038/srep34688
25. Singh, S. K., Panda, S. K., "A comparative study of micromechanics models to evaluate effective coefficients of 1-3 piezoelectric composite", ***Mechanics of Advanced Materials and Structures***, (2022), 1–14. https://doi.org/10.1080/15376494.2022.2092799
26. Sakthivel, M., Arockiarajan, A., "An analytical model for predicting thermo-electro-mechanical response of 1–3 piezoelectric composites", ***Computational Materials Science***, Vol. 48, No. 4, (2010), 759–767. https://doi.org/10.1016/j.commatsci.2010.03.027
27. Prasath, S. S., Arockiarajan, A., "Effective electromechanical response of macro-fiber composite (MFC): Analytical and numerical models", ***International Journal of Mechanical Sciences***, Vol. 77, (2013), 98–106. https://doi.org/10.1016/j.ijmecsci.2013.09.031
28. Wilson, O. B., ***Introduction to the Theory and Design of Sonar Transducers***, Peninsula Pub, (1989).
29. Yang, J., ***Mechanics of Piezoelectric Structures***, 2nd Ed., WSPC, (2020). https://doi.org/10.1142/6057
30. Balé, A., Rouffaud, R., Levassort, F., Brenner, R., Hladky-Hennion, A. C., "Homogenization of periodic 1-3 piezocomposite using wave propagation: Toward an experimental method", ***The Journal of the Acoustical Society of America***, Vol. 149, No. 5, (2021), 3122–3132. https://doi.org/10.1121/10.0004824
31. Li, L., Li-Kun, W., Lei, Q., Yuan-Yuan, W., Hong-Liang, D., Bai-Sheng, S., "The Theoretical Model for 1-3-2 Piezoelectric Composites", ***Ferroelectrics***, Vol. 350, No. 1, (2007), 29–37. https://doi.org/10.1080/00150190701369727
32. Smith, W. A., Auld, B. A., "Modeling 1-3 composite piezoelectrics: thickness-mode oscillations", In ***IEEE Transactions on Ultrasonics, Ferroelectrics, and Frequency Control***, Vol. 38, No. 1, (1991), 40–47. https://doi.org/10.1109/58.67833
33. Smith, W. A., "Modeling 1-3 composite piezoelectrics: hydrostatic response", In ***IEEE Transactions on Ultrasonics, Ferroelectrics, and Frequency Control***, Vol. 40, No. 1, (1993), 41–49. https://doi.org/10.1109/58.184997
34. Lin, P., Zhang, L., Fei, C., Li, D., Wu, R., Chen, Q., Hou, C., Yang, Y., "Novel multi-layer-composites design for ultrasonic transducer applications", ***Composite Structures***, Vol. 245, (2020), 112364. https://doi.org/10.1016/j.compstruct.2020.112364

AIMS AND SCOPE

Advanced Ceramics Progress (ACERP) as an ISC international journal is devoted to elucidating the fundamental aspects of chemistry and physics occurring at a wide range of oxide and nonoxide ceramics and composite materials and their processing, microstructure, properties, and applications. The journal provides a unique venue for publishing new exciting research, focusing on dynamic growth areas in this field.

INSTRUCTIONS FOR AUTHORS

Submission of manuscript represents that it has neither been published nor submitted for publication elsewhere and is result of research carried out by author(s).
Authors are required to include a list describing all the symbols and abbreviations in the manuscript. Use of the international system of measurement units is mandatory.

- On-line submission of manuscripts results in faster publication process and is recommended. Instructions are given in the ACERP web site: www.acerp.ir
- References should be numbered in brackets and appear in sequence through the text. List of references should be given at the end of the manuscript.
- Figures' captions are to be indicated under the illustrations. They should sufficiently explain the figures.
- Illustrations should appear in their appropriate places in the text.
- Tables and diagrams should be submitted in a form suitable for reproduction.
- Photographs and figures should be of high quality saved as jpg files (resolution > 600 dpi).
- Tables, illustrations, figures and diagrams will be normally printed in single column width (8 cm). Exceptionally large ones may be printed across two columns (17 cm).

PAGE CHARGES AND REPRINTS

ACERP subscribers do not need to make any payment for publication and reprints.

AUTHORS CHECKLIST

- Author(s), bio-data including academic degree, affiliation(s), ORCiD(s), and e-mail addresses.
- Manuscript including title, abstract, key words, illustrations, tables with tables' captions, figures with figures' captions, acknowledgement, and list of references.
- MS Word files of the manuscript in the ACERP template and all figures (resolution > 600 dpi).
- Similarity check of the manuscript, copyright forms, and conflict of interest forms

Advanced **Cer**amics **P**rogress,
P.O. Box 31787-316, Meshkin Dasht, Alborz, I. R. Iran
Materials and Energy Research Center, Imam Khomeini Blvd, Meshkin Dasht, Alborz, I. R. of Iran
P.O. Box 14155-4777, Tehran, I. R. Iran
No. 5, Ahuramazda St., Alvand Ave., Argentine Sq., Tehran, Tehran, I. R. of Iran

www.merc.ac.ir - www.icers.ir

Advanced Ceramics Progress

Volume 8, Number 2, Spring 2022

CONTENTS

Journal Home Page: www.acerp.ir